

Constitutive theory for mechanics of amorphous thermoplastic polymers under extreme dynamic loading

J.D. Clayton^{1*}

¹Terminal Effects Division, Army Research Directorate
DEVCOM ARL, Aberdeen, MD 21005-5066, USA

Abstract

A geometrically nonlinear continuum mechanical theory is formulated for deformation and failure behaviors of amorphous polymers. The model seeks to capture material response over a range of loading rates, temperatures, and stress states encompassing shock compression, inelasticity, melting, decomposition, and spallation. Thermoelasticity, viscoelasticity, viscoplasticity, ductile failure with localized shear yielding, and brittle fracture with crazing can all emerge under this ensemble of intense loading conditions. Known prior theories have considered one or more, but not all, such physical mechanisms. The present coherent formulation invokes thermodynamics with internal state variables for dynamic molecular and network configurational changes affecting viscoelasticity and plastic deformation, and it uses order parameters for more abrupt structural changes across state-dependent glass-transition and shock-decomposition thresholds. A phase-field order parameter captures material degradation from ductile or brittle fracture, including evolving porosity from crazing. The theory is applied toward polymethyl methacrylate (PMMA) under intense dynamic loading. The high-pressure equilibrium response, with shear strength and temperature over known ranges, is well represented along the principal Hugoniot to pressures far exceeding shock decomposition. Predicted release wave velocities agree with experiment. A semi-analytical solution for steady waves describes the relatively lower-pressure viscoelastic setting, providing insight into relaxation times. One-dimensional calculations assess suitability of the model for representing spall fracture strengths seen in experiments over a range of initial temperatures and loading rates.

Key words: continuum physics; shock waves; viscoelasticity; plasticity; fracture; phase field; amorphous polymers; thermoplastics; polymethyl methacrylate

Contents

1	Introduction	2
----------	---------------------	----------

*Email: john.d.clayton1.civ@army.mil

2 Continuum principles	7
2.1 Standard relations	7
2.2 Kinematics, state variables, and thermodynamics	8
2.3 Phase-field fracture mechanics	11
3 Constitutive theory: amorphous polymers	12
3.1 Internal state variables, inelastic deformation, and free energy	12
3.2 Thermoelasticity	14
3.3 Viscoelasticity	17
3.4 Plasticity	20
3.5 Fracture	23
3.6 Melting	25
3.7 Shock decomposition	27
3.8 Heat conduction and viscosity	30
3.9 Total stress and temperature rate	31
4 Application: PMMA	35
4.1 Hugoniot response to high pressure	35
4.2 Low-pressure shock propagation	42
4.3 Spall fracture	48
5 Conclusions	52
A Appendix: PMMA properties and parameters	53

1 Introduction

Thermoplastic polymers are widely used in commercial and structural applications. Examples include polymethyl methacrylate (PMMA), polyethylene, polystyrene, polyvinylchloride, and polycarbonate (PC). Under the glass transition temperature θ_G , behaviors can be brittle or ductile depending on loading mode, whereas rubbery or viscous fluid-like response manifests above θ_G . Many physical properties vary in the vicinity of θ_G , where the latter itself, for a polymer of specific composition and processing history, is unique only in an ambient equilibrium state. For example, the glass transition in PMMA can be interpreted to vary with pressure and loading rate [1–4]. The term “melting” is used interchangeably to denote transition from glassy to (viscoelastic) rubbery state or from solid to (viscous) liquid state, where the former necessarily occurs at lower temperature than the latter if both are possible; certain polymers can also thermally decompose into various chemical products from a solid state, rather than liquify, with increasing temperature [5].

The present research focuses on amorphous (i.e., non-crystalline) thermoplastics that are glassy at room temperature, and in particular the transparent polymer PMMA, though descriptive models and physical findings may translate to other polymers that share similar physical traits. These materials are used in protection systems including windows (i.e., “bullet-proof glass”), goggles, face shields, and layered transparent armors [6]. PMMA—also known as acrylic or acrylic glass

with trade names Plexiglas and Lucite, among others—is furthermore widely used as a window material in shock physics experiments [7]. Over such a broad dynamic application space, strains, strain rates, pressures, and temperatures can be severe, inducing one or more coupled phenomena: nonlinear elastic and viscoelastic behaviors, plasticity and localization by shear yielding, brittle fracture by crazing and spall, melting, and shock or thermal decomposition. Crazes are cavitation zones arising normal to the direction of maximum principal stress in amorphous polymers [8].

A detailed treatment of origins of physical behaviors at the molecular level is beyond the current scope, but a few remarks are given here for motivation of previous and current continuum theory. The glassy polymer macromolecular structure is comprised of a network of entangled molecular chains. The latter can be idealized as rigid links along the strongly bonded polymer chain [9]. Temporal changes in network entanglement structures and secondary bonding (e.g., chain interactions) induced by strain and temperature histories affect thermo-mechanical properties controlling viscoelasticity, yielding, directional hardening, and fracture mechanisms (e.g., ductility). Viscoelastic and viscoplastic mechanisms are correlated with structural transitions (e.g., α and various β processes [10–12]). Entanglement density affects the tendency for ductile versus brittle failure, the former by shear yielding and the latter by crazing or network disentanglement with chain scission [13, 14]. Generally, the more entanglements, the greater potential for elongation (e.g., plastic flow) without fracture under tensile loading. The quantity “free volume”, namely the unoccupied space in a solid polymer between molecular chains and their aggregates, has also been widely associated to changes in thermal, elastic, viscous, and plastic behaviors [15–19]. Though different physical and mathematical definitions for free volume exist [18], an increase in free volume correlates with strain-softening of plastic yield strength below the glass transition [17] and decreased (e.g., elastic) stiffness across the glass transition itself [18].

A geometrically nonlinear theory is essential in the current applications: elastic and viscoelastic deformations can be large, even in uniaxial shock compression [20]. Apparent shear and bulk moduli vary strongly with temperature and pressure in PMMA, even far below the glass transition [21]. Bulk and shear moduli are time or frequency dependent [22, 23], suggesting a viscoelastic treatment should be included in a complete theory that seeks to span a wide range of loading rates and temperatures [2, 4, 11, 24]. Innumerable theories have been constructed to capture viscoelasticity of thermoplastic polymers. Some models simply assign the elastic coefficients as functions of strain rate in addition to temperature [2, 11]. Others do not resolve viscoelasticity distinctly, but rather implicitly embed all dissipative deformation mechanisms in an inelastic or plastic model component [9, 20, 25–27]. The stress-history functional approach based on fading memory concepts and finite linear viscoelasticity [28] has described one-dimensional (1-D) shock waves [29–31]. A sophisticated model spanning static to shock regimes incorporated non-equilibrium history functionals for bulk and shear response [4]. A viscoelastic-plastic model for thermoplastics [32] used tensor-valued internal variables [33, 34] for configurational energy changes.

In the current work, viscoelastic response is distinguished from (visco)plastic response following Ref. [35], wherein plastic deformation is one form of “anelastic” deformation in that reference. Total elastic deformation can be decomposed into that which is recovered instantaneously (i.e., perfectly glassy response without dissipation) and that which is recovered more slowly (i.e., dissipative viscoelastic response). Finite-strain theories decomposed the deformation gradient into

a product of (instantaneous) elastic and transient viscoelastic parts [35–37]. In this context, the intermediate configuration achieved upon local instantaneous unloading is generally not stress-free. In contrast, in finite elastoplasticity theory (cf. [38]), the intermediate configuration is locally stress-free upon removal of local elastic deformation. In the theory developed in the present work, consistent with Ref. [35], all elastic deformation (instantaneous and viscoelastic) is eventually recovered when load is removed, while plastic deformation is residual and can be permanent in the absence of load reversal. However, the current theory uses tensor-valued internal variables to address viscoelasticity following Refs. [33, 34], and it does not deconstruct the total elastic deformation into instantaneous and dissipative parts. The deformation gradient is decomposed into a total thermoelastic component (encompassing thermal expansion and viscoelasticity) and a residual plastic component incorporating irreversible chain motions, free volume changes, and dilatational crazing mechanisms. The current approach simplifies the kinematic and thermodynamic analysis over that which would be incurred from explicitly resolving thermal, instantaneous elastic, viscous, plastic, and damage mechanisms via distinct terms in the deformation gradient [9, 27, 39], though all mechanisms are properly encompassed in rate form through the velocity gradient.

Finite-deformation constitutive models for amorphous glassy polymers have been under development since at least the 1980s [40], building on seminal earlier studies from materials science, for example, Ref. [41]. Inelastic models with a basis in polymer physics include those of the Boyce and Arruda research groups [9, 11, 42, 43]. Other sophisticated thermodynamics or molecular physics-motivated models include those of the Anand research group [16, 25, 44], Richeton et al. [2, 12, 45, 46] and Bouvard et al. [26, 27]. These models generally use scalar and tensor-valued internal or kinematic variables for capturing hardening and softening associated with polymer chain interactions, rotations, and internal stretches. Large-strain elastic and inelastic behavior has been related to chain orientation distributions [47]; statistical mechanics frequently motivates the former (e.g., [48, 49] and references therein). While many focused only on the glassy response [9, 16, 25, 42, 44, 48], theories have addressed drastic softening witnessed as temperature approaches and exceeds the glass transition [2, 3, 11, 12, 43, 45, 46, 50]. Aforementioned models did not, however, address the high pressures and extreme rates achieved in shock loading. Equations-of-state coupled to less sophisticated inelasticity or rheological models (e.g., no anisotropic hardening) have been developed for this regime and were used predominantly to study the 1-D shock response [4, 20, 51–54]. Empirical plasticity models such as Drucker-Prager [55] and Johnson-Cook [56, 57] have been calibrated to depict shock or ballistic impact of PMMA, but these engineering approaches do not provide insight into relative importance of fundamental physical mechanisms originating at the macromolecular scale, nor do they formally consider continuum thermodynamic relations and restrictions [58, 59].

Brittle fracture of glassy polymers such as PMMA originates from crazing, even at high rates pertinent to dynamics and spallation [10, 60, 61]. Crazing is discussed from a materials physics perspective in Refs. [8, 19, 62] and can incur significant inelastic volume increase [63]. However, the tendency for ductile versus brittle failure tends to increase with temperature [10] and confining pressure [64–66]. Shear banding in PMMA is highly rate sensitive [67]: diffuse bands form at lower rates and sharp bands at higher rates leading to mode II fracture. Temperature rise during ductile or brittle mode II fracture can be large enough to approach or surpass the glass transition,

leading to localized melting [65, 68].

Continuum damage models for crazing have been coupled to finite polymer inelasticity, albeit at moderate rates and low pressures [13, 39]. These methods, devoid of an intrinsic length scale, can produce mesh-sensitive results, as can phenomenological approaches such as the Johnson-Cook fracture model used for ballistic failure response of PMMA [56]. Cohesive finite element (FE) models [69–71] have been used for ductile and brittle fractures. Spallation has been modeled in other material systems (e.g., metallic and ceramic polycrystals) with cohesive models [72–74], but apparently not in monolithic thermoplastics. Regularized phase-field models have been implemented for shear yielding and craze fractures in polymers such as PC and PMMA [14, 19, 75, 76]. These implementations, however, have been limited to relatively low rates, low pressures, and isothermal conditions. Therefore, they are unsuitable for ballistic loading. Spall fracture experiments on amorphous thermoplastics suggest an increase in spall strength with increasing loading (i.e., pressure release) rate [77, 78] and decrease with increasing temperature, the latter notably severe across the glass transition [79, 80]. A micromechanics-based model for spall fracture of PC was developed in Ref. [81]. In a computational study of spall fracture in high density polyethylene [82], a volumetric damage component was appended to the dynamic polymer framework of Clements [4], though details of that damage model and parameters were not reported. Molecular dynamics simulations [83] provide some insight into mechanisms of spallation in polymers, but length and time scales are exceedingly small for comparison to standard experiments. Herein, a phase-field approach extending that of Refs. [75, 84] is extended to study rate- and temperature-dependent crazing pertinent to spall fracture of thermoplastics.

Under planar shock compression, many thermoplastic as well as thermosetting polymers display a variation along their principal Hugoniot in the form of a local volume collapse at pressures around or exceeding the order of 20 GPa [85, 86]. Such behavior was originally attributed to a generic kind of phase transition [85, 87, 88] but has been more recently confirmed as a chemical decomposition from a condensed (solid, melt, or fluid) reactant phase to a combination of condensed elemental and gaseous products [86, 89–92]. Transformation of PMMA to a more fluid phase at impact stresses between 20 and 30 GPa was apparently first discovered by shock-induced polarization measurements of Hauver [87, 88]. This now-designated shock decomposition is accompanied by a volume decrease of 3.4% [85, 86]. A correlation between tendencies for shock-induced polarization and shock-induced conduction in specific polymers was noted in the context of a bond scission model [93, 94]. Modeling of shock decomposition in polymers has been limited to date. Recent methods include distinct tabular equations-of-state for reactant and product phases, thermochemical modeling of products with free energy minimization, and Arrhenius kinetics for reaction rates [89, 91, 92, 95]. For PMMA, the former have been compared with ab initio molecular dynamics simulations [91]. Although temperatures at the decomposition threshold can exceed 1000–2000 K, it is unclear if the material is solid or fluid prior to decomposition due to the immense pressures that should suppress glass-to-melt transition. Shock decomposition at extreme pressures, temperatures, and strain rates should be distinguished from more understood thermal decomposition and combustion processes in polymers at lower pressures [5, 96–98]. Experimental principal Hugoniot data for PMMA exceeding shock pressures of 100 GPa are available [99].

The objective of the present study is construction and demonstration of accuracy and utility of

a constitutive model for amorphous polymers with all features listed below:

- Nonlinear thermo-viscoelasticity applicable to high rates, temperatures, and pressures
- Finite-strain plasticity with isotropic and anisotropic hardening/softening
- Ductile and brittle fracture applicable to high rates, temperatures, and pressures
- Behavior changes across the glass transition and shock decomposition thresholds

No theory known to the author synthesizes all of these features in a manner consistent with established continuum mechanical and thermodynamic laws. The proposed framework achieves its objective using a combined internal variable and phase-field formulation of finite-strain thermo-viscoelasticity and viscoplasticity. The current fully three-dimensional (3-D) theory adapts the established Holzapfel-Simo approach [33, 34] with tensor configurational variables, as this appears more straightforward to integrate with formal internal state variable theory [59] than finite linear viscoelastic functionals [28], non-equilibrium energy functionals [4], and Prony series approximations [100]. Invariants of a logarithmic thermoelastic strain measure [101, 102] enter the free and internal energy functions, contributing to an equation of state valid at high pressure. For viscoplasticity, a combination of scalar and tensor internal state variables (the latter linked to plastic stretch) is adopted to account for isotropic and anisotropic hardening and softening mechanisms [2, 9, 25, 27]. A phase-field model resolving ductile and brittle fracture contributions, with dilatation linked to void growth, adapts ideas from Refs. [14, 19, 75]. Features are newly augmented account for extreme pressures, rates, and temperatures pertinent to shock compression and spall.

Scalar order parameters, of local rather than gradient type, are used to interpolate the material response across the glass transition and shock-decomposition thresholds. Depending on the kinetic laws and functions, the response can be smooth, abrupt or even discontinuous. Phase-field models have been used for interfacial physics of melting and solidification [103] and polymer crystallization [104]. Here, as morphological details of the solid-melt and condensed-vaporized material interfaces are not of primary interest, gradient regularizations of solid-melt and condensed-decomposed order parameters are omitted, as elsewhere in modeling fracture of liquids [105] and soft solids [106] and shear localized melting in metals [107]. The glass-melt transition in amorphous polymers can be interpreted as a second-order phase transformation [108, 109], whereas shock decomposition involves a mass density jump [85, 88] so is of first order.

Given the immense scope of physics, it is unreasonable to expect detailed functions and parameters be obtained for all possible sub-features and loading regimes in a single publication, even for one material. Unique features are demonstrated for 1-D problems in high-rate and shock regimes. These problems, here considering PMMA, can be treated analytically or with basic numerical integration. Notable physics observed in shock experiments include a rapid slope change or inflection in the Hugoniot indicative of a Hugoniot Elastic Limit (HEL) for plastic yielding at a longitudinal stress around 0.7 GPa [7, 110], lack of an elastic precursor [7, 51], rounding of the particle velocity profile due to viscoelastic relaxation [7, 29, 30], and increase or maintenance of shear strength to at least moderate shock pressures on the order of 6–8 GPa [110–113], followed by a decay above 10 GPa [114]. Shear strength is thought to persist at shock-elevated temperatures above the ambient static glass transition (e.g., $\theta_G \approx 375 - 395$ K for common kinds of PMMA) [20]. The aforementioned physics result from a combination of dependence of viscoelastic moduli, plastic flow strength, and melting on pressure and time scale (e.g., loading rate) [4, 20, 115]. Steady wave forms

are observed within a certain impact velocity range and after a minimum run distance [116], at least below the Hugoniot inflection that otherwise can cause dispersion [29]. Shock evolution and steady waves at stresses below the HEL were described in theoretical works by Schuler, Nunziato, and Walsh [29–31, 116, 117]. Their solutions for shock evolution adopted the analysis of Chen and Gurtin [118, 119] on shock waves in (thermo)viscoelastic materials with fading memory and finite linear viscoelasticity. Numerical studies of shock evolution encompassing higher shock pressures in PMMA followed thereafter using various theoretical and computational schemes [4, 20, 51–54]. In the current study, methods of Ref. [106] for viscoelastic soft solids described by internal variables [33, 34], Ref. [120] for fluids with internal variables, and Refs. [121, 122] for steady waves in the context of phase-field fracture are adapted to derive equations for shock evolution in a different constitutive setting for amorphous viscoelastic polymers.

General continuum principles are presented in Section 2. These include balance laws and governing equations deemed pertinent to any thermoviscoelastic-inelastic material with internal state variables of scalar, tensor, and gradient (e.g., phase-field) type demonstrating isotropic elastic response. The constitutive framework is directed toward amorphous polymers, with possible plastic anisotropy, in Section 3. Energy functions and kinetic laws for thermoelasticity, viscoelasticity, plasticity, fracture, melting across the glass transition, and structural decomposition are constructed. Applications to PMMA follow in Section 4. Known physical properties and parameters are reviewed. The principal “equilibrium” shock Hugoniot, including pressure, temperature, shear strength, and structural changes, is calculated via an iterative analytical method in Section 4.1 to shock stresses exceeding the experimental decomposition threshold. Shock evolution and steady waves are analyzed in Section 4.2 for the lower-pressure viscoelastic regime. Spall fracture is analyzed via 1-D dynamic calculations in Section 4.3 for different starting temperatures and loading rates. Comparisons with experiments are included throughout Section 4 where possible, providing complementary insight into observed physics. Conclusions appear in Section 5.

2 Continuum principles

2.1 Standard relations

Denote the spatial volume occupied by a body by $\Omega(t)$, where t is time. In a reference configuration at $t = t_0$, the body occupies $\Omega_0 = \Omega(t_0)$. External boundaries are $\partial\Omega(t)$ and $\partial\Omega_0$ with respective unit normal vector fields $\mathbf{n}(\mathbf{x})$ and $\mathbf{n}_0(\mathbf{X})$. Spatial position is \mathbf{x} measured by coordinate chart(s) $\{x^k\}$ where generally $k = 1, 2, 3$. Similarly, reference position is \mathbf{X} with charts $\{X^K\}$ and $K = 1, 2, 3$. Let \square be a differentiable function of position and time. Basis vectors are $\mathbf{g}_k = \partial_k \mathbf{x}$ and $\mathbf{G}_K = \partial_K \mathbf{X}$ where $\partial_k \square = \partial \square / \partial x^k$ and $\partial_K \square = \partial \square / \partial X^K$. Usual metric tensors have components $g_{ij} = \mathbf{g}_i \cdot \mathbf{g}_j$ and $G_{IJ} = \mathbf{G}_I \cdot \mathbf{G}_J$ with determinants $g = \det(g_{ij})$ and $G = \det(G_{IJ})$. Particle motion and particle velocity are, respectively,

$$\mathbf{x} = \boldsymbol{\chi}(\mathbf{X}, t), \quad \mathbf{v}(\mathbf{X}, t) = \partial \boldsymbol{\chi}(\mathbf{X}, t) / \partial t. \quad (2.1)$$

The material time derivative (i.e., derivative at fixed \mathbf{X}) is denoted by $\dot{\square}$. The partial space-time derivative (i.e., at fixed \mathbf{x}) is denoted by $\partial_t \square$. Material and spatial covariant derivatives are denoted,

respectively, by $\nabla_0 \square$ and $\nabla \square$. The deformation gradient and Jacobian determinant are

$$\mathbf{F} = \nabla_0 \boldsymbol{\chi} = \partial x^i / \partial X^J \mathbf{g}_i \otimes \mathbf{G}^J, \quad J = \sqrt{g/G} \det(F_J^i) = d\Omega / d\Omega_0 > 0. \quad (2.2)$$

The spatial velocity gradient, deformation rate, spin, and rate of volume change obey

$$\mathbf{l} = \nabla \mathbf{v} = \dot{\mathbf{F}} \mathbf{F}^{-1} = \mathbf{d} + \boldsymbol{\omega}, \quad \mathbf{d} = \frac{1}{2}(\mathbf{l} + \mathbf{l}^\top), \quad \boldsymbol{\omega} = \frac{1}{2}(\mathbf{l} - \mathbf{l}^\top), \quad j = J \nabla \cdot \mathbf{v} = J \text{tr} \mathbf{d}. \quad (2.3)$$

Mass densities are $\rho(\mathbf{X}, t)$ and $\rho_0 = \rho(\mathbf{X}, t_0)$. Cauchy stress is $\boldsymbol{\sigma}$, body force per unit mass is \mathbf{b} , internal energy per unit mass is u , spatial heat flux is \mathbf{q} , and point heat sources per unit mass are r . Classical local conservation laws for mass, momentum, and energy are (cf. [38, 123, 124])

$$\dot{\rho} + \rho \text{tr} \mathbf{d} = 0, \quad \nabla \cdot \boldsymbol{\sigma} + \rho \mathbf{b} = \rho \dot{\mathbf{v}}, \quad \boldsymbol{\sigma} = \boldsymbol{\sigma}^\top, \quad \rho \dot{u} = \boldsymbol{\sigma} : \mathbf{d} - \nabla \cdot \mathbf{q} + \rho r. \quad (2.4)$$

The first of (2.4) corresponds to $\rho_0 = \rho J$. The last of (2.4) is derived from the usual, standard global balance of continuum mechanics. No independent contributions from rates of order parameters or their gradients are ascribed to the internal energy rate, and no micro-force balances are imposed, differing from many other phase-field models [14, 121, 125, 126]. Rather, following Refs. [19, 75, 84, 127], the order parameter for fracture obeys conservation and kinetic laws that are independent from the first and second laws of thermodynamics, as will be shown in Section 2.3. The local form of the latter is, with θ absolute temperature and s entropy per unit mass,

$$\rho \theta \dot{s} + \nabla \cdot \mathbf{q} - \rho r - (\mathbf{q}/\theta) \cdot \nabla \theta \geq 0. \quad (2.5)$$

Let ψ be Helmholtz free energy per unit mass and (U, Ψ, η) be (internal energy, free energy, entropy) per unit reference volume. If heat conduction always produces non-negative dissipation, (2.5) with the last of (2.4) provides the non-negative internal dissipation per unit volume \mathfrak{D} :

$$\psi = u - \theta s \Leftrightarrow \Psi = U - \theta \eta; \quad U = \rho_0 u, \quad \Psi = \rho_0 \psi, \quad \eta = \rho_0 s; \quad (2.6)$$

$$\mathfrak{D} = \theta \dot{\eta} + J \nabla \cdot \mathbf{q} - \rho_0 r = J \boldsymbol{\sigma} : \mathbf{d} - \dot{\Psi} - \dot{\theta} \eta \geq 0. \quad (2.7)$$

2.2 Kinematics, state variables, and thermodynamics

The deformation gradient is decomposed into a thermoelastic part \mathbf{F}^E and a plastic part \mathbf{F}^P . Note \mathbf{F}^E encompasses instantaneous hyperelasticity, thermal expansion, and dissipative viscoelastic deformation. Note \mathbf{F}^P encompasses deviatoric plastic flow (e.g., from irreversible molecular chain motions), changes in residual free volume, residual deformation from crack opening (e.g., porosity from crazing), and potential volume changes from melting and decomposition. Specifically,

$$\mathbf{F} = \mathbf{F}^E \mathbf{F}^P, \quad F_J^i = (F^E)_\alpha^i (F^P)_J^\alpha; \quad (2.8)$$

$$\mathbf{l} = \dot{\mathbf{F}}^E (\mathbf{F}^E)^{-1} + \mathbf{F}^E \mathbf{D}^P \mathbf{F}^{E-1}, \quad \mathbf{D}^P = (\mathbf{D}^P)^\top = \dot{\mathbf{F}}^P (\mathbf{F}^P)^{-1} = (\mathbf{F}^E)^{-1} \mathbf{d}^P \mathbf{F}^E. \quad (2.9)$$

The spatial plastic deformation rate is \mathbf{d}^P . For isotropy, plastic velocity gradient \mathbf{D}^P is symmetric; plastic spin vanishes [16, 25, 84, 128]. Implicit in (2.8) is a locally stress-free intermediate configuration. Following [121, 129], basis vectors on this anholonomic space are chosen as $\mathbf{g}_\alpha = \delta_\alpha^K \mathbf{G}_K$ producing metric tensor components $g_{\alpha\beta} = \delta_\alpha^I G_{IJ} \delta_\beta^J$ such that $\det(g_{\alpha\beta}) = G$. Volume ratios obey

$$J^E = \det(F^E)_\alpha^i \sqrt{g/G} > 0, \quad J^P = \det(F^P)_J^\alpha > 0; \quad j^P = J^P \text{tr} \mathbf{D}^P = J^P \text{tr} \mathbf{d}^P. \quad (2.10)$$

Thermoelastic deformation can be decomposed into rotation tensor $\mathbf{R}^E = (\mathbf{R}^E)^{-\top}$ and stretch tensors $\mathbf{U}^E, \mathbf{V}^E$ via polar decompositions. Logarithmic strain tensors and their deviatoric parts follow:

$$\mathbf{F}^E = \mathbf{R}^E \mathbf{U}^E, \quad \mathbf{C}^E = (\mathbf{F}^E)^\top \mathbf{F}^E = (\mathbf{U}^E)^2, \quad \boldsymbol{\epsilon}^E = \ln \mathbf{U}^E = \frac{1}{2} \ln \mathbf{C}^E, \quad \boldsymbol{\varepsilon}_V^E = \ln J^E; \quad (2.11)$$

$$\mathbf{F}^E = \mathbf{V}^E \mathbf{R}^E, \quad \mathbf{B}^E = \mathbf{F}^E (\mathbf{F}^E)^\top = (\mathbf{V}^E)^2, \quad \boldsymbol{e}^E = \ln \mathbf{V}^E = \frac{1}{2} \ln \mathbf{B}^E, \quad e_V^E = \ln J^E; \quad (2.12)$$

$$J^E = \exp[(\boldsymbol{\varepsilon}^E)_\alpha^\alpha] = \exp[(e^E)_k^k], \quad \bar{\boldsymbol{\epsilon}}^E = \boldsymbol{\epsilon}^E - \frac{1}{3} \boldsymbol{\varepsilon}_V^E \mathbf{1}, \quad \bar{\boldsymbol{e}}^E = \boldsymbol{e}^E - \frac{1}{3} e_V^E \mathbf{1}. \quad (2.13)$$

Logarithmic thermoelastic strain in locally relaxed material coordinates [101] is $\boldsymbol{\epsilon}^E$, with deviatoric (i.e., traceless) part $\bar{\boldsymbol{\epsilon}}^E$. Its analogy in spatial coordinates [130–132] is \boldsymbol{e}^E with deviatoric part $\bar{\boldsymbol{e}}^E$.

Denote by $\{\boldsymbol{\alpha}\}(\mathbf{X}, t)$ the set of conventional internal state variable fields, and denote by $\xi(\mathbf{X}, t)$ an order parameter field of gradient type for phase-field fracture that does not belong to $\{\boldsymbol{\alpha}\}(\mathbf{X}, t)$. Properties of ξ are discussed in Section 2.3. Individual entries of $\{\boldsymbol{\alpha}\}$ encompassing configurational viscoelasticity, isotropic and anisotropic plastic hardening, porosity, free volume, and phase fractions of melt and decomposed material are introduced in Section 3.1. For isotropic elasticity, strain energy can depend on up to three independent scalar invariants of \boldsymbol{e}^E [132]. A logarithmic theory for anisotropic elasticity would require dependence on $\boldsymbol{\epsilon}^E$ instead. While more broadly applicable to crystalline [101, 102, 121] solids, use of $\boldsymbol{\epsilon}^E$ is more mathematically cumbersome than \boldsymbol{e}^E . Energy potentials are assigned the following dependencies, omitting argument \mathbf{X} for brevity:

$$\Psi = \Psi(\boldsymbol{e}^E(\mathbf{F}^E), \theta, \{\boldsymbol{\alpha}\}, \xi), \quad U = U(\boldsymbol{e}^E(\mathbf{F}^E), \eta, \{\boldsymbol{\alpha}\}, \xi). \quad (2.14)$$

Total Cauchy stress is split into an elastic part $\boldsymbol{\sigma}^E$ and a viscous part $\boldsymbol{\sigma}^V$ [58, 106], both symmetric:

$$\boldsymbol{\sigma}(\boldsymbol{e}^E, \theta, \{\boldsymbol{\alpha}\}, \xi, \mathbf{d}) = \boldsymbol{\sigma}^E(\boldsymbol{e}^E, \theta, \{\boldsymbol{\alpha}\}, \xi) + \boldsymbol{\sigma}^V(\boldsymbol{e}^E, \theta, \{\boldsymbol{\alpha}\}, \xi, \mathbf{d}). \quad (2.15)$$

Deviatoric parts are denoted by $\bar{\square}$, and spherical Cauchy pressures are p , p^E , and p^V :

$$\bar{\boldsymbol{\sigma}} = \boldsymbol{\sigma} + p \mathbf{1}, \quad \bar{\boldsymbol{\sigma}}^E = \boldsymbol{\sigma}^E + p^E \mathbf{1}, \quad \bar{\boldsymbol{\sigma}}^V = \boldsymbol{\sigma}^V + p^V \mathbf{1}; \quad (2.16)$$

$$p = -\frac{1}{3} \text{tr} \boldsymbol{\sigma}, \quad p^E = -\frac{1}{3} \text{tr} \boldsymbol{\sigma}^E, \quad p^V = -\frac{1}{3} \text{tr} \boldsymbol{\sigma}^V. \quad (2.17)$$

Expanding the first of (2.14) with abbreviated notation $\partial_{\square} \Psi = \partial \Psi / \partial \square$ gives

$$\dot{\Psi} = (\partial_{\mathbf{F}^E} \Psi) : \dot{\mathbf{F}}^E + (\partial_\theta \Psi) \dot{\theta} + (\partial_{\{\boldsymbol{\alpha}\}} \Psi) \{\dot{\boldsymbol{\alpha}}\} + (\partial_\xi \Psi) \dot{\xi}. \quad (2.18)$$

From (2.9) and (2.15), the stress power per unit reference volume is

$$J \boldsymbol{\sigma} : \mathbf{d} = J[\boldsymbol{\sigma}^E(\mathbf{F}^E)^{-\top}] : \dot{\mathbf{F}}^E + J[(\mathbf{F}^E)^\top \boldsymbol{\sigma}^E(\mathbf{F}^E)^{-\top}] : \mathbf{D}^P + \boldsymbol{\tau}^V : \mathbf{d}, \quad \boldsymbol{\tau}^V = J \boldsymbol{\sigma}^V. \quad (2.19)$$

Inserting (2.18) and (2.19) into (2.7) produces

$$\begin{aligned} \mathfrak{D} &= [J \boldsymbol{\sigma}^E(\mathbf{F}^E)^{-\top} - \partial_{\mathbf{F}^E} \Psi] : \dot{\mathbf{F}}^E - [\eta + \partial_\theta \Psi] \dot{\theta} + \boldsymbol{\tau}^V : \mathbf{d} + \mathbf{M}^E : \mathbf{D}^P + \{\boldsymbol{\pi}\} \cdot \{\dot{\boldsymbol{\alpha}}\} + \zeta \dot{\xi} \geq 0; \\ \mathbf{M}^E &= \frac{1}{2} [\mathbf{C}^E \mathbf{S}^E + \mathbf{S}^E \mathbf{C}^E], \quad \mathbf{S}^E = J(\mathbf{F}^E)^{-1} \boldsymbol{\sigma}^E(\mathbf{F}^E)^{-\top}; \quad \{\boldsymbol{\pi}\} = -\partial_{\{\boldsymbol{\alpha}\}} \Psi, \quad \zeta = -\partial_\xi \Psi. \end{aligned} \quad (2.20)$$

Denoted by \mathbf{M}^E and \mathbf{S}^E are a symmetrized Mandel stress [38, 133] and an elastic second Piola-Kirchhoff stress, herein energy per unit reference rather than per unit intermediate-configuration volume. Conjugate forces to internal variables and the fracture parameter are $\{\boldsymbol{\pi}\}$ and ζ .

Regarding the inequality in (2.20), quantities in square brackets are independent of rates of thermoelastic deformation and temperature and thus should be zero per classical arguments [38, 58, 59, 121]. Constitutive relations and a reduced dissipation inequality follow as a result:

$$\boldsymbol{\sigma}^E = J^{-1}(\partial_{\mathbf{F}^E} \Psi)(\mathbf{F}^E)^\top = J^{-1}(\partial_{\mathbf{V}^E} \Psi) \mathbf{V}^E, \quad \eta = -\partial_\theta \Psi; \quad (2.21)$$

$$\mathfrak{D} = \boldsymbol{\tau}^V : \mathbf{d} + \mathbf{M}^E : \mathbf{D}^P + \{\boldsymbol{\pi}\} \cdot \{\dot{\boldsymbol{\alpha}}\} + \zeta \dot{\xi} \geq 0. \quad (2.22)$$

In isotropic logarithmic elasticity, the second identity for $\boldsymbol{\sigma}^E$ in (2.21) can be derived from (2.14) with $\mathbf{e}^E = \mathbf{e}^E(\mathbf{V}^E)$ and $\mathbf{V}^E = (\mathbf{V}^E)^\top = \mathbf{F}^E(\mathbf{R}^E)^\top$. See Ref. [131] where $\boldsymbol{\sigma}^E : \dot{\mathbf{e}}^E = \boldsymbol{\sigma}^E : [\dot{\mathbf{V}}^E(\mathbf{V}^E)^{-1}]$ is confirmed as the rate of elastic strain energy. Then the free energy rate at fixed $(\theta, \{\boldsymbol{\alpha}\}, \xi)$ arises from (2.21), leading to a third equality for stress in isotropic logarithmic elasticity [84, 131, 132]:

$$(\partial_{\mathbf{V}^E} \Psi) : \dot{\mathbf{V}}^E = [J \boldsymbol{\sigma}^E(\mathbf{V}^E)^{-1}] : \dot{\mathbf{V}}^E = J \boldsymbol{\sigma}^E : \dot{\mathbf{e}}^E = (\partial_{\mathbf{e}^E} \Psi) : \dot{\mathbf{e}}^E \Rightarrow \boldsymbol{\sigma}^E = J^{-1} \partial_{\mathbf{e}^E} \Psi. \quad (2.23)$$

Letting $\theta = \theta(\mathbf{e}^E(\mathbf{F}^E), \eta, \{\boldsymbol{\alpha}\}, \xi)$, a Legendre transform [38, 124] produces analogs of (2.21) in terms of internal energy:

$$\boldsymbol{\sigma}^E = J^{-1}(\partial_{\mathbf{F}^E} U)(\mathbf{F}^E)^\top = J^{-1}(\partial_{\mathbf{V}^E} U) \mathbf{V}^E, \quad \theta = \partial_\eta U. \quad (2.24)$$

Heat conduction and viscous response are isotropic. Thermal conductivity is $k_\theta \geq 0$. Bulk viscosity is $\kappa_V \geq 0$, and shear viscosity is $\mu_V \geq 0$. Any or all of $k_\theta, \kappa_V, \mu_V$ can depend on isotropic invariants of thermodynamic state variables $(\mathbf{e}^E, \theta, \{\boldsymbol{\alpha}\}, \xi, \mathbf{d})$ including deformation rate to enable non-Newtonian flow. More definitive forms are given in Section 3.8. Spatial heat flux and spatial viscous stress are assigned traditionally as [123]

$$\begin{aligned} \mathbf{q} &= -k_\theta \nabla \theta; & \boldsymbol{\tau}^V &= J \boldsymbol{\sigma}^V = \kappa_V(\text{tr} \mathbf{d}) \mathbf{1} + 2\mu_V \bar{\mathbf{d}}, & \bar{\mathbf{d}} &= \mathbf{d} - \frac{1}{3}(\text{tr} \mathbf{d}) \mathbf{1}, \\ p^V &= -J^{-1} \kappa_V(\text{tr} \mathbf{d}), & \bar{\boldsymbol{\sigma}}^V &= 2J^{-1} \mu_V \bar{\mathbf{d}}. \end{aligned} \quad (2.25)$$

Entropy production from conduction and viscous stress is always non-negative:

$$-J \mathbf{q} \cdot \nabla \theta = J k_\theta |\nabla \theta|^2 \geq 0, \quad \boldsymbol{\tau}^V : \mathbf{d} = \kappa_V(\text{tr} \mathbf{d})^2 + 2\mu_V \bar{\mathbf{d}} : \bar{\mathbf{d}} \geq 0. \quad (2.26)$$

Following classical thermodynamic procedures (cf. [38]), the local energy balance is transformed into a temperature rate equation. Specifically, using the last of (2.4) in conjunction with (2.21), chain-rule expansion of $\dot{\eta}(\mathbf{e}^E, \theta, \{\boldsymbol{\alpha}\}, \xi)$, and $\dot{U} = \Psi + \dot{\eta} \theta + \eta \dot{\theta}$ from (2.6) gives

$$\begin{aligned} c \dot{\theta} &= \mathbf{M}^E : \mathbf{D}^P - c \theta \boldsymbol{\Gamma} : \dot{\mathbf{e}}^E + \{\boldsymbol{\pi} - \theta \partial_\theta \boldsymbol{\pi}\} \cdot \{\dot{\boldsymbol{\alpha}}\} + (\zeta - \theta \partial_\theta \zeta) \dot{\xi} \\ &\quad + [\kappa_V(\text{tr} \mathbf{d})^2 + 2\mu_V \bar{\mathbf{d}} : \bar{\mathbf{d}}] + J \nabla \cdot (k_\theta \nabla \theta) + \rho_0 r; \end{aligned} \quad (2.27)$$

$$c = -\theta \partial_{\theta\theta}^2 \Psi = \partial_\theta U, \quad \boldsymbol{\Gamma} = -[\partial_{\theta\mathbf{e}^E}^2 \Psi]/c = -[\partial_{\eta\mathbf{e}^E}^2 U]/\theta. \quad (2.28)$$

Specific heat, as energy per unit reference volume, at constant strain is c . Grüneisen's tensor is $\boldsymbol{\Gamma}$.

2.3 Phase-field fracture mechanics

The present phase-field representation of ductile and brittle fracture, including mechanisms of localized shear yielding, chain scission, and crazing for polymers, follows many notions of Refs. [19, 75, 84, 134, 135]. Herein, damage order parameter $\xi \in [0, 1]$ takes a value of 0 for the pristine state and 1 for the fully degraded state. Healing is forbidden in the current application, meaning $\dot{\xi} \geq 0$.

The forthcoming general treatment follows Refs. [75, 84] for isotropic damage. Denote by $l \geq 0$ a constant regularization length approximating the half-width of the significantly damage-softened zone [136]. An integral over the domain of isotropic crack surface density $\check{\gamma}(\xi(\mathbf{X}, t), \nabla_0 \xi(\mathbf{X}, t))$ then defines the regularized crack surface area functional $\Upsilon[\xi(t)]$:

$$\Upsilon[\xi] = \int_{\Omega_0} \check{\gamma} d\Omega_0 = \int_{\Omega_0} \left[\frac{1}{2l} \xi^2 + \frac{l}{2} |\nabla_0 \xi|^2 \right] d\Omega_0. \quad (2.29)$$

A kinetic law for Υ is prescribed as follows, along with admissible natural or essential boundary conditions, recalling that $\mathbf{n}_0(\mathbf{X})$ is the unit normal vector to $\partial\Omega_0$:

$$l \frac{d}{dt} \Upsilon = \int_{\Omega_0} [(1 - \xi) \mathcal{H} - \mathcal{R}] \dot{\xi} d\Omega_0, \quad \mathcal{R} = \frac{1}{2} \beta_\xi \dot{\xi}; \quad [\nabla_0 \xi \cdot \mathbf{n}_0 = 0 \text{ or } \xi = \xi_0 \forall \mathbf{X} \in \partial\Omega_0]. \quad (2.30)$$

Dimensionless forcing and rate functions are respectively written as \mathcal{H} and \mathcal{R} . A scalar viscosity for damage kinetics, with dimensions of time, is denoted by $\beta_\xi(\bullet) \geq 0$; this can be a function of thermodynamic state and rate variables [125, 137]. Differentiation of (2.29), integration by parts, and invocation of the divergence theorem with either choice of boundary conditions in (2.30) gives

$$\frac{d}{dt} \Upsilon = \int_{\Omega_0} \left[\frac{\xi}{l} \dot{\xi} + l \nabla_0 \xi \cdot \nabla_0 \dot{\xi} \right] d\Omega_0 = \int_{\Omega_0} \left[\frac{\xi}{l} - l \nabla_0^2 \xi \right] \dot{\xi} d\Omega_0. \quad (2.31)$$

Setting (2.30) equal to (2.31) and localizing, the kinetic law with standard initial conditions is

$$\beta_\xi \dot{\xi} = 2(1 - \xi) \mathcal{H} - 2[\xi - l^2 \nabla_0^2 \xi], \quad \xi(\mathbf{X}, t_0) = \xi_0(\mathbf{X}) = 0. \quad (2.32)$$

Irreversibility is enforced following arguments established in Refs. [75, 127]. Require the history function $\mathcal{H}(\mathbf{X}, t) = \mathcal{H}(\Phi(\{\boldsymbol{\alpha}(\mathbf{X}, t)\}), t)$ to be a continuous non-decreasing function of function $\Phi \geq 0$. Function Φ , in turn, can depend on any or all of the state variables $\{\boldsymbol{\Lambda}\}$ that exclude ξ :

$$\mathcal{H} = \max_{s \in [0, t]} \Phi(\{\boldsymbol{\Lambda}\}(\mathbf{X}, s)) \geq 0, \quad \{\boldsymbol{\Lambda}\}(\mathbf{X}, t) = \{\boldsymbol{\epsilon}^E, \theta, \{\boldsymbol{\alpha}\}\}(\mathbf{X}, t), \quad \frac{d}{dt} \Upsilon \geq 0. \quad (2.33)$$

Henceforth, s is a dummy time variable not to be confused with entropy per unit mass. Following from (2.33), rate dependent ($\beta_\xi > 0$) and independent ($\beta_\xi \rightarrow 0$) versions of (2.32) are [75, 127]

$$\dot{\xi} = (1/\beta_\xi) \langle 2(1 - \xi) \Phi - 2\xi + 2l^2 \nabla_0^2 \xi \rangle, \quad [\beta_\xi > 0]; \quad (2.34)$$

$$\dot{\xi}[(1 - \xi) \Phi - \xi + l^2 \nabla_0^2 \xi] = 0, \quad \dot{\xi} \geq 0, \quad (1 - \xi) \Phi - \xi + l^2 \nabla_0^2 \xi \leq 0, \quad [\beta_\xi = 0]. \quad (2.35)$$

Rate-dependent law (2.34) is used primarily in what follows. Denote right-continuous Heaviside function by $H(\square)$, whereby $H(0) = 1$. Set $\beta_\xi = \beta_0^\xi / H(\zeta)$ where $\beta_0^\xi = \text{const} > 0$ and $\zeta = -\partial_\xi \Psi$. It follows from (2.34) that any dissipation from fracture in (2.22) must be non-negative:

$$\xi(\mathbf{X}, t) \in [0, 1], \quad \dot{\xi} \geq 0; \quad \mathfrak{D}^\xi = \zeta \dot{\xi} = (\zeta H(\zeta) / \beta_0^\xi) \langle 2(1 - \xi) \Phi - 2\xi + 2l^2 \nabla_0^2 \xi \rangle \geq 0. \quad (2.36)$$

The needed function Φ is assigned for amorphous polymer physics in Section 3.5.

3 Constitutive theory: amorphous polymers

3.1 Internal state variables, inelastic deformation, and free energy

The framework of Section 2 is specialized to amorphous thermoplastic polymers in a glassy state at room temperature and atmospheric pressure. Internal state variables consist of the fracture phase-field parameter field $\xi(\mathbf{X}, t)$ of Section 2.3 and the following dimensionless fields:

$$\{\boldsymbol{\alpha}\}(\mathbf{X}, t) \ni \begin{cases} \{\mathbf{Y}\}(\mathbf{X}, t) & : \text{tensor-valued viscoelastic configurational variables,} \\ \{\xi\}(\mathbf{X}, t) & : \text{scalar-valued plastic isotropic hardening/softening variables,} \\ \mathbf{A}(\mathbf{X}, t) & : \text{tensor-valued plastic anisotropic hardening variable,} \\ \varphi(\mathbf{X}, t) & : \text{scalar-valued residual free volume change,} \\ \phi(\mathbf{X}, t) & : \text{scalar-valued void volume fraction,} \\ \omega(\mathbf{X}, t) & : \text{scalar-valued melt fraction of non-dissociated material,} \\ \Xi(\mathbf{X}, t) & : \text{scalar-valued decomposition fraction.} \end{cases} \quad (3.1)$$

Governing equations for $\{\mathbf{Y}\}$ are discussed in Section 3.3, $(\{\xi\}, \mathbf{A}, \varphi)$ in Section 3.4, ϕ in Section 3.5, ω in Section 3.6, and Ξ in Section 3.7. The following constraints are noted:

$$\mathbf{Y} = \mathbf{Y}^T; \quad \mathbf{A} = \mathbf{A}^T, \quad \det \mathbf{A} = 1; \quad 0 \leq \varphi \ll 1; \quad \phi \in [0, 1]; \quad \omega \in [0, 1]; \quad \Xi \in [0, 1]. \quad (3.2)$$

Henceforth, the state variable ω refers to a rubbery melt phase rather than a liquid melt. The latter is not formally distinguished with a state variable, but rather is achieved in practice by a temperature-softening shear modulus. Melting is not applicable for the decomposed phase; $\omega(\mathbf{X}, t) + \Xi(\mathbf{X}, t) > 1$ is possible. When the material is partially melted or partially decomposed (e.g., $\omega(\mathbf{X}, t) \in (0, 1)$ or $\Xi(\mathbf{X}, t) \in (0, 1)$), all phases at (\mathbf{X}, t) share the same deformation gradient \mathbf{F} , the same values of \mathbf{F}^E and \mathbf{F}^P , and the same values of temperature $\theta(\mathbf{X}, t)$. For example, if material undergoes plastic deformation prior to liquification, \mathbf{F}^P loses physical meaning but is not automatically reversed when the solid liquifies. Similarly, ξ and the internal state variables in (3.1) are defined only for the entire volume element $d\Omega$, even in a mixed-phase state, and are not formally distinguished among phases. Stress, entropy, and other response functions for the volume element, if of mixed phases, are obtained from thermodynamic relations in Section 2 where free energy density is a weighted sum of contributions from each phase as assigned in what follows in (3.9).

Total plastic deformation rate \mathbf{D}^P defined in (2.9) and rate of plastic volume change J^P of (2.10) contain contributions from isochoric shear-plastic flow, generally anisotropic dilatational crazing or scission, residual free volume change, and isotropic structural or chemical decomposition:

$$\mathbf{D}^P = \dot{\boldsymbol{\varepsilon}}^P + \frac{\dot{\phi}}{1-\phi} \mathbf{N}^\phi + \frac{\dot{\phi} c_\phi}{3(1-\phi c_\phi)} \mathbf{1} + \frac{\dot{\Xi} \delta_\Xi}{3(1-\Xi \delta_\Xi)} \mathbf{1}, \quad (3.3)$$

$$J^P (J^P)^{-1} = \dot{\phi}/(1-\phi) + \dot{\phi} c_\phi/(1-\phi c_\phi) + \dot{\Xi} \delta_\Xi/(1-\Xi \delta_\Xi), \quad (3.4)$$

$$\dot{\boldsymbol{\varepsilon}}^P = (\dot{\boldsymbol{\varepsilon}}^P)^T, \quad \text{tr} \dot{\boldsymbol{\varepsilon}}^P = 0; \quad \mathbf{N}^\phi = \mathbf{n}_\phi \otimes \mathbf{n}_\phi, \quad \mathbf{n}_\phi \cdot \mathbf{n}_\phi = 1, \quad \bar{\mathbf{N}}^\phi = \mathbf{N}^\phi - \frac{1}{3} \mathbf{1}; \quad (3.5)$$

$$\bar{\mathbf{D}}^P = \dot{\boldsymbol{\varepsilon}}^P + [\dot{\phi}/(1-\phi)] \bar{\mathbf{N}}^\phi; \quad c_\phi = \text{const} \in [0, 1), \quad \delta_\Xi = \text{const} \in (-\infty, 1). \quad (3.6)$$

The non-negative parameter c_ϕ quantifies the amount of free volume change that contributes to net plastic dilatation. If all local free volume in a material element is offset by increased density from of polymer chains, local mass density is unchanged and $c_\phi \rightarrow 0$. Relative volume change from complete shock decomposition is quantified by δ_{Ξ} . The deviatoric part of the total plastic deformation rate is $\bar{\mathbf{D}}^P$. The unit vector in the direction of craze or scission crack opening, normal to a mode I crack plane, is \mathbf{n}_ϕ . From (3.3)–(3.6) and noting $\text{tr} \mathbf{M}^E = -3Jp^E$, total dissipation from inelasticity entering (2.22) is

$$\mathbf{M}^E : \mathbf{D}^P = \bar{\mathbf{M}}^E : \dot{\mathbf{\bar{e}}}^P + \left[\frac{\bar{\mathbf{M}}^E : \bar{\mathbf{N}}^\phi - Jp^E}{1 - \phi} \right] \dot{\phi} - \left[\frac{Jp^E c_\phi}{1 - \phi c_\phi} \right] \dot{\phi} - \left[\frac{Jp^E \delta_{\Xi}}{1 - \Xi \delta_{\Xi}} \right] \dot{\Xi}. \quad (3.7)$$

If ω were to describe a transition from crystalline to amorphous state, or solid to liquid, then nonzero volume change, and possible shape change [103, 107], would be expected [138]. However, specific volume remains continuous across the glass transition in amorphous polymers of interest (e.g., [2–4]), so (3.3) contains no explicit contribution from $\dot{\omega}$. Inelastic shape changes from shock decomposition are physically possible but are omitted here for brevity and lack of quantifiable data on their magnitudes. The change in free volume ϕ that affects J^P is very small [19] and therefore often omitted for brevity [16]. This quantity is somewhat analogous to the volume or mass density change from dislocations or other lattice defects in crystalline solids [38, 84] usually omitted in crystal plasticity theory. Assignment of $\mathbf{n}_\phi(\mathbf{X}, t)$ is discussed in Section 3.5.

A standard uniform reference state at $t = t_0$ is defined as follows. The material is undeformed, undamaged, fully dense (i.e., null porosity), and fully glassy (i.e., no melting or decomposition). Corresponding initial conditions on deformation gradient fields, temperature, ξ , and $\{\alpha\}$ are

$$\begin{aligned} \mathbf{F}(\mathbf{X}, t_0) &= \mathbf{F}^E(\mathbf{X}, t_0) = \mathbf{F}^P(\mathbf{X}, t_0) = \mathbf{1}, & \theta(\mathbf{X}, t_0) &= \theta_0 = \text{const} \in (0, \theta_G); \\ \xi(\mathbf{X}, t_0) &= 0, & \{\mathbf{Y}\}(\mathbf{X}, t_0) &= \{\mathbf{0}\}, & \{\zeta\}(\mathbf{X}, t_0) &= \{0\}, & \mathbf{A}(\mathbf{X}, t_0) &= \mathbf{1}, \\ \varphi(\mathbf{X}, t_0) &= \phi(\mathbf{X}, t_0) = \omega(\mathbf{X}, t_0) = \Xi(\mathbf{X}, t_0) = 0. \end{aligned} \quad (3.8)$$

The glass transition temperature at atmospheric pressure and null mechanical loading is $\theta_G = \text{const}$.

Helmholtz free energy per unit reference volume Ψ comprises functions for glassy phase Ψ^G , melt phase Ψ^M , and decomposed products Ψ^D , recalling from (2.13) that e_V^E and $\bar{\mathbf{e}}^E$ are finite logarithmic elastic volume and shape strains:

$$\begin{aligned} \Psi(\mathbf{e}^E, \theta, \xi, \{\mathbf{Y}\}, \{\zeta\}, \mathbf{A}, \varphi, \phi, \omega, \Xi) &= (1 - \Xi)[(1 - \omega)\Psi^G(\bar{\mathbf{e}}^E, e_V^E, \theta, \xi, \{\mathbf{Y}\}, \{\zeta\}, \mathbf{A}, \varphi, \phi) \\ &\quad + \omega\Psi^M(\bar{\mathbf{e}}^E, e_V^E, \theta, \xi, \{\mathbf{Y}\}, \{\zeta\}, \mathbf{A}, \varphi, \phi)] + \Xi\Psi^D(e_V^E, \theta). \end{aligned} \quad (3.9)$$

From the rightmost term in (3.9), shock-decomposed products are dissociated such that shear strain and internal state variables contribute no free energy. Energies can be transformed to per unit mass dimensions via $\psi = \Psi/\rho_0$, where $\rho_0 = \text{const}$ is mass density of glassy solid in state (3.8). Internal energy can be obtained as a function of strain, internal state, and temperature via $U = \Psi - \theta\partial_\theta\Psi$.

Free energies are deconstructed into volumetric and shear elastic strain energies Ψ_V^E and Ψ_S^E , bulk thermoelastic coupling energy Ψ_β^E , volumetric and shear viscoelastic configurational energies Ψ_V^r and Ψ_S^r , energy of plastic microstructure evolution Ψ^P (e.g., cold work [139, 140]), and

specific and latent heat energy Ψ^θ . Denoting degradation functions from damage by f_V^E and f_S^E ,

$$\begin{aligned}\Psi^G(\mathbf{e}^E, \theta, \xi, \{\mathbf{r}\}, \{\zeta\}, \mathbf{A}, \phi, \phi) = & f_V^E(\xi, e_V^E)[\Psi_V^{G,E}(e_V^E) + \Psi_\beta^{G,E}(e_V^E, \theta) + \Psi_V^{G,Y}(e_V^E, \{\mathbf{r}_V\}, \theta)] \\ & + f_S^E(\xi)[\Psi_S^{G,E}(\bar{\mathbf{e}}^E, e_V^E, \theta) + \Psi_S^{G,Y}(\bar{\mathbf{e}}^E, e_V^E, \{\mathbf{r}_S\}, \theta)] \\ & + f_S^E(\xi)[\Psi^{G,P}(\{\zeta\}, \mathbf{A}, \phi, \phi, \theta)] + \Psi^{G,\theta}(\theta),\end{aligned}\quad (3.10)$$

$$\begin{aligned}\Psi^M(\mathbf{e}^E, \theta, \xi, \{\mathbf{r}\}, \{\zeta\}, \mathbf{A}, \phi, \phi) = & f_V^E(\xi, e_V^E)[\Psi_V^{M,E}(e_V^E) + \Psi_\beta^{M,E}(e_V^E, \theta) + \Psi_V^{M,Y}(e_V^E, \{\mathbf{r}_V\}, \theta)] \\ & + f_S^E(\xi)[\Psi_S^{M,E}(\bar{\mathbf{e}}^E, e_V^E, \theta) + \Psi_S^{M,Y}(\bar{\mathbf{e}}^E, e_V^E, \{\mathbf{r}_S\}, \theta)] \\ & + f_S^E(\xi)[\Psi^{M,P}(\{\zeta\}, \mathbf{A}, \phi, \phi, \theta)] + \Psi^{M,\theta}(\theta),\end{aligned}\quad (3.11)$$

$$\Psi^D(e_V^E, \theta) = \Psi_V^{D,E}(e_V^E) + \Psi_\beta^{D,E}(e_V^E, \theta) + \Psi^{D,\theta}(\theta); \quad (3.12)$$

Degradation functions $f_S^E(\xi)$ and $f_V^E(\xi, e_V^E)$ depend on ξ in the usual quadratic sense [14, 19, 75, 121] and f_E^V on volume change e_V^E ensuring a positive bulk modulus in compression [141]:

$$f_S^E(\xi) = (1 - \xi)^2, \quad f_V^E(\xi, e_V^E) = (1 - \xi \mathsf{H}(e_V^E))^2. \quad (3.13)$$

Recall the right-continuous Heaviside unit step function is $\mathsf{H}(\square)$; $f_V^E(\xi, e_V^E \geq 0) = f_S^E(\xi)$. As in Refs. [14, 19, 84], functions (3.13) do not depend explicitly on ϕ , but porosity can affect kinetics of ξ . Superscripts $\square^{G,*}$, $\square^{M,*}$, $\square^{D,*}$ label free energies of glass, melt, and decomposed states. Notation \mathbf{r}_V and \mathbf{r}_S labels configurational variables for volumetric and shear deformation. Forms for other functions on right sides of (3.10)–(3.12) are posited in Sections 3.2, 3.3, and 3.4.

3.2 Thermoelasticity

Thermoelastic free energy describes an equilibrium response with no viscoelastic, plastic, or rate effects. Dependence on strain is through two independent invariants $e_V^E = \text{tr} \mathbf{e}^E = \ln J^E$ and $|\bar{\mathbf{e}}^E|^2 = \bar{\mathbf{e}}^E : \bar{\mathbf{e}}^E = \text{tr}[(\bar{\mathbf{e}}^E)^2]$. A third invariant is admissible for nonlinear isotropic elasticity [124] but is not implemented. For the decomposed substance, all free energy Ψ^D in (3.12) is thermoelastic. For the solid in glassy (3.10) and rubbery (3.11) states, thermoelastic free energy $\Psi^{*,E}$ comprises terms from purely volumetric deformation, shear deformation, thermoelastic coupling, and specific heat.

Volumetric contributions are each akin to a “cold curve” [142] in the limit that $\theta_0 \rightarrow 0$. These contribute an isotropic elastic pressure $p_V^{*,E}$ that depends only on volume change:

$$\Psi_V^{G,E} = \begin{cases} B_0^{G,E}(e_V^E)^2 \left[\frac{1}{2!} - \frac{1}{3!} B_1^{G,E} e_V^E + \frac{1}{4!} B_2^{G,E}(e_V^E)^2 - \frac{1}{5!} B_3^{G,E}(e_V^E)^3 + \dots \right], & [e_V^E \leq 0], \\ \frac{1}{2} B_0^{G,E}(e_V^E)^2, & [e_V^E > 0]; \end{cases} \quad (3.14)$$

$$p_V^{G,E} = -\frac{1}{J} \frac{\partial \Psi^{G,E}}{\partial e_V^E} = \begin{cases} -\frac{1}{J} B_0^{G,E} e_V^E \left[1 - \frac{1}{2!} B_1^{G,E} e_V^E + \frac{1}{3!} B_2^{G,E}(e_V^E)^2 - \frac{1}{4!} B_3^{G,E}(e_V^E)^3 \dots \right], & [e_V^E \leq 0], \\ -\frac{1}{J} B_0^{G,E} e_V^E, & [e_V^E > 0]; \end{cases} \quad (3.15)$$

$$\Psi_V^{M,E} = \begin{cases} B_0^{M,E}(e_V^E)^2 \left[\frac{1}{2!} - \frac{1}{3!} B_1^{M,E} e_V^E + \frac{1}{4!} B_2^{M,E} (e_V^E)^2 - \frac{1}{5!} B_3^{M,E} (e_V^E)^3 + \dots \right], & [e_V^E \leq 0], \\ \frac{1}{2} B_0^{M,E} (e_V^E)^2, & [e_V^E > 0]; \end{cases} \quad (3.16)$$

$$p_V^{M,E} = -\frac{1}{J} \frac{\partial \Psi^{M,E}}{\partial e_V^E} = \begin{cases} -\frac{1}{J} B_0^{M,E} e_V^E \left[1 - \frac{1}{2!} B_1^{M,E} e_V^E + \frac{1}{3!} B_2^{M,E} (e_V^E)^2 - \frac{1}{4!} B_3^{M,E} (e_V^E)^3 \dots \right], & [e_V^E \leq 0], \\ -\frac{1}{J} B_0^{M,E} e_V^E, & [e_V^E > 0]. \end{cases} \quad (3.17)$$

$$\Psi_V^{D,E} = \begin{cases} B_0^{D,E}(e_V^E)^2 \left[\frac{1}{2!} - \frac{1}{3!} B_1^{D,E} e_V^E + \frac{1}{4!} B_2^{D,E} (e_V^E)^2 - \frac{1}{5!} B_3^{D,E} (e_V^E)^3 + \dots \right], & [e_V^E \leq 0], \\ 0, & [e_V^E > 0]; \end{cases} \quad (3.18)$$

$$p_V^{D,E} = -\frac{1}{J} \frac{\partial \Psi^{D,E}}{\partial e_V^E} = \begin{cases} -\frac{1}{J} B_0^{D,E} e_V^E \left[1 - \frac{1}{2!} B_1^{D,E} e_V^E + \frac{1}{3!} B_2^{D,E} (e_V^E)^2 - \frac{1}{4!} B_3^{D,E} (e_V^E)^3 \dots \right], & [e_V^E \leq 0], \\ 0, & [e_V^E > 0]. \end{cases} \quad (3.19)$$

A linear-type response is invoked for elastic tensile states in glassy and melt phases since volumetric expansion is constrained by limits of fracture or cavitation. Decomposed products comprise gaseous fluid and disassociated particulate matter [86, 91]; products are approximated as having null (tensile) cold pressure for $e_V^E > 0$. The isothermal equilibrium bulk modulus at $e_V^E = 0$ and $\theta = \theta_0$ is $B_0^{*,E}$. Dimensionless constants for nonlinear pressure-volume response are $B_1^{*,E}, B_2^{*,E}, B_3^{*,E}, \dots$. The first is related to the pressure derivative of isothermal equilibrium tangent bulk modulus $B^{*,E} = -J \partial p / \partial J$ at the reference state via $B_1^{*,E} + 2 = (\partial B^{*,E} / \partial p)|_0$ [101, 102]. Energies $\Psi_V^{*,E}$ are non-negative so long as $B_k^{*,E} \geq 0 \forall k = 0, 1, 2, \dots$. Only $B_0^{*,E} > 0$ is essential for generic applications. Note coupling $\Psi_\beta^{*,E}$ and viscoelastic $\Psi_V^{*,r}$ and $\Psi_S^{*,r}$ energies, and not cold energy $\Psi_V^{*,E}$, all specified later, can affect temperature dependence of the tangent bulk modulus.

Shear-dominant contributions in condensed phases arise from an equilibrium shear modulus $G^{*,E}(e_V^E, \theta)$ that depends at most linearly on temperature (omitted in Ref. [20]) and up to quadratically on volume change as in Ref. [20]. A deviatoric Cauchy stress $\bar{\sigma}_S^{*,E}$ is the primary result, but a pressure contribution $p_S^{*,E}$ arises from volume dependence of $G^{*,E}$:

$$\Psi_S^{G,E} = G_0^{G,E} \left[1 + (G_\theta^{G,E} / G_0^{G,E})(\theta - \theta_0) - (B_0^{G,E} \{G_p^{G,E} - G_2^{G,E} e_V^E\} / G_0^{G,E}) e_V^E \right] \bar{\epsilon}^E : \bar{\epsilon}^E, \quad (3.20)$$

$$\bar{\sigma}_S^{G,E} = \frac{1}{J} \frac{\partial \Psi_S^{G,E}}{\partial \bar{\epsilon}^E} = \frac{2}{J} G_0^{G,E} \left[1 + \frac{G_\theta^{G,E}}{G_0^{G,E}} (\theta - \theta_0) - \frac{B_0^{G,E}}{G_0^{G,E}} (G_p^{G,E} - G_2^{G,E} e_V^E) e_V^E \right] \bar{\epsilon}^E, \quad (3.21)$$

$$p_S^{G,E} = -\frac{1}{J} \frac{\partial \Psi_S^{G,E}}{\partial e_V^E} = \frac{1}{J} B_0^{G,E} (G_p^{G,E} - 2G_2^{G,E} e_V^E) \bar{\epsilon}^E : \bar{\epsilon}^E; \quad (3.22)$$

$$\Psi_S^{M,E} = G_0^{M,E} \left[1 + (G_\theta^{M,E} / G_0^{M,E})(\theta - \theta_G) - (B_0^{M,E} \{G_p^{M,E} - G_2^{M,E} e_V^E\} / G_0^{M,E}) e_V^E \right] \bar{\epsilon}^E : \bar{\epsilon}^E, \quad (3.23)$$

$$\bar{\sigma}_S^{M,E} = \frac{1}{J} \frac{\partial \Psi_S^{M,E}}{\partial \bar{\epsilon}^E} = \frac{2}{J} G_0^{M,E} \left[1 + \frac{G_\theta^{M,E}}{G_0^{M,E}} (\theta - \theta_G) - \frac{B_0^{M,E}}{G_0^{M,E}} (G_p^{M,E} - G_2^{M,E} e_V^E) e_V^E \right] \bar{\epsilon}^E, \quad (3.24)$$

$$p_S^{M,E} = -\frac{1}{J} \frac{\partial \Psi_S^{M,E}}{\partial e_V^E} = \frac{1}{J} B_0^{M,E} (G_p^{M,E} - 2G_2^{M,E} e_V^E) \bar{\epsilon}^E : \bar{\epsilon}^E. \quad (3.25)$$

The equilibrium shear modulus in an unstrained state is $G_0^{*,E} > 0$, referred to θ_0 for glass and θ_G for melt. Temperature and pressure derivatives of $G^{*,E}$ are respectively, to first order, $G_\theta^{*,E}$ and $G_p^{*,E}$. Constant $G_2^{*,E}$ gives a second-order volume dependency. In typical solids, $G_\theta^{*,E} < 0$ and $G_p^{*,E} > 0$. This would enable the tangent shear modulus to become negative at large temperatures or tensile states. To circumvent this, the tangent shear modulus and $\Psi_S^{*,E}$ are forbidden to be negative:

$$\frac{G_\theta^{G,E}}{G_0^{G,E}}(\theta - \theta_0) - \frac{B_0^{G,E}}{G_0^{G,E}}(G_p^{G,E} - G_2^{G,E} e_V^E) e_V^E < -1 \Rightarrow \Psi_S^{G,E} = 0 = p_S^{G,E}, \quad \bar{\sigma}_S^{G,E} = \mathbf{0}; \quad (3.26)$$

$$\frac{G_\theta^{M,E}}{G_0^{M,E}}(\theta - \theta_G) - \frac{B_0^{M,E}}{G_0^{M,E}}(G_p^{M,E} - G_2^{M,E} e_V^E) e_V^E < -1 \Rightarrow \Psi_S^{M,E} = 0 = p_S^{M,E}, \quad \bar{\sigma}_S^{M,E} = \mathbf{0}. \quad (3.27)$$

Transition from a solid to liquid state can be linked to a vanishing tangent shear modulus [143]. At null strain, the transition from rubber to liquid melt would occur at a liquification temperature θ_M :

$$\theta_M = \theta_G - G_0^{M,E} / G_\theta^{M,E} > \theta_G, \quad \theta_G \leq \theta_0 - G_0^{G,E} / G_\theta^{G,E}, \quad [G_\theta^{M,E} < 0, G_\theta^{G,E} < 0]. \quad (3.28)$$

Inequalities in (3.28) ensure that, at null elastic volume strain, the glassy phase has non-negative shear modulus at $\theta = \theta_G$ and glass transition temperature θ_G cannot exceed the liquification temperature of the glass. These are valid only when shear moduli decrease with increasing θ .

Equilibrium thermoelastic coupling energy $\Psi_\beta^{*,E}$ accounts for interaction energy from temperature and elastic strain. For isotropic response, this energy depends only on the first strain invariant e_V^E . The corresponding contribution to the Grüneisen tensor Γ in (2.28) is spherical and allowed to depend up to quadratically on volumetric strain [20]. Let $(c_{V0}^G, c_{V0}^M, c_{V0}^D)$ denote specific heat per unit reference volume of (glass, melt, decomposed) phases at $\theta = \theta_0$ and $\epsilon^E = \mathbf{0}$. Then prescribe for each phase the following free energy and resulting pressure contribution $p_\beta^{*,E} = -\frac{1}{J} \partial \Psi_\beta^{*,E} / \partial e_V^E$:

$$\Psi_\beta^{G,E} = -c_{V0}^G(\theta - \theta_0)e_V^E[\Gamma_0^{G,E} + \frac{1}{2!}\Gamma_1^{G,E}e_V^E + \frac{1}{3!}\Gamma_2^{G,E}(e_V^E)^2], \quad (3.29)$$

$$p_\beta^{G,E} = \frac{c_{V0}^G}{J}(\theta - \theta_0)[\Gamma_0^{G,E} + \Gamma_1^{G,E}e_V^E + \frac{1}{2!}\Gamma_2^{G,E}(e_V^E)^2]; \quad (3.30)$$

$$\Psi_\beta^{M,E} = -c_{V0}^M(\theta - \theta_0)e_V^E[\Gamma_0^{M,E} + \frac{1}{2!}\Gamma_1^{M,E}e_V^E + \frac{1}{3!}\Gamma_2^{M,E}(e_V^E)^2], \quad (3.31)$$

$$p_\beta^{M,E} = \frac{c_{V0}^M}{J}(\theta - \theta_0)[\Gamma_0^{M,E} + \Gamma_1^{M,E}e_V^E + \frac{1}{2!}\Gamma_2^{M,E}(e_V^E)^2]; \quad (3.32)$$

$$\Psi_\beta^{D,E} = -c_{V0}^D(\theta - \theta_0)e_V^E[\Gamma_0^{D,E} + \frac{1}{2!}\Gamma_1^{D,E}e_V^E + \frac{1}{3!}\Gamma_2^{D,E}(e_V^E)^2], \quad (3.33)$$

$$p_\beta^{D,E} = \frac{c_{V0}^D}{J}(\theta - \theta_0)[\Gamma_0^{D,E} + \Gamma_1^{D,E}e_V^E + \frac{1}{2!}\Gamma_2^{D,E}(e_V^E)^2]. \quad (3.34)$$

The equilibrium Grüneisen parameter for respective glassy, rubbery, or decomposed phases in the unstrained condition is $\Gamma_0^{G,E}$, $\Gamma_0^{M,E}$, or $\Gamma_0^{D,E}$. Constants $\Gamma_1^{*,E}$ and $\Gamma_2^{*,E}$ enable linear and quadratic

volume dependence of the spherical part of the equilibrium Grüneisen tensor entering (2.28):

$$\begin{aligned}\boldsymbol{\Gamma}^{*,E} &= -\frac{1}{c_V^*} \frac{\partial^2 (f_V^E \boldsymbol{\Psi}_\beta^{*,E} + f_S^E \boldsymbol{\Psi}_S^{*,E})}{\partial \theta \partial \boldsymbol{e}^E} \\ &= \frac{c_{V0}^*}{c_V^*} \left\{ f_V^E [\Gamma_0^{*,E} + \Gamma_1^{*,E} e_V^E + \frac{1}{2} \Gamma_2^{*,E} (e_V^E)^2] \mathbf{1} - 2 f_S^E \frac{G_\theta^{*,E}}{c_{V0}^*} \bar{\boldsymbol{e}}^E \right\}. \end{aligned} \quad (3.35)$$

Lastly, the purely thermal energy $\Psi^{*,\theta}(\theta)$ comprises specific and possible latent heat. Denote by λ_θ^D a latent heat parameter [103, 107, 144] that, when positive, increases the internal energy of decomposing material due to bond rearrangements, scissions, or dissociations [85, 93]. Denote by c_θ^* temperature derivatives of the specific heat at constant strain that herein varies linearly with temperature in each phase. Define $(c_{00}^G, c_{00}^M, c_{00}^D)$ specific heat constants of (glass, melt, decomposed) phases linearly extrapolated downward to $\theta = 0$ from $\theta = \theta_0$. Let $\Psi_0^{*,\theta}$ be datum constants accounting for free energy differences between phases coexisting at the same temperature and strain, vanishing by default for the glassy state. Contributions to specific heat from viscoelastic coupling are theoretically and physically possible [117, 145] but are assumed negligible here [4]. Denote by $\theta_D = \text{const} > \theta_G$ a zero-strain decomposition temperature [5, 96]. No latent heat is associated with the glass-melt transition that is often viewed as a second-order transformation [108, 109]; null volume change is correspondingly assigned for this melting process in (3.3) and Section 3.4. In contrast, decomposition is modeled as a first-order phase transition [85, 88] with potentially, but not necessarily, nonzero latent heat and volume change as discussed in Section 3.7. Then, given these definitions and assumptions,

$$\Psi^{G,\theta} = -c_{00}^G [\theta \ln \frac{\theta}{\theta_0} - (\theta - \theta_0)] - \frac{c_\theta^G}{2} (\theta - \theta_0)^2, \quad c_V^* = -\theta \frac{d^2 \Psi^{*,\theta}}{d\theta^2} = c_{V0}^* + c_\theta^* (\theta - \theta_0), \quad (3.36)$$

$$\Psi^{M,\theta} = -c_{00}^M [\theta \ln \frac{\theta}{\theta_0} - (\theta - \theta_0)] - \frac{c_\theta^M}{2} (\theta - \theta_0)^2 + \Psi_0^{M,\theta}; \quad c_{00}^* = c_{V0}^* - c_\theta^* \theta_0; \quad (3.37)$$

$$\Psi^{D,\theta} = -c_{00}^D [\theta \ln \frac{\theta}{\theta_0} - (\theta - \theta_0)] - \frac{c_\theta^D}{2} (\theta - \theta_0)^2 - \frac{\lambda_\theta^D}{\theta_D} (\theta - \theta_D) + \Psi_0^{D,\theta}. \quad (3.38)$$

3.3 Viscoelasticity

Strain-like configurational state variables for viscoelasticity comprise volumetric and shear contributions $\{\mathbf{r}\} = (\{\mathbf{r}_V\}, \{\mathbf{r}_S\})$. These are further decomposed into $l = 1, \dots, L$ bulk relaxation modes and $m = 1, \dots, M$ shear modes: $\{\mathbf{r}_V\} = (\mathbf{r}_1^V, \dots, \mathbf{r}_L^V)$ and $\{\mathbf{r}_S\} = (\mathbf{r}_1^S, \dots, \mathbf{r}_M^S)$. Recall that for a local volume element of mixed phases, these internal state variables, like kinematic variables and temperature, are not distinguished among glassy, melt, and decomposed phases. Instead, their kinetic equations are influenced by local melt and decomposition fractions ω and Ξ .

The present treatment extends Refs. [33, 34, 106, 146, 147] to possible coexisting phases and inelastic deformations. Assigned to each volumetric l and shear m relaxation process are respective relaxation times τ_l^V and τ_m^S , possibly temperature dependent:

$$\tau_l^V(\theta) = a_T^V(\theta; \theta_R^V) \tau_{Rl}^V(\theta_R^V) > 0, \quad \tau_m^S(\theta) a_T^S(\theta; \theta_R^S) \tau_{Rm}^S(\theta_R^S) > 0. \quad (3.39)$$

Volumetric and shear time-temperature shift functions are a_T^V and a_T^S , for which inverse logarithmic and Arrhenius forms are typical for polymers [4, 15, 148, 149]. Reference temperatures for bulk and shear relaxation are θ_R^V and θ_R^S , at which respective reference times τ_{RL}^V and τ_{Rm}^S are measured.

For shearing modes, stresses $\{\mathbf{Q}_m^S\}$ conjugate to configurational variables and total free energy $\Psi_S^r = \Psi_S^{G,r} = \Psi_S^{M,r}$ indistinguishable from glass and melt phases are, summing over $m = 1, \dots, M$,

$$\mathbf{Q}_m^S = -\frac{\partial \Psi_S^r}{\partial \mathbf{r}_m^S} = 2 \frac{\partial \Psi_m^S}{\partial \mathbf{C}^E}, \quad \Psi_S^r(\{\mathbf{r}_S\}, \mathbf{F}^E, \theta) = \sum_m \Psi_m^S(\mathbf{r}_m^S, \mathbf{F}^E, \theta) = \sum_m \int \frac{1}{2} \mathbf{Q}_m^S : d\mathbf{C}^E. \quad (3.40)$$

Recall $\mathbf{C}^E = (\mathbf{F}^E)^\top \mathbf{F}^E$. Dependence of Ψ_S^r and Ψ_m^S on phase fractions (ω, Ξ) is implicit through $\{\mathbf{r}_m^S\}$ and not written out in (3.40). Denote $D_t(\square) = (\dot{\square})$. Introduce energy functions $\hat{\Psi}_m^S$, $\hat{\Psi}_m^{G,S}$, and $\hat{\Psi}_m^{M,S}$ that are independent of configurational variables. Rate equations for internal stresses are

$$\dot{\mathbf{Q}}_m^S + \frac{\mathbf{Q}_m^S}{\tau_m^S} = 2D_t \left(\frac{\partial \hat{\Psi}_m^S}{\partial \mathbf{C}^E} \right), \quad \hat{\Psi}_m^S(\mathbf{F}^E, \theta, \omega) = (1 - \omega) \hat{\Psi}_m^{G,S}(\mathbf{F}^E, \theta) + \omega \hat{\Psi}_m^{M,S}(\mathbf{F}^E, \theta). \quad (3.41)$$

If relaxation times τ_m^S are constants, then a solution to (3.41) is the convolution integral [33, 34]

$$\mathbf{Q}_m^S(t) = \mathbf{Q}_{m0}^S \exp \left[\frac{t_0 - t}{\tau_m^S} \right] + \int_{t_0^+}^t \exp \left[\frac{s - t + t_0}{\tau_m^S} \right] D_s \left(2 \frac{\partial \hat{\Psi}_m^S}{\partial \mathbf{C}^E} \right) ds, \quad \mathbf{Q}_{m0}^S = 2 \frac{\partial \hat{\Psi}_m^S}{\partial \mathbf{C}^E} \Big|_{t=t_0}. \quad (3.42)$$

Cauchy stress contributions from shear viscoelasticity are, for isotropic logarithmic response and recalling $\mathbf{e}^E = \frac{1}{2} \ln[\mathbf{F}^E(\mathbf{F}^E)^\top]$, sums over m :

$$\boldsymbol{\sigma}_S^r = \frac{1}{J} \frac{\partial \Psi_S^r}{\partial \mathbf{e}^E} = \frac{2}{J} \mathbf{F}^E \frac{\partial \Psi_S^r}{\partial \mathbf{C}^E} (\mathbf{F}^E)^\top = \frac{1}{J} \sum_m \mathbf{F}^E \mathbf{Q}_m^S (\mathbf{F}^E)^\top = \bar{\boldsymbol{\sigma}}_S^r - p_S^r \mathbf{1}. \quad (3.43)$$

Let t_R be the time duration for a load history. For infinitely slow loading, $t_R/\tau_m^S \rightarrow \infty$, $\mathbf{Q}_m^S \rightarrow \mathbf{0}$, and $\boldsymbol{\sigma}_S^r \rightarrow \mathbf{0}$ is the equilibrium shear response if this holds for all m . For extremely rapid loading, $t_R/\tau_m^S \rightarrow 0$; thereby, $\boldsymbol{\sigma}_S^r$ reduces to an instantaneous (i.e., glassy) Cauchy stress contribution:

$$t_R/\tau_m^S \rightarrow 0 \quad [\forall m = 1, \dots, M] \Rightarrow \boldsymbol{\sigma}_S^r = \frac{1}{J} \sum_m \frac{\partial \hat{\Psi}_m^S}{\partial \mathbf{e}^E} = \frac{1 - \omega}{J} \sum_m \frac{\partial \hat{\Psi}_m^{G,S}}{\partial \mathbf{e}^E} + \frac{\omega}{J} \sum_m \frac{\partial \hat{\Psi}_m^{M,S}}{\partial \mathbf{e}^E}. \quad (3.44)$$

Kinetics from shear viscoelasticity is prescribed in what follows, where conjugate forces $\{\boldsymbol{\pi}_m^S\}$ are a subset of $\{\boldsymbol{\pi}\} = -\partial \Psi / \partial \{\boldsymbol{\alpha}\}$. Forces, evolution equations, and dissipation are [33, 34, 106]

$$\boldsymbol{\pi}_m^S = -\frac{\partial \Psi}{\partial \mathbf{r}_m^S} = f_S^E (1 - \Xi) \mathbf{Q}_m^S, \quad \dot{\mathbf{r}}_m^S = \frac{\mathbf{Q}_m^S}{\tau_m^S \mu_Y^S}, \quad \mathcal{D}_S^r = f_S^E (1 - \Xi) \sum_m \frac{\mathbf{Q}_m^S : \mathbf{Q}_m^S}{\tau_m^S \mu_Y^S} \geq 0; \quad (3.45)$$

$$\Psi_S^r = \Psi_S^{G,r} = \Psi_S^{M,r} = \sum_m \left[\hat{\Psi}_m^S - \int_{t_0}^t \mathbf{Q}_m^S : D_s \mathbf{r}_m^S ds \right]; \quad \mu_Y^S = \text{const} > 0; \quad (3.46)$$

Integration over time obtains shear configurational energy in (3.46). Initial conditions at $t = t_0$ are $\mathbf{r}_m^S = \mathbf{0}$, $\Psi_S^r(\{\mathbf{0}\}, \mathbf{F}^E, \theta) = \sum_m \hat{\Psi}_m^S(\mathbf{F}^E, \theta; \omega = 0)$.

Volumetric (i.e., bulk) viscoelasticity is addressed similarly to shear viscoelasticity. Thermo-viscoelastic coupling is enabled, namely, relaxation of Grüneisen's parameters [4, 117, 145]. For volumetric modes, conjugate stresses $\{\mathbf{Q}_l^V\}$ and free energy $\Psi_V^r = \Psi_V^{G,r} = \Psi_V^{M,r}$ are as follows:

$$\mathbf{Q}_l^V = -\frac{\partial \Psi_V^r}{\partial \mathbf{r}_l^V} = 2 \frac{\partial \Psi_l^V}{\partial \mathbf{C}^E}, \quad \Psi_V^r(\{\mathbf{r}_V\}, \mathbf{F}^E, \theta) = \sum_l \Psi_l^V(\mathbf{r}_l^V, \mathbf{F}^E, \theta) = \sum_l \int \frac{1}{2} \mathbf{Q}_l^V : d\mathbf{C}^E. \quad (3.47)$$

Dependence of Ψ_V^r and Ψ_l^V on (ω, Ξ) enters implicitly through kinetics for $\{\mathbf{r}_l^V\}$. Rate equations are as follows, including the bulk and thermoelastic coupling energies in $\hat{\Psi}_l^V$, $\hat{\Psi}_l^{G,V}$, and $\hat{\Psi}_l^{M,V}$:

$$\dot{\mathbf{Q}}_l^V + \frac{\mathbf{Q}_l^V}{\tau_l^V} = 2D_t \left(\frac{\partial \hat{\Psi}_l^V}{\partial \mathbf{C}^E} \right), \quad \hat{\Psi}_l^V(\mathbf{F}^E, \theta, \omega) = (1 - \omega) \hat{\Psi}_l^{G,V}(\mathbf{F}^E, \theta) + \omega \hat{\Psi}_l^{M,V}(\mathbf{F}^E, \theta). \quad (3.48)$$

In the special case that relaxation times τ_l^V are constants, then a solution to (3.48) is the integral

$$\mathbf{Q}_l^V(t) = \mathbf{Q}_{l0}^V \exp \left[\frac{t_0 - t}{\tau_l^V} \right] + \int_{t_0}^t \exp \left[\frac{s - t + t_0}{\tau_l^V} \right] D_s \left(2 \frac{\partial \hat{\Psi}_l^V}{\partial \mathbf{C}^E} \right) ds, \quad \mathbf{Q}_{l0}^V = 2 \frac{\partial \hat{\Psi}_l^V}{\partial \mathbf{C}^E} \Big|_{t=t_0}. \quad (3.49)$$

Cauchy stress contributions from bulk viscoelasticity are the following sums over $l = 1, \dots, L$:

$$\boldsymbol{\sigma}_V^r = \frac{1}{J} \frac{\partial \Psi_V^r}{\partial \mathbf{e}^E} = \frac{2}{J} \mathbf{F}^E \frac{\partial \Psi_V^r}{\partial \mathbf{C}^E} (\mathbf{F}^E)^\top = \frac{1}{J} \sum_l \mathbf{F}^E \mathbf{Q}_l^V (\mathbf{F}^E)^\top = -p_V^r \mathbf{1}. \quad (3.50)$$

As previously explained for shear, under infinitely slow loading $t_R/\tau_l^V \rightarrow \infty$, $\mathbf{Q}_l^V \rightarrow \mathbf{0}$, so $\boldsymbol{\sigma}_V^r \rightarrow \mathbf{0}$ if all modes are relaxed. For instantaneous loading, $t_R/\tau_l^V \rightarrow 0$ so that $\boldsymbol{\sigma}_V^r$ becomes a glassy stress:

$$t_R/\tau_l^V \rightarrow 0 \quad [\forall l = 1, \dots, L] \Rightarrow \boldsymbol{\sigma}_V^r = \frac{1}{J} \sum_l \frac{\partial \hat{\Psi}_l^V}{\partial \mathbf{e}^E} = \left[\frac{1 - \omega}{J} \sum_l \frac{\partial \hat{\Psi}_l^{G,V}}{\partial e_V^E} + \frac{\omega}{J} \sum_l \frac{\partial \hat{\Psi}_l^{M,V}}{\partial e_V^E} \right] \mathbf{1}. \quad (3.51)$$

Initial conditions at $t = t_0$ are $\mathbf{r}_l^V = \mathbf{0}$, $\Psi_V^r(\{\mathbf{0}\}, \mathbf{F}^E, \theta) = \sum_l \hat{\Psi}_l^V(\mathbf{F}^E, \theta; \omega = 0)$. Thermodynamic forces, evolution equations, dissipation, and bulk configurational energies are obtained from

$$\boldsymbol{\pi}_l^V = -\frac{\partial \Psi}{\partial \mathbf{r}_l^V} = f_V^E (1 - \Xi) \mathbf{Q}_l^V, \quad \dot{\mathbf{r}}_l^V = \frac{\mathbf{Q}_l^V}{\tau_l^V \mu_r^V}, \quad \mathcal{D}_V^r = f_V^E (1 - \Xi) \sum_l \frac{\mathbf{Q}_l^V : \mathbf{Q}_l^V}{\tau_l^V \mu_r^V} \geq 0; \quad (3.52)$$

$$\Psi_V^r = \Psi_V^{G,r} = \Psi_V^{M,r} = \sum_l \left[\hat{\Psi}_l^V - \int_{t_0}^t \mathbf{Q}_l^V : D_s \mathbf{r}_l^V ds \right]; \quad \mu_r^V = \text{const} > 0. \quad (3.53)$$

Extending Ref. [33], contributions to temperature rate arise from shear and bulk viscoelasticity:

$$\begin{aligned} \sum_m \theta (\partial^2 \Psi_S^r / \partial \mathbf{r}_m^S \partial \theta) : \dot{\mathbf{r}}_m^S &= -2\theta \sum_m (\partial^2 \Psi_m^S / \partial \mathbf{C}^E \partial \theta) : \dot{\mathbf{r}}_m^S \\ &= -\theta \sum_m [(\mathbf{F}^E)^{-1} (\partial^2 \Psi_m^S / \partial \mathbf{e}^E \partial \theta) (\mathbf{F}^E)^{-\top}] : \dot{\mathbf{r}}_m^S, \end{aligned} \quad (3.54)$$

$$\begin{aligned} \sum_l \theta (\partial^2 \Psi_V^r / \partial \mathbf{r}_l^V \partial \theta) : \dot{\mathbf{r}}_l^V &= -2\theta \sum_l (\partial^2 \Psi_l^V / \partial \mathbf{C}^E \partial \theta) : \dot{\mathbf{r}}_l^V \\ &= -\theta \sum_l [(\mathbf{F}^E)^{-1} (\partial^2 \Psi_l^V / \partial \mathbf{e}^E \partial \theta) (\mathbf{F}^E)^{-\top}] : \dot{\mathbf{r}}_l^V. \end{aligned} \quad (3.55)$$

3.4 Plasticity

The plasticity model comprises three main components. Described first are free energy, anisotropic hardening, and evolution of tensor internal variable \mathbf{A} associated with alignment and stretching of molecular chains in both glassy and rubbery regimes. Described second are energy and flow stress contributions, and coupled kinetic laws, for free volume φ and internal variable ζ associated with deformation induced disordering in the glassy phase. Described third are the flow rule for traceless symmetric strain rate $\dot{\mathbf{\epsilon}}^P$ and commensurate dissipation from shear yielding.

Multiple models exist that, depending on numbers of governing equations and calibrated parameters, can match complex finite stress-strain behavior of amorphous polymers across ranges of strain, strain rate, and temperature, most often for uniaxial compressive stress states [2–4, 9, 11, 12, 16, 25–27, 42, 44–46, 48, 50, 150]. Many recent works draw heavily from their immediate predecessors, and differences among theories can be subtle. Here, representative model features follow from this literature, balancing descriptive capability with model complexity and numbers of parameters. A single scalar hardening parameter ζ is used [2, 14, 16], noting multiple entries of $\{\zeta\}$ have been proposed to address crystallization or enhanced hardening at large strain [26, 27, 44] or distinct mechanisms across the glass transition [3].

As in cited works, many “constants” in what follows can be made temperature- or strain-rate dependent to better fit complex data. However, nonlinear temperature dependence of inelastic free energy is discouraged to avoid affecting specific heat. Dependence of free energy on strain rate is discouraged to avoid thermodynamic inconsistencies. Previous works invoked a glass transition temperature θ_G that depends on strain rate and also enters the definitions of elastic constants and other contributors to free energy [2, 3, 50]. This approach seems acceptable when the strain rate is constant, but thermodynamic inconsistencies and unusual viscoelastic effects can arise if the strain rate varies during the load history. Such issues are avoided in the present approach by using an order parameter ω to account for rate- and pressure-dependent melting, rather than a transient θ_G .

Plastic free energy densities in (3.10) and (3.11) are partitioned, without ϕ dependence, as

$$\Psi^{*,P}(\zeta, \mathbf{A}, \varphi, \phi, \theta) = \Psi_A^{*,P}(\mathbf{A}, \theta) + \Psi_\zeta^{*,P}(\zeta, \varphi). \quad (3.56)$$

The evolution law for the tensor \mathbf{A} , initial condition, and network plastic stretch λ^P are [14, 16]

$$\dot{\mathbf{A}} = \mathbf{A} \dot{\mathbf{\epsilon}}^P + \dot{\mathbf{\epsilon}}^P \mathbf{A}, \quad \mathbf{A}(\mathbf{X}, t_0) = \mathbf{1}, \quad \lambda^P = (\frac{1}{3} \text{tr} \mathbf{A})^{1/2}; \quad \bar{\mathbf{A}} = \mathbf{A} - (\lambda^P)^2 \mathbf{1}. \quad (3.57)$$

When $\mathbf{D}^P(\mathbf{X}, t) = \dot{\mathbf{\epsilon}}^P(\mathbf{X}, t) \forall t$, then $\mathbf{A} = \mathbf{F}^P(\mathbf{F}^P)^\top$. Denote $N^{*,P}(\theta) > 0$ the temperature dependent number of statistical links per polymer chain [9] with reference value $N_0^P = N^{G,P}(\theta_0)$. Isothermal network locking stretch is defined as $\lambda_L^P = (N_0^P)^{1/2}$. Denote Langevin function $\mathcal{L}(\square) = \coth(\square) - 1/\square$ and approximate inverse by $\mathcal{L}^{-1}(\square) \approx \square(3 - \square^2)/(1 - \square^2)$ [151]. Normalized stretch is $\lambda_N^P = \lambda^P / \lambda_L^P$. Free energy contributions from chain alignment and finite inelastic stretch processes

in glassy and melt phases extend Refs. [2, 13, 16, 19, 46]:

$$\Psi_A^{G,P}(\lambda_N^P(\mathbf{A}), \theta) = \mu_A^G(\theta)N^{G,P}(\theta) \left[\lambda_N^P \mathcal{L}^{-1}(\lambda_N^P) + \ln \frac{\mathcal{L}^{-1}(\lambda_N^P)}{\sinh\{\mathcal{L}^{-1}(\lambda_N^P)\}} \right. \\ \left. - (1/\lambda_L^P) \mathcal{L}^{-1}(1/\lambda_L^P) - \ln \frac{\mathcal{L}^{-1}(1/\lambda_L^P)}{\sinh\{\mathcal{L}^{-1}(1/\lambda_L^P)\}} \right], \quad (3.58)$$

$$\Psi_A^{M,P}(\lambda_N^P(\mathbf{A}), \theta) = \mu_A^M(\theta)N^{M,P}(\theta) \left[\lambda_N^P \mathcal{L}^{-1}(\lambda_N^P) + \ln \frac{\mathcal{L}^{-1}(\lambda_N^P)}{\sinh\{\mathcal{L}^{-1}(\lambda_N^P)\}} \right. \\ \left. - (1/\lambda_L^P) \mathcal{L}^{-1}(1/\lambda_L^P) - \ln \frac{\mathcal{L}^{-1}(1/\lambda_L^P)}{\sinh\{\mathcal{L}^{-1}(1/\lambda_L^P)\}} \right]; \quad (3.59)$$

$$\mu_A^G = \langle \mu_{A0} - \mu_{A\theta}(\theta - \theta_0) \rangle, \quad \mu_A^M = \langle \mu_{A0} - \mu_{A\theta}(\theta_G - \theta_0) \rangle \theta / \theta_G; \quad (3.60)$$

$$N^{G,P} = \langle N_0^P + N_\theta^P(\theta - \theta_0) \rangle, \quad N^{M,P} = \langle N_0^P + N_\theta^P(\theta_G - \theta_0) \rangle. \quad (3.61)$$

Angled brackets preclude negative values: $\langle \square \rangle = \frac{1}{2}(\square + |\square|)$. Material constants are $\mu_{A0} \geq 0$, $\mu_{A\theta}$, $N_0^P > 0$, and N_θ^P .

Denote by $\tau^P = \tau^E - \tau^A \geq 0$ the net shear stress in the flow direction, with applied elastic part τ^E and back-stress part τ^A . Define $\dot{\gamma}^P \geq 0$ as the plastic shearing rate and $\bar{\mathbf{N}}^P$ the flow direction tensor that is symmetric, traceless, and of unit magnitude. Net dissipation from shear flow $\dot{\mathbf{\epsilon}}^P$ and $\dot{\mathbf{A}}$, using (3.57) and isotropy [25] of $\Psi_A^{*,P}(\text{tr}\mathbf{A}, \theta)$, is the following:

$$\mathfrak{D}_A^P = \bar{\mathbf{M}}^E : \dot{\mathbf{\epsilon}}^P - (\partial_{\mathbf{A}} \Psi) : \dot{\mathbf{A}} \\ = f_S^E (1 - \Xi) [(1 - \omega) \bar{\mathbf{M}}_S^{G,E} + \omega \bar{\mathbf{M}}_S^{M,E} + \bar{\mathbf{M}}_S^Y] : \dot{\mathbf{\epsilon}}^P \\ - \{2f_S^E (1 - \Xi) [(1 - \omega) \partial_{\mathbf{A}} \Psi^{G,P} + \omega \partial_{\mathbf{A}} \Psi^{M,P}] \mathbf{A}\} : \dot{\mathbf{\epsilon}}^P \\ = (\bar{\mathbf{M}}^E - \bar{\mathbf{M}}^A) : \dot{\mathbf{\epsilon}}^P = \bar{\mathbf{M}}^P : \dot{\mathbf{\epsilon}}^P = \tau^P \dot{\gamma}^P = |\tau^E - \tau^A| \dot{\gamma}^P \geq 0; \quad (3.62)$$

$$\bar{\mathbf{M}}_S^{*,E} = \frac{1}{2} J [(\mathbf{F}^E)^T \bar{\boldsymbol{\sigma}}_S^{*,E} (\mathbf{F}^E)^{-T} + (\mathbf{F}^E)^{-1} \bar{\boldsymbol{\sigma}}_S^{*,E} \mathbf{F}^E], \\ \bar{\mathbf{M}}_S^Y = \frac{1}{2} J [(\mathbf{F}^E)^T \bar{\boldsymbol{\sigma}}_S^Y (\mathbf{F}^E)^{-T} + (\mathbf{F}^E)^{-1} \bar{\boldsymbol{\sigma}}_S^Y \mathbf{F}^E]; \\ \bar{\mathbf{M}}^P = \sqrt{2} \tau^P \bar{\mathbf{N}}^P, \quad \bar{\mathbf{N}}^P = \bar{\mathbf{M}}^P / (\bar{\mathbf{M}}^P : \bar{\mathbf{M}}^P)^{1/2}, \quad \dot{\mathbf{\epsilon}}^P = \frac{1}{\sqrt{2}} \dot{\gamma}^P \bar{\mathbf{N}}^P; \\ \tau^P = \frac{1}{\sqrt{2}} \bar{\mathbf{M}}^P : \bar{\mathbf{N}}^P = \frac{1}{\sqrt{2}} (\bar{\mathbf{M}}^P : \bar{\mathbf{M}}^P)^{1/2}, \quad \dot{\gamma}^P = \sqrt{2} (\dot{\mathbf{\epsilon}}^P : \dot{\mathbf{\epsilon}}^P)^{1/2}; \quad (3.63)$$

$$\bar{\mathbf{M}}^A = 2 \left[\frac{\partial \Psi}{\partial \mathbf{A}} \mathbf{A} - \frac{1}{3} \text{tr} \left(\frac{\partial \Psi}{\partial \mathbf{A}} \mathbf{A} \right) \mathbf{1} \right] = f_V^E (1 - \Xi) \left[\frac{(1 - \omega)}{3\lambda^P} \frac{\partial \Psi_A^{G,P}}{\partial \lambda^P} + \frac{\omega}{3\lambda^P} \frac{\partial \Psi_A^{M,P}}{\partial \lambda^P} \right] \bar{\mathbf{A}} \\ = \frac{f_S^E (1 - \Xi)}{3N_0^P \lambda_N^P} [(1 - \omega) \mu_A^G N^{G,P} + \omega \mu_A^M N^{M,P}] \mathcal{L}^{-1}(\lambda_N^P) \bar{\mathbf{A}} \\ \approx \frac{f_S^E (1 - \Xi)}{3N_0^P} [(1 - \omega) \mu_A^G N^{G,P} + \omega \mu_A^M N^{M,P}] \left[\frac{3 - (\lambda_N^P)^2}{1 - (\lambda_N^P)^2} \right] \bar{\mathbf{A}}. \quad (3.64)$$

Following Refs. [14, 16, 19, 25–27, 44], ζ and φ account for initial hardening, a yield peak, and subsequent strain softening associated with network disorder. Free volume φ in this context only measures plastic structural disorder and its effect on plastic softening [17]. It does not account for changes in some thermo-physical properties such as thermal expansion and compressibility. The latter are widely correlated to definitions of “free volume” that increases across the glass transition [15, 18]. Rather, such correlations are captured here by different thermoelastic properties for glass and melt. Because residual free volume change does not appreciably affect mass density [16, 25],

$$c_\varphi \rightarrow 0. \quad (3.65)$$

The cooperative-model flow rule of Ref. [2] is used, whereby the isotropic shear resistance associated with molecular defect rearrangements vanishes identically in the melt phase. Thus, from (3.65), values of ζ and φ are inconsequential for the melt, and likewise for decomposed products, and their time evolution is controlled by properties of the glassy solid. Material parameters $\tau_0^\zeta, \mu_\zeta^G, a_\varphi, b_\varphi, \tau_\infty^\zeta$, and φ_∞ are now introduced. Under steady flow, $\tau^\zeta \rightarrow \tau_\infty^\zeta$ and $\varphi \rightarrow \varphi_\infty$ as $t \rightarrow \infty$. The following system [13, 16, 19] of ordinary differential equations (ODEs) then suffices for kinetics of ζ and φ , where τ^ζ is flow resistance associated with ζ :

$$\tau^\zeta = \tau_0^\zeta + \mu_\zeta^G \zeta, \quad \zeta(\mathbf{X}, t_0) = 0, \quad \varphi(\mathbf{X}, t_0) = 0; \quad \tau_\varphi^\zeta = \tau_\infty^\zeta [1 + b_\varphi (\varphi_\infty - \varphi)]; \quad (3.66)$$

$$\dot{\tau}^\zeta = \mu_\zeta^G (1 - \tau^\zeta / \tau_\varphi^\zeta) \dot{\gamma}^P; \quad \dot{\varphi} = a_\varphi (\tau^\zeta / \tau_\infty^\zeta - 1) \dot{\gamma}^P; \quad \dot{\zeta} = \dot{\tau}^\zeta / \mu_\zeta^G = (1 - \tau^\zeta / \tau_\varphi^\zeta) \dot{\gamma}^P. \quad (3.67)$$

The scalar plastic shearing rate is furnished by the cooperative model of Refs. [2, 46], modified to account for mixed phase regions $\omega \in (0, 1)$ and possible decomposition $\Xi \in (0, 1]$. When $\omega = \Xi = 0$, the present flow rule reduces to that of the glassy material in the original reference [12, 45], and when $\omega = 1$, it reduces to that of the rubbery material [2]. As $\Xi \rightarrow 1$, the polymer decomposes into chemical products and plastic flow ceases to have physical relevance. Herein,

$$\dot{\gamma}^P = (1 - \Xi) \dot{\gamma}_0 \exp \left(\frac{-H_\beta}{k_B \theta} \right) \left[(1 - \omega) + \omega \exp \left\{ \frac{(\ln 10) c_1^G (\theta - \theta_G)}{c_2^G + (\theta - \theta_G)} \right\} \right] \left[\sinh \left(\frac{\tau^F V_F}{2k_B \theta} \right) \right]^{1/m}, \quad (3.68)$$

where $\dot{\gamma}_0 > 0$ and $m \geq 0$ are reference strain rate and rate sensitivity, k_B is Boltzmann’s constant, and activation energy for secondary relaxation is H_β . Activation volume is V_F , and c_1^G and c_2^G are parameters. For rate independence, $m \rightarrow 0$. The effective flow stress is defined akin to Ref. [27]:

$$\tau^F = \langle \tau^E - \{ \tau^A + f_S^E (1 - \omega) (1 - \Xi) (1 - \phi) \langle \tau^\zeta - \alpha_\theta^F (\theta - \theta_0) + \alpha_p^F B_0^{G,E} \langle -e_V^E \rangle \} f_R^P \rangle. \quad (3.69)$$

Reduction in flow resistance by f_S^E and $1 - \phi$ accounts for softening from fractures [14] and voids [19, 152], respectively. Thermal softening is accelerated by constant $\alpha_\theta^F \approx \tau_0^\zeta / (\theta_G - \theta_0) > 0$ [2]. Pressure hardening in compression [11, 115] is enabled by constant $\alpha_p^F > 0$. Scalar function $f_R^P = f_R^P (e_V^E, \theta) \geq 0$ scales the total flow resistance to account for complex strength response under shock loading [113, 114] as explained in Section 4.1 for PMMA. A more elaborate thermodynamic theory spanning the glass transition has been implemented [3] that captures some physics missing in (3.68) for complex load histories, albeit with more parameters. See Ref. [3].

The plasticity model is complete upon choosing the rightmost terms in (3.56). For simplicity, assumed here is $\Psi_\zeta^{G,P} = \Psi_\zeta^{M,P} = \Psi_\zeta^P$. These functions are otherwise left generic. In principle, they could be calibrated to temperature data (e.g., Taylor-Quinney factors [140]) if of sufficient fidelity. Weighted contributions to internal dissipation from rates of ζ and φ , thus affecting $\dot{\theta}$, are

$$\mathfrak{D}^\zeta = -\partial_\zeta \Psi \dot{\zeta} = -(1 - \Xi)(\partial_\zeta \Psi_\zeta^P) f_S^E (1 - \tau^\zeta / \tau_\phi^\zeta) \dot{\gamma}^P, \quad (3.70)$$

$$\mathfrak{D}^\varphi = -\partial_\varphi \Psi \dot{\varphi} = -(1 - \Xi)(\partial_\varphi \Psi_\zeta^P) f_S^E a_\varphi (\tau^\zeta / \tau_\infty^\zeta - 1) \dot{\gamma}^P. \quad (3.71)$$

3.5 Fracture

The fracture framework consists of the phase-field formulation of Section 2.3 for order parameter ξ , where the net driving force Φ remains to be prescribed, and the kinetic law for porosity ϕ whose rate enters kinematic relation (3.3) with direction \mathbf{N}_ϕ also to be prescribed. Herein, the phase-field model, where ξ simultaneously addresses degradation from brittle or ductile fractures, draws from prior phase-field descriptions of amorphous polymers undergoing combined inelastic shear-yielding and crazing [14, 19, 75, 134, 135]. The same sources, along with continuum damage mechanics models [13, 39], are consulted for the porosity representation. A damage instantiation criterion based on maximum principal stress is used to activate brittle fracture from crazing, and an instantiation criterion based on local plastic stretch is used to instantiate ductile tearing or chain scission [13, 14]. For a polymer with low entanglement density such as PMMA, crazing applies for the nominally brittle glassy regime. The scission mechanism is enabled for the rubbery melt since crazing is typically irrelevant above the glass transition. The decomposed phase of dissociated products is essentially already “fractured” and “porous”; ξ and ϕ are unaffected by energy density of the decomposed phase that, according to Section 3.2, cannot support tensile pressure regardless.

First consider the phase-field formulation. Define a surface energy density per unit area Γ_ξ , akin to twice the fracture toughness, a length constant $l_\xi \geq 0$ that may or may not differ from gradient regularizer l of Section 2.3, and a threshold resistance energy per unit volume inhibiting damage initiation $R_\xi^* \geq 0$. Letting $\Gamma_\xi^G, R_\xi^G, \Gamma_\xi^M$, and R_ξ^M denote non-negative temperature-dependent functions for glass and melt,

$$\Gamma_\xi(\theta, \omega, \Xi) = (1 - \Xi)[(1 - \omega)\Gamma_\xi^G(\theta) + \omega\Gamma_\xi^M(\theta)], \quad (3.72)$$

$$R_\xi(\theta, \mathbf{e}^E, \omega, \Xi) = (1 - \Xi)[(1 - \omega)R_\xi^G(\theta, \mathbf{e}^E) + \omega R_\xi^M(\theta, \mathbf{e}^E)]. \quad (3.73)$$

Thresholds R_ξ^G and R_ξ^M can depend on strain \mathbf{e}^E as well as θ to enable fracture resistance at high confining pressure [64, 65]. The elastic driving force contribution to Φ allows brittle fracture even in the absence of porosity or shear yielding. It comprises usual dilatational and deviatoric elastic strain energy densities [14, 121, 141, 153] as well as viscoelastic configurational energies [106]:

$$F_\xi^E = (1 - \Xi)\{(1 - \omega)[\Psi_V^{G,E} \mathsf{H}(e_V^E) + \Psi_S^{G,E}] + \omega[\Psi_V^{M,E} \mathsf{H}(e_V^E) + \Psi_S^{M,E}] + [\Psi_V^r \mathsf{H}(e_V^E) + \Psi_S^r]\}. \quad (3.74)$$

Denote $c_\xi^\phi \geq 0$ and $c_\xi^P \geq 0$ respective constants for quadratic dependence of order-parameter kinetics on porosity [19, 75, 134] and for ductile fracture induced quadratically by isochoric plastic

stretch [19]. The net driving force function is finally posited as

$$\Phi(\mathbf{e}^E, \theta, \{\mathbf{Y}\}, \lambda^P(\mathbf{A}), \phi, \omega, \Xi) = \frac{l_\xi \langle F_\xi^E(\mathbf{e}^E, \theta, \{\mathbf{Y}\}, \omega, \Xi) + (1 - \Xi)[c_\xi^\phi \phi^2 + c_\xi^P (\lambda^P - 1)^2] - R_\xi(\mathbf{e}^E, \theta, \omega, \Xi) \rangle}{\Gamma_\xi(\theta, \omega, \Xi)}. \quad (3.75)$$

Now consider inelastic flow from dilatational deformations. Similar to Ref. [39], the porosity rate is decomposed additively into contributions from several mechanisms, here crazing in the brittle glass phase and chain scission in the ductile melt. Following Refs. [13, 14, 19, 75, 134], a non-negative scalar strain rate $\dot{\varepsilon}^\phi$ is used to prescribe, in power-law form, the porosity rate $\dot{\phi}$:

$$\dot{\varepsilon}^\phi = \frac{\dot{\phi}}{1 - \phi} = (1 - \Xi)(1 - \omega)\varkappa_G \dot{\varepsilon}_0 \left(\frac{\langle M_\phi^E \rangle}{f_V^E S_\phi^G} \right)^{1/n} + (1 - \Xi)\omega \varkappa_M \dot{\varepsilon}_0 \left(\frac{\langle M_\phi^E \rangle}{f_V^E S_\phi^M} \right)^{1/n} \geq 0. \quad (3.76)$$

Reference strain rate $\dot{\varepsilon}_0 > 0$ and rate sensitivity $n > 0$ are assigned as the same constants for each mechanism; distinct values could be used, if needed, to match data [14]. Indicator functions \varkappa_G and \varkappa_M acquire values of 0 or 1 depending on local stress or plastic stretch state. A spectral decomposition of Mandel stress \mathbf{M}^E is, with principal components M_I^E and directions \mathbf{n}_I^E ,

$$\mathbf{M}^E = \sum_{I=1}^3 M_I^E \mathbf{n}_I^E \otimes \mathbf{n}_I^E; \quad M_1^E \geq M_2^E \geq M_3^E; \quad \text{tr} \mathbf{M}^E = \sum_{I=1}^3 M_I^E = -3Jp^E. \quad (3.77)$$

In (3.5) and (3.76), the opening direction and driving force are prescribed as the direction and magnitude of maximum principal (Mandel) stress, similar to Refs. [13, 14, 19, 75, 134]:

$$\mathbf{n}_\phi(\mathbf{X}, t) = \mathbf{n}_1^E(\mathbf{X}, t); \quad M_\phi^E = \mathbf{M}^E : \mathbf{n}_\phi \otimes \mathbf{n}_\phi = \mathbf{M}^E : \mathbf{N}_\phi = M_1^E. \quad (3.78)$$

Unlike Refs. [14, 19], but like other cited works, $\mathbf{n}_\phi(\mathbf{X}, t)$ can evolve with time. If \mathbf{M}^E has repeated maximum eigenvalues, one of these must be chosen arbitrarily for (3.78). Indicator functions for crazing [19, 75, 134] and ductile fracture [13, 14] are, with scaling $f_V^E \tilde{M}_\phi^E = M_\phi^E$ and $f_V^E \tilde{p}^E = p^E$,

$$\varkappa_G = \mathsf{H}(M_\phi^E) \mathsf{H}(-p^E) \mathsf{H}(f_\phi^G), \quad f_\phi^G = \tilde{M}_\phi^E - [c_1^\phi - c_2^\phi / (J\tilde{p}^E) - 3v_0^{G,E} J\tilde{p}^E / (1 + v_0^{G,E})]; \quad (3.79)$$

$$\varkappa_M = \mathsf{H}(M_\phi^E) \mathsf{H}(\lambda^P - \lambda_\phi^P); \quad \lambda_\phi^P = \text{const} > 1. \quad (3.80)$$

Material constants for craze initiation are c_1^ϕ and c_2^ϕ , and $v_0^{G,E} = (3B_0^{G,E} - 2G_0^{G,E}) / (6B_0^{G,E} + 2G_0^{G,E})$ is Poisson's ratio. Resisting stresses in (3.76) are driving stresses at instantiation times t_ϕ^G and t_ϕ^M of each mechanism [14]:

$$S_\phi^G(\mathbf{X}, t \geq t_\phi^G) = \tilde{M}_\phi^E(\mathbf{X}, t_\phi^G(\mathbf{X})), \quad t_\phi^G(\mathbf{X}) = \min_{s \in (t_0, t]} \{\text{arg0}[\varkappa_G(\mathbf{X}, s) - 1]\}; \quad (3.81)$$

$$S_\phi^M(\mathbf{X}, t \geq t_\phi^M) = \tilde{M}_\phi^E(\mathbf{X}, t_\phi^M(\mathbf{X})), \quad t_\phi^M(\mathbf{X}) = \min_{s \in (t_0, t]} \{\text{arg0}[\varkappa_M(\mathbf{X}, s) - 1]\}. \quad (3.82)$$

Dissipation from porosity is non-negative, noting $\Psi_\zeta^{G,P} = \Psi_\zeta^{M,P}$ in (3.56) does not depend on ϕ :

$$\mathfrak{D}^\phi = (1 - \Xi) M_\phi^E \dot{\epsilon}_0 \left[(1 - \omega) \varkappa_G \left(\frac{\langle M_\phi^E \rangle}{f_V^E S_\phi^G} \right)^{1/n} + \omega \varkappa_M \left(\frac{\langle M_\phi^E \rangle}{f_V^E S_\phi^M} \right)^{1/n} \right] \geq 0. \quad (3.83)$$

To avoid computational complexity, as in prior treatments [14, 19], (3.68) can be appended with multiplier $(1 - \varkappa_G)(1 - \varkappa_M)$ to prevent shear yielding and crazing or scission simultaneously at \mathbf{X} .

3.6 Melting

Recall “melting” refers to transition from a glassy to rubbery state. At ambient pressure and null loading rate, this second-order transition occurs as temperature is raised to a value in the vicinity of a constant θ_G characteristic of the polymer. The present framework also captures the reverse transition, from rubbery to glassy state, beginning when the polymer melt is cooled from high temperature to the vicinity of θ_G . Typically the rubbery phase has a higher specific heat, a higher thermal expansion coefficient, and lower mechanical stiffness than the glass. Representative curves are available in Refs. [3, 4, 154]. Calorimetry and mechanical experiments show that rapid thermo-physical property variations in amorphous polymers occur over a temperature window $\theta_G \pm \Delta\theta$, where $\Delta\theta$ is on the order of 5 to 10 K [43, 50]. Evidence that the reduction in stiffness decreases with increasing loading rate [2, 43, 50] implies a time scale is involved in the melt process. However, this time scale τ_ω is expected to be small (e.g., relative to 1 second) since specimens preheated above θ_G respond to very high-rate loading in at least a partially glassy manner [2, 46, 79], meaning the melt acquires glassy stiffness very early in the dynamic deformation process. Experiments also show that the melt process is inhibited by compressive pressure [4, 155], presumably because the vibrational free volume increase reflected by the increase in thermal expansivity is restricted.

Previous plasticity models for amorphous polymers traversing the glass transition assigned a variable glass transition temperature that depends on local effective strain rate [3, 43, 50]. This transition temperature then enters thermodynamic (e.g., hyperelastic) energy potentials via elastic coefficients that depend explicitly on the variable glass transition temperature. Such an approach appears most theoretically sound if strain rate is fixed during a loading history. However, if strain rate varies with time, then thermodynamic potentials acquire implicit dependence on rate that could become incompatible with original modeling assumptions such as hyperelastic response.

Circumventing this issue, in the present formulation the transition from glassy to rubbery response is described by an order parameter $\omega(t) \in [0, 1]$ that evolves with thermodynamic state (including temperature, pressure, and strain rate) and enters free energy Ψ of (3.9), along with various kinetic laws, using a constant θ_G . The kinetic law used for ω has similarities to prior models for first-order phase or structural transformations in crystalline materials [84, 107, 144, 152, 156, 157]. However, the glass-melt transition is viewed as a second-order solid state transformation [108, 109] in that density ρ and energy Ψ stay constant if transformation occurs in the ideal limit of fixed $\theta = \theta_G$ under null elastic and plastic straining. Entropy and pressure need not remain constant, however, if specific heat and Grüneisen parameters vary independently across the transition.

Net dissipation \mathfrak{D}_ω and thermodynamic driving force for melting F_ω (i.e., contribution from ω to $\{\boldsymbol{\pi}\}$) are defined consistently with (2.22), $\Psi_V^{G,Y} = \Psi_V^{M,Y}$, $\Psi_S^{G,Y} = \Psi_S^{M,Y}$, and $\Psi_\zeta^{G,P} = \Psi_\zeta^{M,P}$ as

$$\begin{aligned}\mathfrak{D}^\omega &= F_\omega \dot{\omega}; \quad F_\omega = -\partial_\omega \Psi = (1 - \Xi) \{ f_V^E [\Psi_V^{G,E} + \Psi_\beta^{G,E}] + f_S^E [\Psi_S^{G,E} + \Psi_A^{G,P}] + \Psi^{G,\theta} \\ &\quad - (f_V^E [\Psi_V^{M,E} + \Psi_\beta^{M,E}] + f_S^E [\Psi_S^{M,E} + \Psi_A^{M,P}] + \Psi^{M,\theta}) \}. \quad (3.84)\end{aligned}$$

As analyzed in Refs. [144, 152], $F_\omega = F_\omega(\boldsymbol{e}^E, \theta, \mathbf{A}, \xi, \Xi)$ is related to the Gibbs free energy difference between coexisting phases. Introduce by $\tau_\omega = \tau_\omega(\theta) > 0$ a characteristic relaxation time for transition kinetics that can depend on temperature if warranted. Denote by $R_\omega \geq 0$ a transition resistance function of thermodynamic state and deformation rate, with dimensions of energy per unit volume. Denote a metastable melt fraction by $\tilde{\omega}(\mathbf{X}, t) \in [0, 1]$. The following kinetic law enforces $\mathfrak{D}^\omega \geq 0$ for forward (melting, $\dot{\omega} > 0$) and reverse (freezing, $\dot{\omega} < 0$) transitions at (\mathbf{X}, t) :

$$\tau_\omega \dot{\omega} = \begin{cases} (\tilde{\omega} - \omega) \mathbb{H}(F_\omega), & [\text{if } \omega < \tilde{\omega} \text{ and } F_\omega > R_\omega \geq 0]; \\ (\tilde{\omega} - \omega) \mathbb{H}(-F_\omega), & [\text{if } \omega > \tilde{\omega} \text{ and } -F_\omega > R_\omega \geq 0]; \\ 0, & [\text{otherwise}]. \end{cases} \quad (3.85)$$

The first condition in (3.85) pertains to glass \rightarrow melt, the second to melt \rightarrow glass, and the third to a stationary state.

Consider forward transitions wherein $F_\omega > R_\omega$. The local metastable value of ω is motivated from differential relationship [144, 152, 156, 157] $d\omega = (1 - \omega)d\mathbb{F}$, where dimensionless forward transition driving force $\mathbb{F} = F_\omega/\beta_\omega$. Proportionality factor $\beta_\omega > 0$ for forward transformation is constant for simplicity. Transition begins when driving force exceeds normalized resistance R_ω/β_ω . Integrating over melt process $\omega : 0 \rightarrow \tilde{\omega}$ to the current value of driving force F_ω produces

$$F_\omega > R_\omega \geq 0 \Rightarrow \int_0^{\tilde{\omega}} \frac{d\omega}{1 - \omega} = \int_{R_\omega/\beta_\omega}^{F_\omega/\beta_\omega} d\mathbb{F} \Rightarrow \tilde{\omega} = 1 - \exp \left[-\frac{F_\omega - R_\omega}{\beta_\omega} \right]. \quad (3.86)$$

Now consider reverse transformations: $-F_\omega > R_\omega$. The differential relation is $d\omega = -\omega d\mathbb{F}$ with $\mathbb{F} = -F_\omega/\beta_\omega$. Since θ_G should be unchanged when the polymer is heated to melt or cooled to freeze, β_ω and R_ω should be the same proportionality constant and energy barrier for forward and reverse transformation. Integrating over the freezing process $\omega : 1 \rightarrow \tilde{\omega}$ gives¹

$$-F_\omega > R_\omega \geq 0 \Rightarrow \int_{\tilde{\omega}}^1 \frac{d\omega}{\omega} = - \int_{-F_\omega/\beta_\omega}^{R_\omega/\beta_\omega} d\mathbb{F} \Rightarrow \tilde{\omega} = \exp \left[\frac{F_\omega + R_\omega}{\beta_\omega} \right]. \quad (3.87)$$

The following are obtained for specific polymers by using (3.86) or (3.87) in conjunction with experimental glass transition data: free energy difference $\Psi_0^{M,\theta} = \text{const}$ between coexisting glass and melt at the same temperature introduced in (3.37), proportionality factor $\beta_\omega = \text{const} > 0$, and resistance function $R_\omega \geq 0$. The latter measures the increase in effective transition start temperature with increasing pressure and strain rate [3, 4, 43, 50, 155] and is of the following assumed form:

$$R_\omega = R_\omega(\langle -e_V^E \rangle, \{\mathbf{Y}_V\}, \theta, \dot{\epsilon}); \quad \dot{\epsilon} = \sqrt{2}(\mathbf{d} : \mathbf{d})^{1/2}; \quad R_\omega(0, \{\mathbf{0}\}, \theta \in (\theta_1, \theta_2), \dot{\epsilon} \leq \dot{\epsilon}_\omega) = 0. \quad (3.88)$$

¹Upper integration limits should be 1 in (4.48) and (2.113) of Refs. [144, 152]; these misprints are corrected here.

As in Refs. [3, 43, 50], rate dependence is encapsulated by the scalar total strain rate $\dot{\varepsilon}$, where $\dot{\varepsilon}_\omega = \text{const} > 0$ is a cutoff below which viscous effects do not affect the transition. As typical data only probe effects of compressive pressure [155], dependence on volume is restricted to negative elastic volumetric strain e_V^E . Volumetric configurational variables $\{\mathbf{Y}_V\}$ are included in arguments of R_ω to account for dynamic stiffening of the bulk modulus. Resistance vanishes at null deformation within range $\theta_1 < \theta < \theta_2$, where $\theta_1 \ll \theta_G$ and $\theta_2 \gg \theta_G$. Recalling $F_\omega = F_\omega(\mathbf{e}^E, \theta, \mathbf{A}, \xi, \Xi)$ from (3.84), and noting $R_\omega = 0$ at steady state and null elastic volume change, energy difference $\Psi_0^{M,\theta}$ is obtained from metastability condition $F_\omega(\mathbf{0}, \theta_G, \mathbf{1}, 0, 0) = R_\omega = 0$. From (3.36) and (3.37),

$$\Psi_0^{M,\theta} = (c_{00}^M - c_{00}^G)[\theta_G \ln(\theta_G/\theta_0) - (\theta_G - \theta_0)] + \frac{1}{2}(c_\theta^M - c_\theta^G)(\theta_G - \theta_0)^2. \quad (3.89)$$

Lastly, β_ω is determined from the “half-width” $\delta\theta_G$ of the transition region in θ versus $\tilde{\omega}$ space, on the order of 5-10 K for polymers of interest [43, 50]. Again enforce steady and null strain conditions and $\theta \in (\theta_1, \theta_2)$ so $R_\omega = 0$. Let $1 - \delta\omega \approx \frac{19}{20}$ be the completion fraction of the forward transition as $\theta : \theta_G \rightarrow \theta_G + \delta\theta_G$. Substituting $\tilde{\omega} = 1 - \delta\omega$ at $\theta = \theta_G + \delta\theta_G$ into (3.86) and solving for β_ω gives $\beta_\omega = -(1/\ln \delta\omega)[\Psi^{G,\theta}(\theta_G + \delta\theta_G) - \Psi^{M,\theta}(\theta_G + \delta\theta_G)]$. From symmetry, $\beta_\omega = -(1/\ln \delta\omega)[\Psi^{M,\theta}(\theta_G - \delta\theta_G) - \Psi^{G,\theta}(\theta_G - \delta\theta_G)]$ is derived for reverse transition to residual fraction $\delta\omega$ via $\theta : \theta_G \rightarrow \theta_G - \delta\theta_G$ in (3.87). Averaging the two defines β_ω used henceforth:

$$\beta_\omega = \frac{-1}{2\ln \delta\omega} \{ [\Psi^{G,\theta}(\theta_G + \delta\theta_G) - \Psi^{G,\theta}(\theta_G - \delta\theta_G)] - [\Psi^{M,\theta}(\theta_G + \delta\theta_G) - \Psi^{M,\theta}(\theta_G - \delta\theta_G)] \},$$

$$\delta\omega \approx \frac{1}{20}, \quad \delta\theta_G \approx 5 \text{ K}. \quad (3.90)$$

3.7 Shock decomposition

The present framework focuses on shock decomposition rather than thermal decomposition. Depending on heating rate and ambient environment (e.g., air or some other gas), thermal decomposition at ambient atmospheric pressure typically commences at temperatures on the order of several hundred K above θ_G [5, 96, 98]. The process is often modeled via Arrhenius kinetics, where time scales span seconds to minutes. Combustion can take place in the presence of oxygen, but thermal decomposition is possible without combustion. The temperature rise induces chemical changes as the polymer backbones and side groups somewhat gradually dissociate into constituent monomers at chain ends or internal scissions [5, 96, 97].

Shock decomposition, conversely, occurs over time scales of microseconds or less, and at much higher pressures and temperatures, for example tens of GPa and over 1000 K. It was originally thought to involve a solid-fluid [88] or solid-solid [85] phase transformation. An early model [93] linked observed changes in dielectric polarization and electric conductivity to polymer chain scission. More recent interpretations [86, 89–92, 95], supported by contemporary experimental evidence (e.g., recovered samples) and chemistry models, regard shock decomposition as an extremely rapid disintegration of the condensed glass or melt phase (i.e., the reactants) into various gases and remnant solid particles such as carbon (i.e., the products). See also Ref. [158]. Hugoniot data show a reduction in specific volume upon shock decomposition that may be small to large depending on the particular polymer [85, 86]. Therefore, compressive pressure necessarily contributes toward the driving force for shock decomposition. However, since decomposition does

not occur during isothermal hydrostatic compression to extreme pressures [94, 159], thermal energy or some other localized energetic source in the shock front [93], in addition to mechanical pressure-volume work, must promote decomposition. Lower Hugoniot decomposition pressures for porous polymers relative to their dense counterparts [86], in addition to higher temperatures reached in porous materials at the same pressure, support this assertion. Experimental measurements [90, 158] and various model predictions [91] are conflicting with regard to temperature rise and dissipated energy during shock decomposition. Some details of the process, for example the extent of densification, correlate qualitatively with chain structure and degree of crystallinity [86].

Previous continuum models for shock decomposition appear limited to piecewise equations-of-state relating pressure, volume, free or internal energy, and temperature [86, 90, 91, 95] below and above the decomposition threshold. Such equations-of-state are typically constructed via a combination of theoretical assumptions (e.g., cold and thermal contributions) and calibrated to various high-pressure datasets. Thermochemical modeling [86, 91, 92, 95] has been used to provide equations-of-state for decomposed products, whereby fractions of fluid and solid products are determined by minimizing Gibbs free energy of the product mixture. Potential chemical products are assigned based on physical assumptions, but no calibration to experiments is needed. Ab-initio molecular dynamics has been used to model the shock Hugoniot spanning decomposition [91]. Equations-of-state alone do not address kinetics. An Arrhenius model [92] has instilled a time scale for decomposition reaction progress in simulations of shock propagation.

Here, shock decomposition is treated as a first-order phase transition from solid and melt reactants to dissociated products. The kinetic model parallels that for melting given in Section 3.6. Decomposition is one-way (i.e., products do not recombine into a condensed material when pressure and temperature are reduced), so only forward transformations are modeled. Unlike the second-order glass transition, the first-order decomposition process incurs a volume change $\delta_{\Xi} \leq 0$, negative for irreversible volume collapse [85], affecting (3.3). Net dissipation \mathfrak{D}_{Ξ} and thermodynamic driving force for decomposition F_{Ξ} are defined as entering (2.22). From (3.7) with (3.9),

$$\begin{aligned} \mathfrak{D}^{\tilde{\Xi}} &= F_{\Xi} \dot{\Xi}; & F_{\Xi} &= -[J p^E \delta_{\Xi} / (1 - \Xi \delta_{\Xi})] - \partial_{\Xi} \Psi = p^E \Delta_{\Xi} + \Psi^{GM} - \Psi^D; \\ \Delta_{\Xi} &= -J \delta_{\Xi} / (1 - \Xi \delta_{\Xi}) \approx -\delta_{\Xi}, & \Psi^{GM} &= (1 - \omega) \Psi^G + \omega \Psi^M. \end{aligned} \quad (3.91)$$

The approximation in (3.91) is most valid for $|J - 1| \ll 1$ and $|\delta_{\Xi}| \ll 1$, and Ψ^{GM} is the combined free energy density of the intact solid-liquid mixture of glass and melt phases. Here, F_{Ξ} can be related to a Gibbs free energy difference between reactant and product phases, though it includes a dependence on Ξ through the transformation work term. Let $\tau_{\Xi} = \tau_{\Xi}(\theta) > 0$ be a characteristic relaxation time for decomposition that likely decreases with increasing θ [86, 92]. For the process to substantially manifest in a shock front [93], τ_{Ξ} should not exceed the order of tens of nanoseconds. Denote by R_{Ξ} a decomposition resistance function (when positive) having dimensions of energy density. The metastable decomposed fraction is $\tilde{\Xi}(\mathbf{X}, t) \in [0, 1]$. A kinetic law enforcing $\mathfrak{D}_{\Xi} \geq 0$ for forward ($\dot{\Xi} > 0$) transitions at (\mathbf{X}, t) is

$$\tau_{\Xi} \dot{\Xi} = \begin{cases} (\tilde{\Xi} - \Xi) H(F_{\Xi}), & [\text{if } \Xi < \tilde{\Xi} \text{ and } F_{\Xi} - R_{\Xi} \geq 0]; \\ 0, & [\text{otherwise}]. \end{cases} \quad (3.92)$$

The first condition in (3.92) describes products \rightarrow reactants, the second to static equilibrium.

For positive decomposition rates, $F_{\Xi} > \langle R_{\Xi} \rangle$. The local metastable value of Ξ stems from differential relationship $d\Xi = (1 - \Xi)d\mathbb{F}$ [84, 144, 152, 156, 157], where dimensionless forward transition driving force $\mathbb{F} = F_{\Xi}/\beta_{\Xi}$. The proportionality factor is $\beta_{\Xi} = \text{const} > 0$. Decomposition can start when driving force exceeds normalized resistance R_{Ξ}/β_{Ξ} . Integrating over the dissociation process $\Xi : 0 \rightarrow \tilde{\Xi}$ to the current value of driving force F_{Ξ} gives the metastable value $\tilde{\Xi}$:

$$F_{\Xi} - R_{\Xi} \geq 0 \quad \Rightarrow \quad \int_0^{\tilde{\Xi}} \frac{d\Xi}{1 - \Xi} = \int_{R_{\Xi}/\beta_{\Xi}}^{F_{\Xi}/\beta_{\Xi}} d\mathbb{F} \quad \Rightarrow \quad \tilde{\Xi} = 1 - \exp \left[-\frac{F_{\Xi} - R_{\Xi}}{\beta_{\Xi}} \right]. \quad (3.93)$$

Free energy difference $\Psi_0^{D,\theta}$ between reactants and decomposed products coexisting at the same temperature, latent heat energy for decomposition λ_{θ}^D , and transformation temperature θ_D , all constants in (3.38), must be assigned for specific polymers. To complete the kinetic model, relaxation time $\tau_{\Xi} > 0$, proportionality factor $\beta_{\Xi} > 0$, and resistance function $R_{\Xi}(\square)$ must also be specified.

Properties and functions are determined from shock compression data, most abundant for plane-wave loading providing the principal Hugoniot (e.g., shock stress versus specific volume and shock velocity versus particle velocity). Such data, which include shock pressure, volume, and possibly temperature, can be experimental [85, 158] or, if necessary, obtained from published results of alternative continuum or molecular theories [91]. The time scale τ_{Ξ} is assumed small enough that Hugoniot data depict metastable states, as in prior work on metallic phase transitions [144, 152, 157] and implied in equation-of-state modeling of polymers [86, 90, 91, 95]. A finite magnitude of volume reduction $|\delta_{\Xi}|$ enables identification of the transition shock pressure from shock velocity, and possibly shock pressure, data [85, 86].

Denote by $P^H = p^H + \frac{2}{3}\bar{\sigma}^H$ the longitudinal shock stress or “shock pressure”, p^H the mean compressive pressure, and $\bar{\sigma}^H = [\frac{3}{2}(\bar{\sigma} : \bar{\sigma})]^{1/2}$ the Von Mises equivalent deviatoric stress, all measured along the principal Hugoniot in steady conditions behind the shock where viscosity of Section 3.8 is negligible. Denote by $J^H = V^H/V_0$ and θ^H the corresponding volume ratio and Hugoniot temperature. Prior to decomposition onset, the principal Hugoniot can be uniquely parameterized by any of J^H , P^H , shock velocity, or particle velocity via the Rankine-Hugoniot equations with the constitutive model for the non-decomposed continuum [102, 142]. Let P_D^H , J_D^H , and $\theta_D = \theta_D^H$ be defined as the initiation shock pressure and temperature at the onset of decomposition as identified by the Hugoniot data. Define resistance function $R_{\Xi}(\square)$ so that $R_{\Xi} = 0$ at this particular Hugoniot state. At decomposition onset, $F_{\Xi} = 0$, and from (3.38), $\theta = \theta_D$ so latent heat does not affect $\Psi^D(J_D^H)$. Denoting $p^E = p_D^H$ in (3.91), the constant energy term then follows from $F_{\Xi} = 0$, using J^H to parameterize free energies:

$$\begin{aligned} \Psi_0^{D,\theta} = & -p_D^H J_D^H \delta_{\Xi} + \Psi^{GM}(J_D^H) - [\Psi_V^{D,E}(J_D^H) + \Psi_{\beta}^{D,E}(J_D^H)] \\ & + c_{00}^D [\theta_D \ln(\theta_D/\theta_0) - (\theta_D - \theta_0)] + \frac{1}{2} c_{\theta}^D (\theta_D - \theta_0)^2. \end{aligned} \quad (3.94)$$

Now consider thermodynamic states at temperatures different from θ_D . If $\lambda_{\theta}^D > 0$, then the latent heat contribution to F_{Ξ} increases linearly with temperature above θ_D and decreases linearly with θ below θ_D . This trend agrees with experiments [94, 159] that show no evidence of high-pressure decomposition in conductivity or pressure-volume response under isothermal (room temperature) compression. If function R_{Ξ} is prescribed as independent of θ , then λ_{θ}^D can be chosen as

having a minimum positive value that prevents “cold” decomposition at $\theta = \theta_0$ as e_V^E is decreased and p^E increased above a large isothermal pressure, for example $p^E \gtrsim 100$ GPa in PMMA [94]. Alternatively, λ_θ^D can be set to zero and $R_\Xi = R_\Xi(\theta)$ defined to increase with decreasing $\theta < \theta_D$ to similarly preclude low-temperature decomposition. The latter approach is taken in Section 4.1.

Constant β_Ξ can be calibrated to Hugoniot P^H versus J^H data, if of sufficient fidelity, in the transition region from P_D^H to a (slightly) higher pressure state $P_\delta^H > P_D^H$ where transition appears complete. Upon full transformation volume collapse, a change in bulk compressibility is often perceptible in shock stress and velocity data [85]. Let $1 - \delta\Xi \approx \frac{19}{20}$ be the decomposition fraction as $P^H : P_D^H \rightarrow P_\delta^H$. Setting $\tilde{\Xi} = 1 - \delta\Xi$ at $P^H = P_\delta^H$ in (3.93), β_Ξ is obtained:

$$\beta_\Xi = (-1/\ln \delta\Xi)[p^H(P_\delta^H)\Delta_\Xi(P_\delta^H) + \Psi^{GM}(P_\delta^H) - \Psi^D(P_\delta^H) - R_\Xi(P_\delta^H)]. \quad (3.95)$$

In (3.95), shock stress P^H is more convenient than volume J^H for parameterizing Hugoniot energy states. Quantities on the right that depend implicitly on Ξ are evaluated at $\Xi(P_\delta^H) = 1 - \delta\Xi$. Note that $\beta_\Xi \rightarrow 0$ as $P_\delta^H \rightarrow P_D^H$, corresponding to coincident metastable and fully equilibrated states and a flat plateau on the P^H versus J^H Hugoniot. Volume collapse on this plateau is decrement $(J_\delta^H - 1)/J_\delta^H = \delta\Xi$, independent of J_D^H and β_Ξ . If data warrant, and depending on λ_θ^D prescribed, R_Ξ can be any function of state such as (volume, temperature) with constraints $R_\Xi(J_D^H, \theta_D) = 0$.

3.8 Heat conduction and viscosity

Isotropic heat flux in the spatial configuration, $\mathbf{q} = -k_\theta \nabla \theta$, is prescribed akin to Fourier’s law in the first of (2.25). The effective thermal conductivity k_θ depends on temperature, phase fractions, and damage. Temperature and phase dependencies follow functional forms in Refs. [2, 27], noting different trends persist in the glassy and melt regimes; see also Ref. [3]. Degradation from fracture follows Refs. [75, 84, 127], where a scalar parameter $\alpha_k^\xi \in [0, 1]$ denotes the ratio of conductivity in the fully degraded state to that of the undamaged state. The decomposed phase is simply assumed to have a constant conductivity k_θ^D . Therefore, with a_k^G, a_k^M, b_k^M material parameters and $k_\theta^G \geq 0$ and $k_\theta^M \geq 0$ conductivities of respective glass and melt phases at $\theta = \theta_G$,

$$k_\theta(\theta, \xi, \omega, \Xi) = (1 - \Xi)[1 + (\alpha_k^\xi - 1)\xi^2]\{(1 - \omega)k_\theta^G \left(\frac{\theta}{\theta_G}\right)^{a_k^G} + \omega k_\theta^M \langle a_k^M - b_k^M \frac{\theta}{\theta_G} \rangle\} + \Xi k_\theta^D. \quad (3.96)$$

Viscous stress $\boldsymbol{\tau}^V = J\boldsymbol{\sigma}^V$ of (2.25) for isotropic polymers depends on total deformation rate \mathbf{d} , shear viscosity μ_V , and bulk viscosity κ_V . These viscosities are distinguished from nonlinear effective viscosities from shear and bulk viscoelastic response in Section 3.3, respectively, $\mu_r^S \tau_m^S(\theta)$ and $\mu_r^V \tau_l^V(\theta)$ for each shear relaxation mode m and bulk relaxation mode l . The latter viscoelastic viscosities tend to zero at highly elevated temperatures since relaxation times τ_m^S and τ_l^V become negligible as shift functions a_T^S and a_T^V become vanishingly small in (3.39).

Here, μ_V accounts for high-temperature Newtonian viscosity in the melt, liquid, and decomposed states, as viscoelastic stiffening effects become negligible:

$$\mu_V(\theta, \omega, \Xi, \dot{\varepsilon}) = \mu_V^D(\dot{\varepsilon})\Xi + \mu_V^M(\dot{\varepsilon})\omega[\min\{1, \langle\theta - \theta_G\rangle/(\theta_M - \theta_G)\}]. \quad (3.97)$$

Rate dependent viscosities of decomposed (mostly gaseous) and liquid melt states are $\mu_V^D \geq 0$ and $\mu_V^M \geq 0$. Liquification temperature θ_M , where elastic shear modulus vanishes, is defined in (3.28).

Bulk viscosity κ_V is included here only for numerical reasons, in the setting of discretized modeling of shock waves. A standard technique [160, 161] is assignment of bulk viscous pressure p^V with terms linear and quadratic in compressive deformation rate to minimize spurious oscillations and spread shock fronts over multiple grid spacings l_G . Here, κ_V depends on \mathbf{d} , is zero for volumetric expansion, and is otherwise independent of material state for simplicity:

$$\kappa_V(\mathbf{d}) = \rho_0 l_G \{c_1^\kappa C_L^\kappa - c_2^\kappa l_G(\text{tr } \mathbf{d})\} \mathsf{H}(-\text{tr } \mathbf{d}) \geq 0. \quad (3.98)$$

Viscous pressure p^V is proportional to ρ and always non-negative. Standard constants for linear and quadratic bulk viscosity are $c_1^\kappa \geq 0$ and $c_2^\kappa \geq 0$. The effective longitudinal sound speed is a conservative upper bound taken as that of the glassy solid with instantaneous viscoelastic response:

$$C_L^\kappa = \{[\hat{B}_{\eta 0}^{G,E} + \frac{4}{3} \hat{G}_0^{G,E}]/\rho_0\}^{1/2}, \quad \hat{B}_{\eta 0}^{G,E} = \hat{B}_0^{G,E} + (\hat{\Gamma}_0^{G,E})^2 c_{V0}^G \theta. \quad (3.99)$$

The instantaneous isentropic bulk modulus $\hat{B}_{0\eta}^{G,E}$ is related to the isothermal bulk modulus $\hat{B}_0^{G,E}$ via the usual identity [38]. Both l_G and C_L^κ are taken as fixed Lagrangian quantities for consistency. Notation $\hat{\square}$ denotes thermoelastic properties in the limits $t/\tau_l^V \rightarrow 0$ and $t/\tau_m^S \rightarrow 0$ for all l, m .

Fourier conduction, Newtonian shear viscosity, and bulk shock viscosity are necessarily excluded when modeling shocks as singular surfaces [106, 162]. Otherwise, dissipation across the shock front would become infinite due to jump discontinuities in strain and temperature (i.e., effectively infinite strain rate and temperature gradient in the zero-width shock front).

3.9 Total stress and temperature rate

Total Cauchy stress $\boldsymbol{\sigma} = \boldsymbol{\sigma}^E + \boldsymbol{\sigma}^V$ in (2.15) comprises summed contributions from elasticity and viscoelasticity in $\boldsymbol{\sigma}^E$ and bulk and shear viscosity in $\boldsymbol{\sigma}^V$. The former are weighted by phase volume fractions (ω, Ξ) and damage degradation functions (f_V^E, f_S^E) via (3.9) with (3.10), (3.11), (3.12), and (3.13). Recall notation $\bar{\boldsymbol{\sigma}}^*$ and $-p^* \mathbf{1}$ for deviatoric and pressure contributions to stress quantity $\boldsymbol{\sigma}^*$. Total Cauchy stress is the weighted sum of cold pressures $p_V^{G,E}, p_V^{M,E}, p_V^{D,E}$ in (3.15), (3.17), (3.19); elastic shear and pressure-shear coupling stresses $\bar{\boldsymbol{\sigma}}_S^{G,E}, p_S^{G,E}, \bar{\boldsymbol{\sigma}}_S^{M,E}, p_S^{M,E}$ in (3.21), (3.22), (3.24), (3.25); thermoelastic coupling pressures $p_\beta^{G,E}, p_\beta^{M,E}, p_\beta^{D,E}$ in (3.30), (3.32), (3.34); viscoelastic shear and pressure-shear coupling stresses $\bar{\boldsymbol{\sigma}}_S^Y, p_S^Y$ in (3.43); viscoelastic bulk pressure p_V^Y in (3.50); viscous shear stress $\bar{\boldsymbol{\sigma}}^V$ with coefficient μ_V in (2.25), (3.97); and viscous bulk pressure p^V with coefficient κ_V in (2.25), (3.98):

$$\begin{aligned} \boldsymbol{\sigma} = & (1 - \Xi)(1 - \omega)[f_S^E(\bar{\boldsymbol{\sigma}}_S^{G,E} - p_S^{G,E} \mathbf{1}) - f_V^E(p_V^{G,E} + p_\beta^{G,E}) \mathbf{1}] \\ & + (1 - \Xi)\omega[f_S^E(\bar{\boldsymbol{\sigma}}_S^{M,E} - p_S^{M,E} \mathbf{1}) - f_V^E(p_V^{M,E} + p_\beta^{M,E}) \mathbf{1}] \\ & + (1 - \Xi)[f_S^E(\bar{\boldsymbol{\sigma}}_S^Y - p_S^Y \mathbf{1}) - f_V^E p_V^Y \mathbf{1}] - \Xi(p_V^{D,E} + p_\beta^{D,E}) \mathbf{1} + J^{-1}[(\kappa_V \text{tr } \mathbf{d}) \mathbf{1} + 2\mu_V \bar{\mathbf{d}}]. \end{aligned} \quad (3.100)$$

To evaluate the temperature rate, total internal dissipation \mathfrak{D} of (2.22) and other terms in (2.27) are needed. Internal dissipation comprises phase-field fracture kinetics $\mathfrak{D}^\xi \geq 0$ in (2.36); shear and

bulk viscoelasticity $\mathfrak{D}_S^r \geq 0$, $\mathfrak{D}_V^r \geq 0$ in (3.45), (3.52); shear yielding $\mathfrak{D}_A^P \geq 0$ in (3.62); internal state and free volume \mathfrak{D}^ς , \mathfrak{D}^φ in (3.70), (3.71); porosity $\mathfrak{D}^\phi \geq 0$ in (3.83); melting $\mathfrak{D}^\omega \geq 0$ in (3.84); and shock decomposition $\mathfrak{D}^\Xi \geq 0$ in (3.91). With Ψ_ς^P yet unspecified, assume $\mathfrak{D}^\varsigma + \mathfrak{D}^\varphi \rightarrow 0$, implying counteracting contributions to stored energy from ς (e.g., isotropic hardening) and ϕ (e.g., softening from excess free volume). Then internal dissipation is always non-negative:

$$\mathfrak{D} = \mathfrak{D}^\xi + \mathfrak{D}_S^r + \mathfrak{D}_V^r + \mathfrak{D}_A^P + \mathfrak{D}^\varsigma + \mathfrak{D}^\varphi + \mathfrak{D}^\phi + \mathfrak{D}^\omega + \mathfrak{D}^\Xi \geq 0. \quad (3.101)$$

As entering (2.36), the conjugate force to fracture is evaluated using (3.9)–(3.13) as

$$\begin{aligned} \zeta = -\partial_\xi \Psi = & 2(1-\Xi)(1-\omega)[(1-\xi H(e_V^E))(\Psi_V^{G,E} + \Psi_\beta^{G,E} + \Psi_V^{G,r}) \\ & + (1-\xi)(\Psi_S^{G,E} + \Psi_S^r + \Psi_A^{G,P} + \Psi_\varsigma^P)] \\ & + 2(1-\Xi)\omega[(1-\xi H(e_V^E))(\Psi_V^{M,E} + \Psi_\beta^{M,E} + \Psi_V^{M,r}) \\ & + (1-\xi)(\Psi_S^{M,E} + \Psi_S^r + \Psi_A^{M,P} + \Psi_\varsigma^M)]. \end{aligned} \quad (3.102)$$

The total specific heat per unit reference volume at constant strain $c = c_V(\theta, \omega, \Xi)$ combines contributions to Ψ that are nonlinear in θ and, in the approximation that transient nonlinear contributions from viscoelastic configurational free energies are negligible [4], are isolated to (3.36), (3.37), and (3.38):

$$\begin{aligned} c = -\theta \partial_{\theta\theta}^2 \Psi = & -\theta(1-\Xi)[(1-\omega)\partial_{\theta\theta}^2(\Psi^{G,\theta} + \Psi_V^{G,r} + \Psi_S^{G,r}) \\ & + \omega\partial_{\theta\theta}^2(\Psi^{M,\theta} + \Psi_V^{M,r} + \Psi_S^{M,r})] - \theta\Xi\partial_{\theta\theta}^2\Psi^{D,\theta} \\ \approx & (1-\Xi)(1-\omega)[c_{V0}^G + c_\theta^G(\theta - \theta_0)] + (1-\Xi)\omega[c_{V0}^M + c_\theta^M(\theta - \theta_0)] + \Xi[c_{V0}^D + c_\theta^D(\theta - \theta_0)]. \end{aligned} \quad (3.103)$$

The total Grüneisen tensor $\boldsymbol{\Gamma}$ is a weighted sum of thermoelastic coupling terms $\boldsymbol{\Gamma}^{G,E}$, $\boldsymbol{\Gamma}^{M,E}$ in (3.35) and viscoelastic contributions from temperature dependence of Ψ_S^r , Ψ_V^r in (3.40), (3.47):

$$\begin{aligned} \boldsymbol{\Gamma} = & -\frac{1}{c} \frac{\partial^2 \Psi}{\partial \theta \partial \mathbf{e}^E} = (1-\Xi) \left[\frac{c_V^G}{c} (1-\omega) \boldsymbol{\Gamma}^{G,E} + \frac{c_V^M}{c} \omega \boldsymbol{\Gamma}^{M,E} - \frac{1}{c} \frac{\partial^2(\Psi_S^r + \partial \Psi_V^r)}{\partial \theta \partial \mathbf{e}^E} \right] + \frac{c_V^D}{c} \Xi \boldsymbol{\Gamma}^{D,E} \\ \approx & (1-\Xi) \left[\frac{c_V^G}{c} (1-\omega) \boldsymbol{\Gamma}^G + \frac{c_V^M}{c} \omega \boldsymbol{\Gamma}^M \right] + \frac{c_V^D}{c} \Xi \boldsymbol{\Gamma}^D; \end{aligned} \quad (3.104)$$

$$\begin{aligned} \boldsymbol{\Gamma}^G = & \frac{c_{V0}^G}{c_V^G} \left\{ f_V^E [\Gamma_0^{G,E} + \Gamma_1^{G,E} e_V^E + \frac{1}{2} \Gamma_2^{G,E} (e_V^E)^2] \mathbf{1} - 2f_S^E \frac{G_\theta^{G,E}}{c_{V0}^G} \bar{\mathbf{e}}^E \right. \\ & \left. - \frac{f_V^E}{c_{V0}^G} \sum_{l=1}^{\hat{l}} \frac{\partial^2 \hat{\Psi}_l^{G,V}}{\partial \theta \partial \mathbf{e}^E} - \frac{f_S^E}{c_{V0}^G} \sum_{m=1}^{\hat{m}} \frac{\partial^2 \hat{\Psi}_m^{G,S}}{\partial \theta \partial \mathbf{e}^E} \right\}, \end{aligned} \quad (3.105)$$

$$\begin{aligned} \boldsymbol{\Gamma}^M = & \frac{c_{V0}^M}{c_V^M} \left\{ f_V^E [\Gamma_0^{M,E} + \Gamma_1^{M,E} e_V^E + \frac{1}{2} \Gamma_2^{M,E} (e_V^E)^2] \mathbf{1} - 2f_S^E \frac{M_\theta^{G,E}}{c_{V0}^G} \bar{\mathbf{e}}^E \right. \\ & \left. - \frac{f_V^E}{c_{V0}^M} \sum_{l=1}^{\hat{l}} \frac{\partial^2 \hat{\Psi}_l^{M,V}}{\partial \theta \partial \mathbf{e}^E} - \frac{f_S^E}{c_{V0}^M} \sum_{m=1}^{\hat{m}} \frac{\partial^2 \hat{\Psi}_m^{M,S}}{\partial \theta \partial \mathbf{e}^E} \right\}, \end{aligned} \quad (3.106)$$

$$\boldsymbol{\Gamma}^D = \frac{c_{V0}^D}{c_V^D} [\Gamma_0^{D,E} + \Gamma_1^{D,E} e_V^E + \frac{1}{2} \Gamma_2^{D,E} (e_V^E)^2] \mathbf{1}. \quad (3.107)$$

In the approximation in (3.104), $\boldsymbol{\Gamma}^G$ and $\boldsymbol{\Gamma}^M$ comprise sums of relaxed elastic and instantaneous volume ($l \leq \hat{l}$) and shear ($m \leq \hat{m}$) modes active for the dynamic regime [4, 106]. Choices of \hat{m} and \hat{l} pertain to ratios that obey $\tau_l^V/t_R \gg 1$ and $\tau_m^S/t_R \gg 1$, where t_R is the time scale of the problem.

More derivatives with respect to temperature are needed to evaluate the third and fourth terms on the right side of (2.27). First derivatives, with viscoelastic approximations akin to (3.104), are

$$\partial_\theta \Psi^G = f_V^E (\partial_\theta \Psi_\beta^{G,E} + \partial_\theta \Psi_V^{G,Y}) + f_S^E (\partial_\theta \Psi_S^{G,E} + \partial_\theta \Psi_S^{G,Y} + \partial_\theta \Psi_A^{G,P}) + \partial_\theta \Psi^{G,\theta}; \quad (3.108)$$

$$\partial_\theta \Psi_\beta^{G,E} = -c_{V0}^G e_V^E [\Gamma_0^{G,E} + \frac{1}{2!} \Gamma_1^{G,E} e_V^E + \frac{1}{3!} \Gamma_2^{G,E} (e_V^E)^2], \quad \partial_\theta \Psi_S^{G,E} = G_\theta^{G,E} \bar{\mathbf{e}}^E : \bar{\mathbf{e}}^E, \quad (3.109)$$

$$\partial_\theta \Psi^{G,\theta} = -c_{00}^G \ln \frac{\theta}{\theta_0} - c_\theta^G (\theta - \theta_0), \quad (3.110)$$

$$\partial_\theta \Psi_A^{G,P} = \left[\frac{d \ln \mu_A^G}{d \theta} + \frac{d \ln N^{G,P}}{d \theta} \right] \Psi_A^{G,P}, \quad \frac{d \mu_A^G}{d \theta} = -\mu_{A\theta} \mathsf{H}(\mu_A^G), \quad \frac{d N^{G,P}}{d \theta} = N_\theta^P \mathsf{H}(N^{G,P}); \quad (3.111)$$

$$\partial_\theta \Psi^M = f_V^E (\partial_\theta \Psi_\beta^{M,E} + \partial_\theta \Psi_V^{M,Y}) + f_S^E (\partial_\theta \Psi_S^{M,E} + \partial_\theta \Psi_S^{M,Y} + \partial_\theta \Psi_A^{M,P}) + \partial_\theta \Psi^{M,\theta}; \quad (3.112)$$

$$\partial_\theta \Psi_\beta^{M,E} = -c_{V0}^M e_V^E [\Gamma_0^{M,E} + \frac{1}{2!} \Gamma_1^{M,E} e_V^E + \frac{1}{3!} \Gamma_2^{G,M} (e_V^E)^2], \quad \partial_\theta \Psi_S^{G,M} = G_\theta^{G,M} \bar{\mathbf{e}}^E : \bar{\mathbf{e}}^E, \quad (3.113)$$

$$\partial_\theta \Psi^{M,\theta} = -c_{00}^M \ln \frac{\theta}{\theta_0} - c_\theta^M (\theta - \theta_0), \quad (3.114)$$

$$\partial_\theta \Psi_A^{M,P} = \frac{d \ln \mu_A^M}{d \theta} \Psi_A^{M,P}, \quad \frac{d \mu_A^M}{d \theta} = \frac{1}{\theta_G} \langle \mu_{A0} - \mu_{A\theta} (\theta_G - \theta_0) \rangle; \quad (3.115)$$

$$\partial_\theta \Psi_V^Y = \partial_\theta \Psi_V^{G,Y} = \partial_\theta \Psi_V^{M,Y} \approx (1 - \omega) \sum_{l=1}^{\hat{l}} \partial_\theta \hat{\Psi}_l^{G,V} + \omega \sum_{l=1}^{\hat{l}} \partial_\theta \hat{\Psi}_l^{M,V}, \quad (3.116)$$

$$\partial_\theta \Psi_S^Y = \partial_\theta \Psi_S^{G,Y} = \partial_\theta \Psi_S^{M,Y} \approx (1 - \omega) \sum_{m=1}^{\hat{m}} \partial_\theta \hat{\Psi}_m^{G,S} + \omega \sum_{m=1}^{\hat{m}} \partial_\theta \hat{\Psi}_m^{M,S}; \quad (3.117)$$

$$\partial_\theta \Psi^D = \partial_\theta \Psi_\beta^{D,E} + \partial_\theta \Psi^{D,\theta}; \quad (3.118)$$

$$\partial_\theta \Psi_\beta^{D,E} = -c_{V0}^D e_V^E [\Gamma_0^{D,E} + \frac{1}{2!} \Gamma_1^{D,E} e_V^E + \frac{1}{3!} \Gamma_2^{D,M} (e_V^E)^2], \quad (3.119)$$

$$\partial_\theta \Psi^{D,\theta} = -c_{00}^D \ln \frac{\theta}{\theta_0} - c_\theta^D (\theta - \theta_0) - \frac{\lambda_\theta^D}{\theta_D}. \quad (3.120)$$

Internal energy per unit reference volume U and requisite entropy η can thus be written as a function of elastic strain, internal state, fracture order parameter, and temperature:

$$U(\mathbf{e}^E, \theta, \{\boldsymbol{\alpha}\}, \xi) = \Psi(\mathbf{e}^E, \theta, \{\boldsymbol{\alpha}\}, \xi) - \theta \partial_\theta \Psi(\mathbf{e}^E, \theta, \{\boldsymbol{\alpha}\}, \xi); \quad (3.121)$$

$$\eta = -\partial_\theta \Psi = -(1 - \Xi) [(1 - \omega) \partial_\theta \Psi^G + \omega \partial_\theta \Psi^M] + \Xi \partial_\theta \Psi^D. \quad (3.122)$$

The third term on the right of (2.27) contains contributions from rates of $(\omega, \Xi, \mathbf{A}, \{\mathbf{Y}_V\}, \{\mathbf{Y}_S\})$:

$$-(\partial_\theta \pi_\omega) \theta \dot{\omega} = (\partial_\omega^2 \Psi) \theta \dot{\omega} = (1 - \Xi) (\partial_\theta \Psi^M - \partial_\theta \Psi^G) \theta \dot{\omega}, \quad (3.123)$$

$$-(\partial_\theta \boldsymbol{\pi}_\Xi) \theta \dot{\Xi} = (\partial_\Xi^2 \Psi) \theta \dot{\Xi} = \{\partial_\theta \Psi^D - [(1-\omega) \partial_\theta \Psi^G + \omega \partial_\theta \Psi^M]\} \theta \dot{\Xi}, \quad (3.124)$$

$$\begin{aligned} & -(\theta \partial_\theta \boldsymbol{\pi}_A) : \dot{\mathbf{A}} = (\theta \partial_{A\theta}^2 \Psi) : \dot{\mathbf{A}} = \theta \partial_\theta \bar{\mathbf{M}}^A : \dot{\bar{\boldsymbol{\epsilon}}}^P \\ & \approx \frac{(1-\Xi) f_S^E \theta}{3N_0^P} \left[(1-\omega) \left(\frac{d \ln \mu_A^G}{d\theta} + \frac{d \ln N^{G,P}}{d\theta} \right) \mu_A^G N^{G,P} + \omega \frac{d \ln \mu_A^M}{d\theta} \mu_A^M N^{M,P} \right] \left[\frac{3 - (\lambda_N^P)^2}{1 - (\lambda_N^P)^2} \right] \bar{\mathbf{A}} : \dot{\bar{\boldsymbol{\epsilon}}}^P, \end{aligned} \quad (3.125)$$

$$-\theta \sum_l \partial_\theta \boldsymbol{\pi}_l^V : \dot{\mathbf{Y}}_l^V = \theta \sum_l \partial_{\mathbf{Y}_l^V \theta}^2 \Psi : \dot{\mathbf{Y}}_l^V = -(1-\Xi) f_V^E \theta \sum_l \frac{\boldsymbol{\mathcal{Q}}_l^V : \partial_\theta \boldsymbol{\mathcal{Q}}_l^V}{\tau_l^V \mu_l^V}, \quad (3.126)$$

$$-\theta \sum_m \partial_\theta \boldsymbol{\pi}_m^S : \dot{\mathbf{Y}}_m^S = \theta \sum_m \partial_{\mathbf{Y}_m^S \theta}^2 \Psi : \dot{\mathbf{Y}}_m^S = -(1-\Xi) f_S^E \theta \sum_m \frac{\boldsymbol{\mathcal{Q}}_m^S : \partial_\theta \boldsymbol{\mathcal{Q}}_m^S}{\tau_m^S \mu_m^S}. \quad (3.127)$$

If approximations (3.104), (3.116), and (3.117) are used, contributions from (3.126) and (3.127) to (2.27) are negligible. In that case, viscoelastic dissipation vanishes: $\{\dot{\mathbf{Y}}_l^V\} \rightarrow \{\mathbf{0}\} \Rightarrow \mathfrak{D}_V^r \rightarrow 0$ and $\{\dot{\mathbf{Y}}_m^S\} \rightarrow \{\mathbf{0}\} \Rightarrow \mathfrak{D}_S^r \rightarrow 0$. The fourth term on the right of (2.27) is, with $\dot{\xi}$ from (2.34) and (2.36),

$$\begin{aligned} & -(\partial_\theta \zeta) \theta \dot{\xi} = (\partial_\xi \theta) \theta \dot{\xi} = -\{2(1-\Xi)(1-\omega)[(1-\xi) \mathcal{H}(e_V^E)] (\partial_\theta \Psi_\beta^{G,E} + \partial_\theta \Psi_V^{G,Y}) \\ & \quad + (1-\xi)(\partial_\theta \Psi_S^{G,E} + \partial_\theta \Psi_S^{G,Y} + \partial_\theta \Psi_A^{G,P})] \\ & \quad + 2(1-\Xi)\omega[(1-\xi) \mathcal{H}(e_V^E)] (\partial_\theta \Psi_\beta^{M,E} + \partial_\theta \Psi_V^{M,Y}) \\ & \quad + (1-\xi)(\partial_\theta \Psi_S^{M,E} + \partial_\theta \Psi_S^{M,Y} + \partial_\theta \Psi_A^{M,P})\} \theta \dot{\xi}. \end{aligned} \quad (3.128)$$

The spatial gradient of thermal conductivity $k_\theta = k_\theta(\theta, \xi, \omega, \Xi)$ in (3.96) is also needed:

$$\begin{aligned} \nabla k_\theta = & \left[(1-\Xi)[1 + (\alpha_k^\xi - 1)\xi^2] \{(1-\omega)k_\theta^G \frac{a_k^G}{\theta_G} \left(\frac{\theta}{\theta_G} \right)^{a_k^G-1} - \omega k_\theta^M \frac{b_k^M}{\theta_G} \mathcal{H} \left(a_k^M - b_k^M \frac{\theta}{\theta_G} \right) \} \right] \nabla \theta \\ & + \left[(1-\Xi)[2(\alpha_k^\xi - 1)\xi] \{(1-\omega)k_\theta^G \left(\frac{\theta}{\theta_G} \right)^{a_k^G} + \omega k_\theta^M \langle a_k^M - b_k^M \frac{\theta}{\theta_G} \rangle \} \right] \nabla \xi \\ & + \left[(1-\Xi)[1 + (\alpha_k^\xi - 1)\xi^2] \{k_\theta^M \langle a_k^M - b_k^M \frac{\theta}{\theta_G} \rangle - k_\theta^G \left(\frac{\theta}{\theta_G} \right)^{a_k^G} \} \right] \nabla \omega \\ & + \left[k_\theta^D - [1 + (\alpha_k^\xi - 1)\xi^2] \{(1-\omega)k_\theta^G \left(\frac{\theta}{\theta_G} \right)^{a_k^G} + \omega k_\theta^M \langle a_k^M - b_k^M \frac{\theta}{\theta_G} \rangle \} \right] \nabla \Xi. \end{aligned} \quad (3.129)$$

Finally, temperature rate in (2.27) is, with all terms defined above in Section 3.9, the following:

$$\begin{aligned} c \dot{\theta} = & \mathfrak{D} - c \theta \boldsymbol{\Gamma} : (\mathbf{d} - \mathbf{d}^P) + [\kappa_V (\text{tr} \mathbf{d})^2 + 2\mu_V \bar{\mathbf{d}} : \bar{\mathbf{d}}] + J[k_\theta \nabla^2 \theta + \nabla k_\theta \cdot \nabla \theta] + \rho_0 r \\ & - \theta \{(\partial_\theta \zeta) \dot{\xi} + (\partial_\theta \pi_\omega) \dot{\omega} + (\partial_\theta \pi_\Xi) \dot{\Xi} + (\partial_\theta \pi_A) : \dot{\mathbf{A}} + \sum_l \partial_\theta \boldsymbol{\pi}_l^V : \dot{\mathbf{Y}}_l^V + \sum_m \partial_\theta \boldsymbol{\pi}_m^S : \dot{\mathbf{Y}}_m^S\}. \end{aligned} \quad (3.130)$$

4 Application: PMMA

The constitutive framework of Section 3 is applied toward the uniaxial-strain shock response of the transparent amorphous polymer PMMA. Properties and parameters are given in Tables A.1 and A.2 of Appendix A with supporting references. Refined or additional parameters for the structured shock propagation analysis of Section 4.2 are given in Table A.3. Certain values are calculated or calibrated to data in what follows. Not all kinds of PMMA are identical, but properties of current relevance appear to vary only modestly among samples from different suppliers [163–165].

Relaxation times for viscoelasticity span many orders of magnitude (e.g., time constants from 10^{-7} s to 10^4 s in Ref. [4]), whereas usual shock experiments conclude by $10^{-5} – 10^{-4}$ s. Long-time relaxation modes are inconsequential. Therefore, thermoelastic properties in Table 1 applicable to the Hugoniot analysis in Section 4.1 correspond to equilibrium states (far) behind the shock front attained at these time scales; axial strain rates in the shock front span the order of 10^4 /s to 10^9 /s, depending on shock strength. Equilibrium shear and bulk moduli at Hugoniot states are significantly larger in magnitude than their quasi-static versions [2, 3] but may be modestly smaller than instantaneous values from very high-frequency ultrasonic measurements [21, 166, 167] or states within the initial elastic shock front [29, 51, 145]. Relaxation to *quasi-static* values is irrelevant and not addressed in Section 4. Viscoelastic stiffening above quasi-static properties is implicitly included in $\Psi_V^{G,E}$, $\Psi_\beta^{G,E}$, and $\Psi_S^{G,E}$ rather than $\Psi_V^{G,R}$ and $\Psi_S^{G,R}$. This simplifies the analysis of Section 4.1 while yielding the same sought results. Differently, modeled in Section 4.2 is viscoelastic relaxation from instantaneous response at the head of structured wave form to equilibrium Hugoniot response at its tail. Similar viscoelasticity assumptions are used in Refs. [20, 30, 31, 51, 117].

Consideration of the glass \rightarrow melt transition at null deformation produces offset energy $\Psi_0^{M,\theta}$ and kinetic parameter β_ω via (3.89) and (3.90) of Section 3.6. Forward and reverse second-order transitions occur over an approximate 10 K window centered at θ_G in Fig. A.1(a). The decrease in free energy and increase in specific heat from glass to melt are shown in Fig. A.1(b) and Fig. A.1(c). Prescription of R_ω for high-pressure states applicable to shock loading is addressed in Section 4.1. Ranges of static, ambient pressure transition temperatures spanning $373\text{ K} \leq \theta_G \leq 393\text{ K}$ have been reported for PMMA [2–4, 50, 79]; here the value of 378 K quoted in Ref. [20] is used.

4.1 Hugoniot response to high pressure

Shocks are analyzed in the infinitesimal width (i.e., singular surface) limit in Section 4.1, though the forthcoming Hugoniot jump equations also apply between any two states in a structured steady wave [102, 142]. Cartesian Lagrangian and Eulerian coordinates are (X_1, X_2, X_3) and (x_1, x_2, x_3) . A planar shock propagates at Lagrangian speed $\mathcal{U} > 0$ in the $X = X_1$ direction. Let \square^+ and \square^- label respective quantities at states immediately ahead of and trailing the shock front. Particle velocity is $v = v_1$. Shear and bulk shock viscosities are excluded following discussion in Section 3.8; the Rankine-Hugoniot equations directly incorporate shock dissipation without need for the latter. Therefore, $\boldsymbol{\sigma} = \boldsymbol{\sigma}^E$, $\bar{\boldsymbol{\sigma}} = \bar{\boldsymbol{\sigma}}^E$, and $p = p^E$. Recall $\bar{\boldsymbol{\sigma}} = [\frac{3}{2}\bar{\boldsymbol{\sigma}} : \bar{\boldsymbol{\sigma}}]^{1/2}$ is the Von Mises equivalent shear stress. The shock stress P is the longitudinal true stress, positive in compression and obeying

$$P = -\sigma_{11} = p - \bar{\sigma}_{11} = p + \frac{2}{3}\bar{\sigma}; \quad \bar{\sigma} = \sigma_{22} - \sigma_{11} = \sigma_{33} - \sigma_{11} = -\frac{3}{2}\bar{\sigma}_{11}. \quad (4.1)$$

Lateral stresses are $\sigma_{22} = \sigma_{33}$. Adiabatic conditions are assumed. Particle velocity, specific volume, mass density, stress, temperature, energy, and entropy are discontinuous across the front. The jump in any such quantity is $[\square] = \square^- - \square^+$. Rankine-Hugoniot jump relations are discrete analogs of the continuum balances of mass, linear momentum and energy in (2.4) and the entropy imbalance in (2.5). In Lagrangian form [102, 142] and recalling $u = U/\rho_0$,

$$\rho_0 \mathcal{U} [1/\rho] = -[\nu], \quad \rho_0 \mathcal{U} [\nu] = [P], \quad \rho_0 \mathcal{U} [u + \frac{1}{2}v^2] = [Pv], \quad \mathcal{U} [\eta] \geq 0. \quad (4.2)$$

No split-wave structure (e.g., precursor wave) emerges in shock wave studies on PMMA [7, 20]. Therefore, for analysis of the principal Hugoniot in Section 4.1, conditions ahead of the wave correspond to a resting state in the reference configuration, whereby according to the constitutive functions in Section 3 with the null (gauge) pressure state corresponding to atmospheric pressure,

$$v^+ = 0, \quad J^+ = 1, \quad \rho^+ = \rho_0, \quad \theta^+ = \theta_0, \quad P^+ = p^+ = 0, \quad U^+ = (\Psi - \theta \partial_\theta \Psi)^+ = U_0. \quad (4.3)$$

The \square^- superscripts for the shocked state are safely omitted in Section 4.1 without chance of confusion. The constitutive model furnishes equations for stress and free energy of the following form, where $J = J^- = J^H = \rho_0/\rho^H$ is the Hugoniot compression ratio:

$$P = P^H(J^H, \theta(J^H), \gamma^P(J^H), \{\alpha\}(J^H), \dots), \quad \Psi = \Psi^H(J^H, \theta(J^H), \gamma^P(J^H), \{\alpha\}(J^H), \dots). \quad (4.4)$$

Rankine-Hugoniot equations (4.2) reduce to the energy equation and expressions for particle and shock velocities for $J = J^H < 1$ ($\mathcal{U} \rightarrow C_L$, the isentropic sound speed akin to (3.99) as $J \rightarrow 1$):

$$U - U_0 = \frac{1}{2}P(1 - J), \quad v = [P(1 - J)/\rho_0]^{1/2}, \quad \mathcal{U} = v/(1 - J). \quad (4.5)$$

In the present analysis, (4.4) and the first of (4.5) are solved for P , Ψ , θ , and other material response functions using an iterative method as J is decremented from unity on the principal Hugoniot. In each decrement, v and \mathcal{U} are calculated a posteriori using the second and third of (4.5).

Principal stresses are all negative (i.e., compressive), so no crazing or porosity change occurs, meaning $\phi = 0$. Furthermore, following Refs. [4, 20], neither melting nor fracture occur under planar uniaxial compression from a start temperature of $\theta_0 = 295$ K. Although melting is promoted by temperature rise, and Hugoniot temperatures far exceed θ_G , the transition from glass to melt is strongly impeded by compressive pressure [1, 4, 155] and requires a finite time t_ω that may be longer than that witnessed in shock experiments. For example, the effective glass transition temperature of PMMA increases by 236 K per GPa of static pressure in Ref. [155]. Extrapolating, this is on the order of 5× faster than the rate of temperature increase on the principal Hugoniot [158, 168, 169]. Confining pressures modest relative to those in shock compression have been shown to suppress fracture of PMMA in quasi-static and dynamic loading, promoting shear yielding or shear banding instead [64, 65]. Kinetic resistance functions R_ω and R_ξ needed in the model to suppress melting and shear-induced fracture for Hugoniot states are calculated later.

Let $\bar{\mathbf{F}}^P$ denote plastic deformation from shear yielding and J^Ξ the volumetric deformation from shock decomposition. In matrix form, the uniaxial deformation gradient can be written

$$\mathbf{F} = \begin{bmatrix} J & 0 & 0 \\ 0 & 1 & 0 \\ 0 & 0 & 1 \end{bmatrix} = \mathbf{F}^E \bar{\mathbf{F}}^P (J^\Xi)^{1/3} = \begin{bmatrix} F_{11}^E & 0 & 0 \\ 0 & F_{22}^E & 0 \\ 0 & 0 & F_{22}^E \end{bmatrix} \begin{bmatrix} \bar{F}^P & 0 & 0 \\ 0 & \bar{F}^{P-1/2} & 0 \\ 0 & 0 & \bar{F}^{P-1/2} \end{bmatrix} \begin{bmatrix} F^\Xi & 0 & 0 \\ 0 & F^\Xi & 0 \\ 0 & 0 & F^\Xi \end{bmatrix}. \quad (4.6)$$

The following kinematic and stress relations then apply, where $F^{\Xi} = (J^{\Xi})^{1/3} = (1 - \Xi \delta_{\Xi})^{-1/3}$:

$$J = J^E J^{\Xi} = \frac{F_{11}^E (F_{22}^E)^2}{1 - \Xi \delta_{\Xi}}, \quad F_{11}^E = \frac{J}{\bar{F}^P F^{\Xi}}, \quad F_{22}^E = \frac{(\bar{F}^P)^{1/2}}{F^{\Xi}}, \quad e_V^E = \ln J^E = \ln J - \ln J^{\Xi}; \quad (4.7)$$

$$\bar{e}_{11}^E = -2\bar{e}_{22}^E = \ln F_{11}^E - \frac{1}{3}e_V^E, \quad \bar{\mathbf{e}}^E = \text{diag}(\bar{e}_{11}^E, \bar{e}_{22}^E, \bar{e}_{22}^E), \quad \gamma^P = -\sqrt{3} \ln \bar{F}^P, \quad \mathbf{A} = \bar{\mathbf{F}}^P (\bar{\mathbf{F}}^P)^T; \quad (4.8)$$

$$\lambda^P = \left\{ \frac{1}{3} [(\bar{F}^P)^2 + 2/\bar{F}^P] \right\}^{1/2}, \quad \bar{\mathbf{N}}^P = -\sqrt{\frac{2}{3}} \text{diag}(1, -\frac{1}{2}, -\frac{1}{2}), \quad \tau^A = \bar{\mathbf{M}}^A : \bar{\mathbf{N}}^P = -\frac{\sqrt{3}}{2} \bar{M}_{11}^A; \quad (4.9)$$

$$\bar{\mathbf{M}}^E = J \bar{\boldsymbol{\sigma}} = J \text{diag}(\bar{\sigma}_{11}, -\frac{1}{2} \bar{\sigma}_{11}, -\frac{1}{2} \bar{\sigma}_{11}), \quad \tau^E = \bar{\mathbf{M}}^E : \bar{\mathbf{N}}^P = -\frac{\sqrt{3}}{2} J \bar{\sigma}_{11} = \frac{\sqrt{3}}{3} J \bar{\sigma}. \quad (4.10)$$

Secant bulk and shear moduli, Hugoniot specific heat, and Hugoniot Grüneisen parameter are

$$B_H = (1 - \Xi) B_H^G + \Xi B_H^D = (1 - \Xi) B_0^{G,E} [1 - \frac{1}{2} B_1^{G,E} e_V^E + \frac{1}{6} B_2^{G,E} (e_V^E)^2 - \frac{1}{24} B_3^{G,E} (e_V^E)^3] + \Xi B_0^{D,E} [1 - \frac{1}{2} B_1^{D,E} e_V^E + \frac{1}{6} B_2^{D,E} (e_V^E)^2 - \frac{1}{24} B_3^{D,E} (e_V^E)^3], \quad (4.11)$$

$$G_H = G_0^{G,E} + G_{\theta}^{G,E} (\theta - \theta_0) - B_0^{G,E} (G_p^{G,E} - G_2^{G,E} e_V^E) e_V^E, \quad c_V(\theta, \Xi) = (1 - \Xi) c_V^G(\theta) + \Xi c_V^D(\theta), \quad (4.12)$$

$$\Gamma = \frac{1}{3} \text{tr} \boldsymbol{\Gamma} = (1 - \Xi) \frac{c_{V0}^G}{c_V} [\Gamma_0^{G,E} + \Gamma_1^{G,E} e_V^E + \frac{1}{2} \Gamma_2^{G,E} (e_V^E)^2] + \Xi \frac{c_{V0}^D}{c_V} [\Gamma_0^{D,E} + \Gamma_1^{D,E} e_V^E + \frac{1}{2} \Gamma_2^{D,E} (e_V^E)^2]. \quad (4.13)$$

Lagrangian longitudinal sound speed $C_L = C_E/J$ in the shocked state is useful for comparison to measured velocities of release or rarefaction waves, where C_E is Eulerian sound speed [142]:

$$\rho_0 (C_L)^2 = - \left[\frac{\partial P}{\partial J} \Big|_{\eta, \gamma^P, \{\boldsymbol{\alpha}\}} - \left[\frac{\partial P}{\partial J} \Big|_{\theta, \gamma^P, \{\boldsymbol{\alpha}\}} - \frac{\theta \Gamma}{J} \frac{\partial P}{\partial \theta} \Big|_{J, \gamma^P, \{\boldsymbol{\alpha}\}} \right] \right]. \quad (4.14)$$

Values of C_L are calculated analytically via differentiation of the thermoelastic functions in Section 3.2 such as in (4.11)–(4.13); $\partial \square / \partial J = (J^E / J) \partial \square / \partial J^E$ when other variables are held fixed.

In PMMA, plastic flow precedes shock decomposition as J decreases and P and θ increase on the Hugoniot. From Table A.1, decomposition begins at $J_D^H = 0.58$, $P_D^H = 25.7$ GPa, and $\theta_D = 1289$ K. From Table A.2, the Hugoniot elastic limit (HEL) for plastic flow occurs at $J_P^H = 0.937$, $P_P^H = 0.74$ GPa, and $\theta_P = 306$ K. For $J > J_P^H$, elastic conditions hold: $J = J^E$, $\bar{F}^P = 1$, $\gamma^P = \Xi = 0$. For $J \geq J_P^H$, plastic shear $\gamma^P = -\sqrt{3} \ln \bar{F}^P$ is determined by static equilibrium conditions for each Hugoniot state *behind* the shock front [144, 152, 157]. Inverting (3.68) and using (3.69),

$$\dot{\gamma}^P = 0 \quad \Rightarrow \quad \tau^F = 0 \quad \Rightarrow \quad \tau^E = \{ \tau^A + (1 - \Xi) \langle \tau^{\zeta} - \alpha_{\theta}^F (\theta - \theta_0) - \alpha_p^F B_0^{G,E} e_V^E \rangle \} f_R^P, \quad (4.15)$$

where $e_V^E \leq 0$. Conditions at the HEL $f_R^P (e_V^E = \ln J_P^H) = 1$ and $\tau^E (\ln J_P^H) = \tau_P^E$ provide the constant

$$\alpha_p^F = -[\tau_P^E - \tau_0^{\zeta} + \alpha_{\theta}^F (\theta_P - \theta_0)] / (B_0^{G,E} \ln J_P^H). \quad (4.16)$$

Function $f_R^P(e_V^E, \theta(e_V^E))$ is a polynomial calibrated to match complex pressure and temperature dependent strength of PMMA on the Hugoniot presented later. With constants f_i and e_C^P in Table A.2,

$$f_R^P = \langle 1 + \sum_{i=1}^6 f_i (e_V^P)^i \rangle \mathcal{H}(e_C^P - e_V^P), \quad e_V^P = \langle \ln J_P^H - e_V^E \rangle. \quad (4.17)$$

Kinetic equations for isotropic hardening and plastic free volume are given in rate form in (3.66) and (3.67). In those equations, values of $\tau^\varsigma(t)$ and $\varphi(t)$ depend on the local history of $\dot{\gamma}^P(t)$. However, in the Hugoniot analysis of singular surfaces, the time history of γ^P and its rate are unknown because transient flow processes in the shock front are unresolved. Therefore, substitute equations for φ , ς , and τ^ς that depend on γ^P rather than its rate are posited for Hugoniot states:

$$\varphi(\gamma^P) = [1 - \exp(-\gamma^P/a_\varphi)]\varphi_\infty, \quad (4.18)$$

$$\tau^\varsigma(\gamma^P, \varphi(\gamma^P)) - \tau_0^\varsigma = \mu_\varsigma^G \varsigma(\gamma^P, \varphi) = \mu_\varsigma^G \{1 - \exp(-\gamma^P/b_\varphi) - [1 - (\tau_\infty^\varsigma - \tau_0^\varsigma)/\mu_\varsigma^G]\varphi/\varphi_\infty\}. \quad (4.19)$$

Constants τ_0^ς , μ_ς^G , a_φ , and b_φ are listed in Table A.2. As shown in Fig. A.2, (4.18) and (4.19) give similar results for monotonic loading at room temperature to those for PMMA in Refs. [19, 26, 150]. Free volume φ increases smoothly to its terminal value φ_∞ with increasing γ^P . Isotropic stress τ^ς increases rapidly to an initial peak, then decays more gradually to its terminal value that only modestly exceeds its initial value τ_0^ς . Back stress from anisotropic hardening τ^A , in Fig. A.2(b) for reference, furnishes increasing shear strength at finite γ^P , as in Refs. [16, 19, 27, 150].

Metastable conditions for decomposition $\Xi = \tilde{\Xi}$ are assumed for Hugoniot states, similar to previous treatments of phase transformations in shock loading of metals [144, 152, 157]. For each decrement of $J = J^H$ on the principal Hugoniot, $\Xi(J^H)$ is obtained from (3.93). Threshold stress for decomposition onset P_D^H is assigned from experiments quoted in Table A.1, with J_D^H and θ_D corresponding calculated values at this shock pressure. Offset energy $\Psi_0^{D,\theta}$ and kinetic parameter β_Ξ are obtained from methods discussed in Section 3.7. Best agreement with experimental shock velocity and temperature data for shock pressures $P > P_D^H$ was achieved by setting thermodynamic latent heat $\lambda_\theta^D = 0$ and using a resistance function $R_\Xi(\theta)$ instead, where $\lambda_\theta^{\tilde{\Xi}}$ is a kinetic latent heat:

$$R_\Xi(\theta) = -\lambda_\theta^{\tilde{\Xi}}(\theta/\theta_D - 1). \quad (4.20)$$

The positive value of $\lambda_\theta^{\tilde{\Xi}}$ in Table A.1 prevents room-temperature, pressure-induced decomposition to hydrostatic pressures of nearly 800 GPa. Furthermore, $R_\Xi < 0$ for $\theta > \theta_D$, increasing the rate of decomposition versus P with increasing Hugoniot temperature. Dissipation from $\dot{\Xi}$ in (3.91) is unknown as kinetics inside the shock front are not resolved by the analysis, but results later confirm that total entropy production across every shock is positive in concurrence with the last of (4.2).

Potential melting can be considered by analogous assumptions on metastability of Hugoniot states. From (3.86), a minimum non-negative resistance function R_ω that prevents melting is determined by setting $F_\omega = R_\omega$ at each Hugoniot state $J = J^H$, where thermal and elastic Hugoniot properties of the melt are listed in Tables A.1 and A.2:

$$\begin{aligned} R_\omega(J^H) &\geq F_\omega(J^H) = (1 - \Xi) \langle \{\Psi^G(J^H) - \Psi^M(J^H)\} \rangle \\ &\approx (1 - \Xi) \langle \{\Psi_V^{G,E}(J^H) [1 - B_0^{M,E}/B_0^{G,E}] + \Psi_S^{G,E}(J^H) [1 - G_0^{M,E}/G_0^{G,E}] \\ &\quad + \Psi_\beta^{G,E}(J^H) [1 - c_{V0}^M/c_{V0}^G] + \Psi^{G,\theta}(\theta(J^H)) - \Psi^{M,\theta}(\theta(J^H)) + \Psi_A^{G,P}(J^H) - \Psi_A^{M,P}(J^H)\} \rangle. \end{aligned} \quad (4.21)$$

A similar approach provides the minimum threshold energy R_ξ needed to prevent fracture in metastable Hugoniot states far behind the wave front. Under shock compression, $\phi = 0$ and $e_V^E < 0$, so $F_\xi^E = (1 - \Xi)\Psi_S^{G,E}$, deviatoric elastic strain energy. With $\omega = 0$, (3.73) gives $R_\xi = (1 - \Xi)R_\xi^G$. The minimum non-negative fracture resistance is determined from setting $\Phi = 0$ in (3.75):

$$R_\xi(J_H) \geq (1 - \Xi)\langle\{\Psi_S^{G,E}(J^H) + c_\xi^P[\lambda^P(J^H) - 1]^2\}\rangle. \quad (4.22)$$

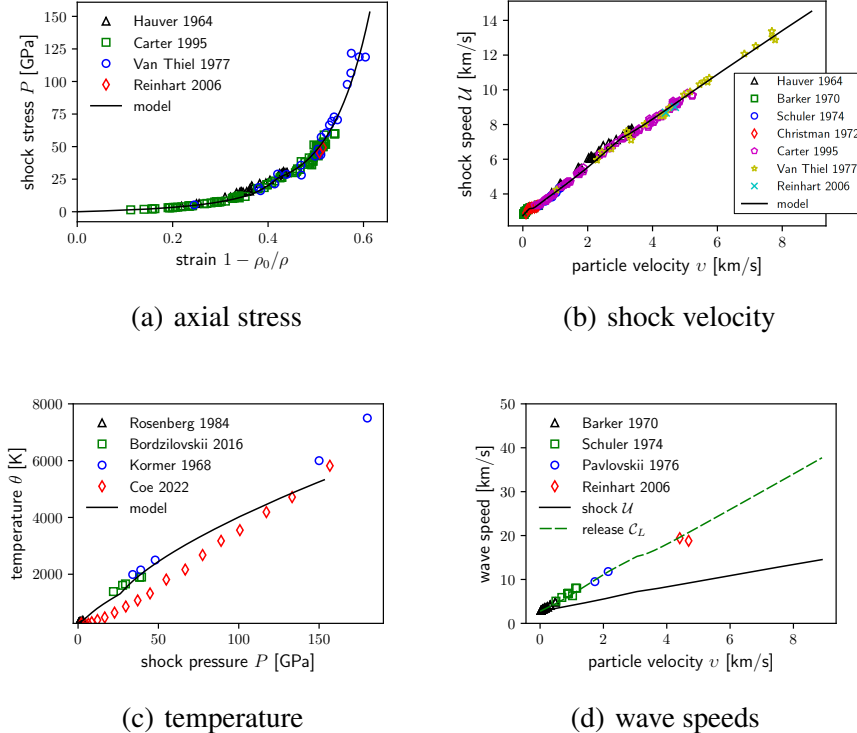


Figure 1. Hugoniot response of PMMA to extreme pressure: (a) shock stress or shock pressure P vs. strain from model and experiments [85, 87, 99, 170] (b) shock velocity U vs. particle velocity v from model and experiments [7, 51, 60, 85, 87, 99, 170] (c) temperature θ vs. stress from model, experiments [158, 168, 169], and DFT [91] (d) Lagrangian sound speed C_L from model and release experiments [7, 51, 170, 171]

The high-pressure Hugoniot response is compared to experimental data in Fig. 1. Experimental shock stress and shock velocity data [7, 51, 60, 85, 87, 99, 170] are matched well to shock stresses P evaluated to 120 GPa and shock speeds U evaluated to 13 km/s in respective Fig. 1(a) and Fig. 1(b). Experimental temperature data [158, 168, 169], which tend to exceed predictions from DFT [91], are well captured to pressures exceeding 50 GPa. Extrapolation to pressures over 150 GPa suggests the model under-predicts temperature in this regime versus historical data [158]. The assumed linear increase in specific heat with increasing temperature of the decomposed products is likely inaccurate at such high temperatures since $c_V^D(\theta)$ should plateau to an upper bound. Isentropic sound speed C_L is shown with shock velocity U in Fig. 1(d), along with release velocities from experiments [7, 51, 170, 171]. Agreement is respectable, and both wave speeds increase

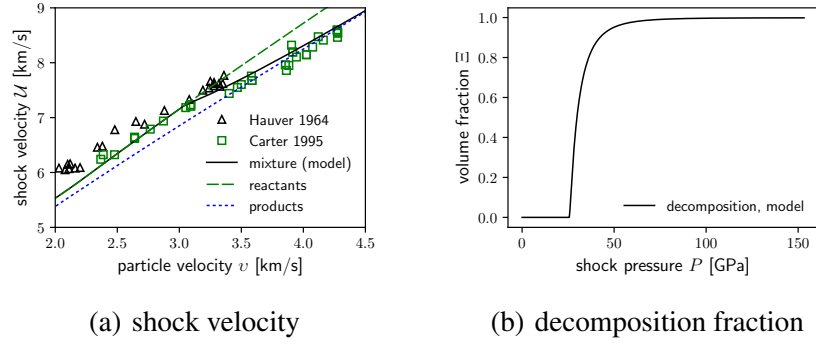


Figure 2. Hugoniot response of PMMA: (a) shock velocity \mathcal{U} vs. particle velocity v from model (mixture, reactants, and decomposed products) and relevant experiments [85, 87] in the vicinity of decomposition (b) predicted decomposition volume fraction Ξ vs. shock stress P

monotonically with increasing particle velocity. The continuous increase in \mathcal{U} precludes break-out of a precursor followed by a distinct plastic wave or transformation wave at the respective HEL or the shock decomposition threshold, for conditions that are not over-driven.

According to the model, shock decomposition commences at a pressure of 25.7 GPa and temperature of 1289 K, corresponding to a particle velocity of 3.0 km/s. The shock velocity-particle velocity Hugoniot is shown in this vicinity for the full model (mixture), isolated products, and isolated reactants in Fig. 2(a), along with experimental data [85, 87]. The predicted metastable decomposition fraction on the Hugoniot is reported in Fig. 2(b). The continuous decomposition process enables a smooth transition from the shock velocity Hugoniot of the reactants to the products, with a corresponding decrease in slope of \mathcal{U} versus v . Transformation is 60% complete at 31 GPa, 80% complete at 36 GPa, and 90% complete at 42 GPa where $\theta = 2124$ K.

The Hugoniot response at more modest pressures is featured in Fig. 3. Data of Refs. [7, 51] on shock stress and shock velocity are captured in Fig. 3(a) and Fig. 3(b). Near and just above the HEL at $P_P^H = 0.74$ GPa, at the onset of plastic flow, shock velocity increases very slowly with particle velocity in the $v = 200 - 260$ m/s range. Temperature closely follows experimental data [168] in Fig. 3(c). The model, in Fig. 3(d), reflects the complex strength behavior of PMMA as measured by lateral stress gauges in experiments [110, 111, 113, 114]. Pressure hardening to a peak strength of 1.54 GPa between P of 5 and 10 GPa is followed by a decrease in static strength to zero at $P \gtrsim 15$ GPa as enabled by the function (4.17). The decay is attributed to thermal softening from shock temperature rise in Ref. [114]; according to the model, $\theta = 920$ K at $P = 15$ GPa. Although equilibrium strength far behind the wave front vanishes for $P \gtrsim 15$ GPa, the material has neither melted nor fractured (i.e., $\omega = \xi = 0$); dynamic strength $\tau^F > 0$ for $\dot{\gamma}^P > 0$ persists in (3.68).

Effective secant bulk modulus, shear modulus, Grüneisen parameter, and specific heat on the Hugoniot, defined in (4.11)–(4.13) and all divided by their initial values, are reported in Fig. 4(a). The bulk modulus and specific heat increase with increasing compressive strain or pressure, with the exception of a momentary decrease in specific heat of the two-phase mixture of reactants and products during decomposition. The shear modulus increases with pressure to a peak at 30% compression, then decreases due to rapidly increasing shock temperature and later shock decomposi-

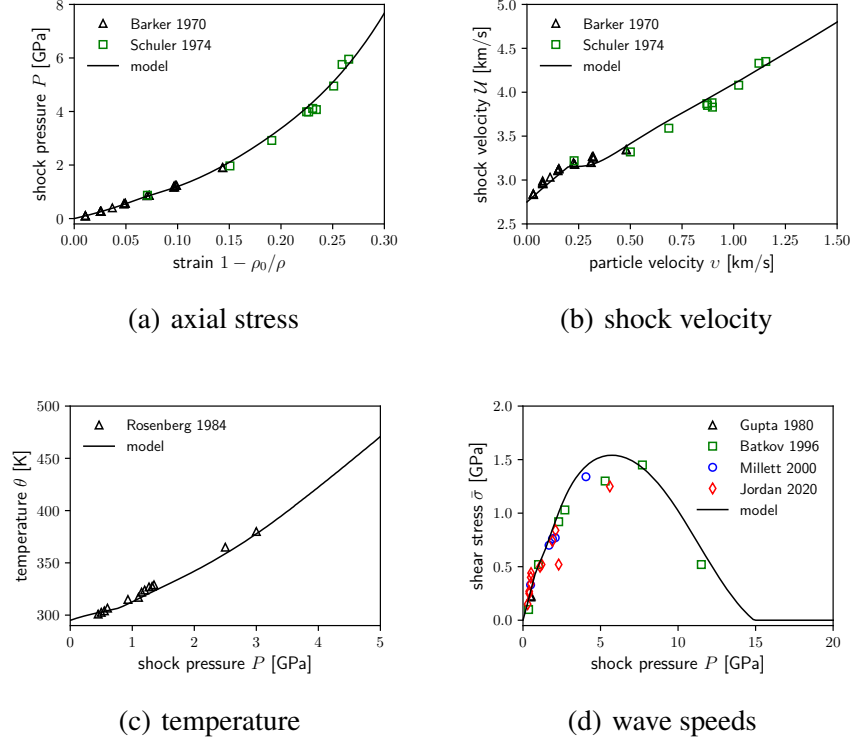


Figure 3. Hugoniot response of PMMA to moderate pressure: (a) shock stress or shock pressure P vs. strain from model and experiments [7, 51] (b) shock velocity U vs. particle velocity v from model and experiments [7, 51] (c) temperature θ vs. stress from model and experiments [168] (d) shear strength (Mises stress) $\bar{\sigma}$ from model and experiments [110, 111, 113, 114]

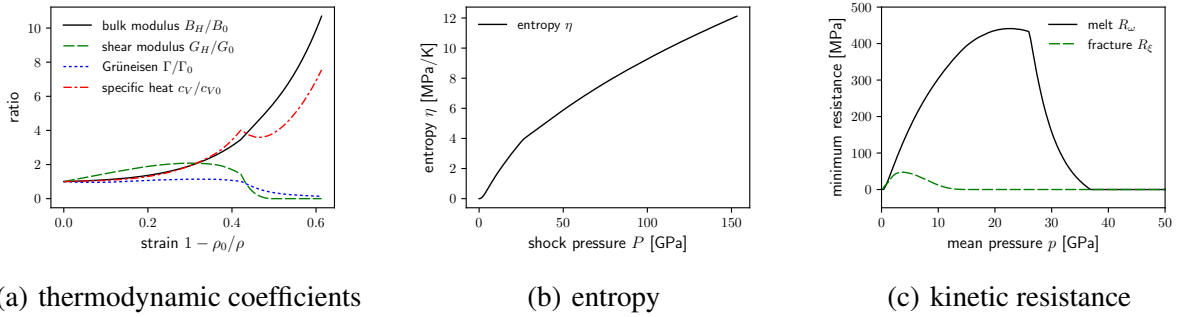


Figure 4. Predicted Hugoniot response of PMMA: (a) ratio of Hugoniot to initial bulk modulus, shear modulus, Grüneisen parameter, and specific heat (b) entropy per unit reference volume (c) minimum values of resistance functions R_ω and R_ξ needed to suppress melting and fracture in high-pressure Hugoniot states

tion beginning at 42% compression. Recall that decomposed products have null shear modulus. The Grüneisen parameter remains relatively constant until shock decomposition, beyond which it decreases due to increasing specific heat. Entropy jump across the shock increases monotonically with increasing pressure in Fig. 4(b) and is always non-negative in accordance with the thermodynamic restriction in the last of (4.2). The change in slope at $P \approx 25$ GPa arises from differences in thermodynamic properties of the reactants and products.

Respective resistance functions R_ω and R_ξ needed to prohibit melting and fracture in Hugoniot states, calculated in (4.21) and (4.22), are shown versus mean pressure $p = P - \frac{2}{3}\bar{\sigma}$ in Fig. 4(d). Melting is promoted by temperature above θ_G due to specific heat differences and the lower bulk and shear moduli of the melt relative to the glass (Table A.2). Function R_ω provides the resistance to melt from high pressure noted elsewhere [1, 4, 20, 155]. Under compressive loading, fracture is driven only by shearing energy from elasticity and extreme plastic flow. The latter is negligible, and the former increases initially then reduces to zero at $P \gtrsim 15$ GPa when shear strength, and thus deviatoric strain energy density, vanish. Modest resistance $R_\xi > 0$ is required at lower pressures to reflect experimental tendencies [64, 65]. The maximum value of $R_\xi(J^H)$ calculated this way for compression is $R_\xi = 95\Gamma_\xi/l_\xi$, reassuringly less than the value of $R_\xi^G = 115\Gamma_\xi/l_\xi$ in Table A.2 used to model spall of the glass in Section 4.3. The minimum melt resistance is notably larger than the fracture resistance but decreases rapidly at pressures exceeding the decomposition threshold since the products do not melt. These functions do not consider off-Hugoniot states within shock fronts that require a more in-depth computational study beyond the present scope. Furthermore, for comparison with experimental data, release waves have been deemed isentropic and thermoelastic per usual assumptions [20, 86, 142] and (4.14). Depending on thermodynamic properties, melting and/or decomposition might be possible on shock release if temperatures remain high enough while pressure reduces. Shock-release melting has been studied elsewhere for metals [172], as have shear localization- and fracture-induced melting that could arise at lower pressures [68, 107, 173].

4.2 Low-pressure shock propagation

At low impact stresses $P \lesssim P_P^H = 0.74$ GPa, structured steady waves are observed in planar shock compression experiments on PMMA after sufficient run distance. These wave forms, as inferred from free-surface velocity histories, comprise an initial elastic shock resulting from instantaneous glassy response, followed by a rounded rise to a terminal particle velocity nearly identical to half of the impact velocity for symmetric loading configurations [7, 29–31]. Such rounding, over finite rise times, originates from transient viscoelastic relaxation to equilibrium Hugoniot states. Constitutive parameters are representative of μ s time scales in the latter states, as discussed at the beginning of Section 4 (e.g., equilibrium Hugoniot stiffness exceeds quasi-static elastic stiffness).

Steady wave behavior in this regime is analyzed by adapting methods of Refs. [106, 121]. For $J > J_P^H = 0.937$, the response in (4.6) is thermoelastic, and none of fracture, melting, or decomposition occur: $\mathbf{F} = \mathbf{F}^E$, $J = J^E$, $\bar{F}^P = \lambda^P = 1$, $\gamma^P = \xi = \omega = \Xi = 0$. A single volumetric \mathbf{Y}_V and single shear \mathbf{Y}_S tensor state variable suffice here for viscoelasticity, so $\{\boldsymbol{\alpha}\} \rightarrow (\mathbf{Y}_V, \mathbf{Y}_S)$. Quantities corresponding to the head of the steady wave are labeled by $\square_i = \square^-$, where \square^- is the state immediately following the initial elastic shock front treated as a singular surface [29–31, 51]. The

\square^+ state ahead of the steady wave, and ahead of the initial shock, obeys (4.3). The state \square_i is determined using (4.5) and procedures of Section 4.1, albeit with instantaneous, rather than relaxed Hugoniot, thermoelastic properties defined in what follows. Quantities for final state at the tail of the steady wave are labeled \square_f . Even though the wave is of finite width (i.e., a “structured” shock), (4.2) apply because the wave is steady [102, 142]. Taking the \square^+ state for the entire wave form as (4.3) and \square_f as the end state, then (4.5) provide the equilibrium Hugoniot quantities at \square_f [31], where suitable relaxed thermodynamic properties are given later. The arbitrary datum time, at the head of the steady wave, is $t_i = 0$. The steady Lagrangian wave speed is \mathcal{U} .

For uniaxial strain with $J(X, t) = \partial x(X, t)/\partial X$, material and momentum conservation laws are

$$J = \partial v / \partial X, \quad \partial P / \partial X = -\rho_0 \partial v / \partial t. \quad (4.23)$$

Define the moving coordinate systems $Y(X, t)$ and resulting differential relations for function $f(Y)$:

$$Y = X - \mathcal{U}t, \quad \partial f / \partial X = df / dY, \quad \partial f / \partial t = -\mathcal{U} df / dY. \quad (4.24)$$

In a steady wave form, $J = J(Y)$, $v = v(Y)$, $P = P(Y)$, etc. Then (4.23) and (4.24) produce

$$\frac{dJ}{dY} = -\frac{1}{\mathcal{U}} \frac{dv}{dY}, \quad \frac{dP}{dY} = \rho_0 \mathcal{U} \frac{dv}{dY} \quad \Rightarrow \quad \frac{dP}{dY} = -\rho_0 \mathcal{U}^2 \frac{dJ}{dY}. \quad (4.25)$$

The rightmost equality in (4.25) is the differential stress-strain equation along the Rayleigh line with slope $dP/dJ = -\rho_0 \mathcal{U}^2$. In the present application, the domain over which (4.25) is used is the Rayleigh line connecting the instantaneous Hugoniot at \square_i to the relaxed Hugoniot at \square_f [30]. Integrating (4.25) between any two points in the steady wave form gives

$$\mathcal{U} [J] = -[v], \quad [P] = \rho_0 \mathcal{U} [v] = -\rho_0 \mathcal{U}^2 [J], \quad (4.26)$$

where $[\square]$ is the difference between the two points. Noting $\rho_0 = \rho J$, these agree with (4.2).

The longitudinal compressive stress P and its derivative obey the constitutive relations

$$P(J, \eta, \mathbf{r}_V, \mathbf{r}_S) = -\frac{\partial U(\mathbf{F}(J), \eta, \mathbf{r}_V, \mathbf{r}_S)}{\partial J}, \quad \frac{dP}{dY} = \frac{\partial P}{\partial J} \frac{dJ}{dY} + \frac{\partial P}{\partial \eta} \frac{d\eta}{dY} + \frac{\partial P}{\partial \mathbf{r}_V} : \frac{d\mathbf{r}_V}{dY} + \frac{\partial P}{\partial \mathbf{r}_S} : \frac{d\mathbf{r}_S}{dY}. \quad (4.27)$$

Equating the second of (4.27) with (4.25) and using the isentropic sound speed definition (4.14),

$$\frac{dJ}{dY} = \frac{1}{\rho_0 [(C_L)^2 - \mathcal{U}^2]} \left[\frac{\partial P}{\partial \eta} \frac{d\eta}{dY} + \frac{\partial P}{\partial \mathbf{r}_V} : \frac{d\mathbf{r}_V}{dY} + \frac{\partial P}{\partial \mathbf{r}_S} : \frac{d\mathbf{r}_S}{dY} \right] = -\frac{1}{\mathcal{U}} \frac{\partial J}{\partial t} \geq 0. \quad (4.28)$$

Both Y and J decrease from the head to the tail of the steady compression wave, and $C_L > \mathcal{U}$.

Equation (4.28) is integrated numerically for $J(Y)$ along the Rayleigh line from J_i to J_f , noting $dY = -\mathcal{U} dt$ at fixed X . For initial conditions $X_i = Y_i = 0 \leftrightarrow t_i = 0$, volume ratio J_i is the solution of (4.5) corresponding to \mathcal{U} using instantaneous constitutive parameters. Complementary initial conditions on P_i , θ_i , η_i , and v_i are obtained from this solution, and $(\mathbf{r}_V)_i = (\mathbf{r}_S)_i = \mathbf{0}$. End conditions for J_f are obtained from solution of (4.5) using relaxed Hugoniot constitutive parameters and

the same value of \mathcal{U} . The steady wave analysis terminates at this volume, when the Rayleigh line intersects the relaxed Hugoniot at (J_f, P_f) at time $t_f = -Y_f/\mathcal{U}$, whereby the constant end state is

$$J = J_f, \quad P = P_f; \quad \theta \rightarrow \theta_f, \quad \eta \rightarrow \eta_f, \quad \dot{\mathbf{Y}}_V \rightarrow \mathbf{0}, \quad \dot{\mathbf{Y}}_S \rightarrow \mathbf{0}, \quad [\forall t > t_f]. \quad (4.29)$$

If the relaxed Hugoniot pair (J_f, P_f) is intersected prior to attainment of the latter four conditions in (4.29) (e.g., total viscoelastic relaxation may require infinite time), then the latter are enforced as jump conditions on temperature, entropy, and internal variable rates at $t = t_f$ for consistency.

The thermoelastic model and thermoelastic properties, namely elastic constants and Grüneisen parameters, used in Section 4.1 are insufficient in the present setting, as the former depict a compromise between instantaneous and relaxed Hugoniot responses with transient viscoelastic effects excluded. Here in Section 4.2, distinct thermoelastic constants for instantaneous and relaxed Hugoniot states are defined following Refs. [29–31, 51], and free energy Ψ^G transitions from instantaneous to relaxed response via evolution of internal configurational variables \mathbf{Y}_V and \mathbf{Y}_S . Neither the instantaneous nor relaxed Hugoniot should be extrapolated to plastic states $P \gg P_P^H$.

According to the framework of Section 3.3, configurational energies Ψ_V^r, Ψ_S^r are not prescribed in analytical form, but can be obtained via numerical integration, for example (3.40) and (3.47), where internal variable rates are given by (3.45) and (3.52). In the current analysis, an analytical form of $P(J, \theta, \mathbf{Y}_V, \mathbf{Y}_S)$, and therefore of Ψ_V^r and Ψ_S^r , is required to accurately calculate $\partial P/\partial \mathbf{Y}_V$, $\partial P/\partial \mathbf{Y}_S$, and $d\eta/dY$ entering (4.28). Strain-like internal variables referred to Lagrangian coordinates are related to scalar volumetric strain-like measure e_V^r and spatial deviatoric measure $\bar{\mathbf{e}}^r$:

$$\mathbf{Y}_V = (\mathbf{R}^E)^\top e_V^r \mathbf{R}^E, \quad \mathbf{Y}_S = (\mathbf{R}^E)^\top \bar{\mathbf{e}}^r \mathbf{R}^E, \quad \bar{\mathbf{e}}^r = (\bar{\mathbf{e}}^r)^\top, \quad \text{tr } \bar{\mathbf{e}}^r = 0. \quad (4.30)$$

For isotropic viscoelastic response, $\Psi_V^r = \Psi_V^r(e_V^r, e_V^E, \theta)$ and $\Psi_S^r = \Psi_S^r(\bar{\mathbf{e}}^r, \bar{\mathbf{e}}^E, \theta)$. These are not needed individually, but rather are combined into a total viscoelastic free energy that, similar to the example in Ref. [33], depends only on the differences $\Delta e_V = e_V^E - e_V^r$ and $\Delta \bar{\mathbf{e}} = \bar{\mathbf{e}}^E - \bar{\mathbf{e}}^r$:

$$\Psi^r = \Psi^r(e_V^r, \bar{\mathbf{e}}^E; e_V^r, \bar{\mathbf{e}}^r; \theta) = \Psi^r(\Delta e_V, \Delta \bar{\mathbf{e}}, \theta), \quad \hat{\Psi}^r = \Psi^r(\Delta e_V = e_V^E, \Delta \bar{\mathbf{e}} = \bar{\mathbf{e}}^E, \theta). \quad (4.31)$$

Function $\hat{\Psi}^r$ produces instantaneous response, wherein configurational variables in (4.30) vanish. Viscous stresses $\mathbf{Q}_l^V, \mathbf{Q}_m^S$ and their spatial counterparts $\mathbf{q}_l^V, \mathbf{q}_m^S$ are defined similarly but not identically to (3.40), (3.41), (3.47), and (3.48), where subscripts $l = 1$ and $m = 1$ are not needed:

$$\mathbf{Q}^V = J(\mathbf{R}^E)^\top \mathbf{q}^V \mathbf{R}^E, \quad \mathbf{q}^V = q^V \mathbf{1} = \frac{1}{J} \frac{\partial \Psi^r}{\partial e_V^E} \mathbf{1} = -\frac{1}{J} \frac{\partial \Psi^r}{\partial e_V^r} \mathbf{1} = -(p_V^r + p_S^r) \mathbf{1}, \quad \hat{\mathbf{q}}^V = \frac{1}{J} \frac{\partial \hat{\Psi}^r}{\partial e_V^E}; \quad (4.32)$$

$$\mathbf{Q}^S = J(\mathbf{R}^E)^\top \mathbf{q}^S \mathbf{R}^E, \quad \mathbf{q}^S = \frac{1}{J} \frac{\partial \Psi^r}{\partial \bar{\mathbf{e}}^E} = -\frac{1}{J} \frac{\partial \Psi^r}{\partial \bar{\mathbf{e}}^r} = \bar{\mathbf{q}}^r_S, \quad \hat{\mathbf{q}}^S = \frac{1}{J} \frac{\partial \hat{\Psi}^r}{\partial \bar{\mathbf{e}}^E}. \quad (4.33)$$

Two relaxation times $\tau_l^V \rightarrow \tau^V = \text{const}$ and $\tau_m^S \rightarrow \tau^S = \text{const}$ are sufficient for the current problem. Analogs of (3.41), (3.42), (3.48), and (3.49) are as follows, with initial conditions at $t_0 \rightarrow t_i = 0$:

$$\dot{q}^V + \frac{q^V}{\tau^V} = D_t \hat{q}^V, \quad q^V(t) = q_0^V \exp\left[\frac{-t}{\tau^V}\right] + \int_{0^+}^t \exp\left[\frac{s-t}{\tau^V}\right] D_s \hat{q}^V ds, \quad q_0^V = \frac{1}{J} \frac{\partial \hat{\Psi}^r}{\partial e_V^E} \Big|_{t=0}; \quad (4.34)$$

$$\dot{\mathbf{q}}^S + \frac{\mathbf{q}^S}{\tau^S} = D_t \hat{\mathbf{q}}^S, \quad \mathbf{q}^S(t) = \mathbf{q}_0^S \exp\left[\frac{-t}{\tau^S}\right] + \int_{0^+}^t \exp\left[\frac{s-t}{\tau^S}\right] D_s \hat{\mathbf{q}}^S ds, \quad \mathbf{q}_0^S = \frac{1}{J} \frac{\partial \hat{\Psi}^r}{\partial \bar{\mathbf{e}}^E} \Big|_{t=0}. \quad (4.35)$$

The spatial tensor rate equation (4.35) is valid generally only if continuum spin $\dot{\mathbf{R}}\mathbf{R}^\top = \mathbf{0}$; otherwise an objective rate of \mathbf{q}^S should be used. The present form is acceptable for uniaxial strain wherein $\mathbf{R} = \mathbf{R}^E = \mathbf{1}$. Also in the uniaxial setting, $\mathbf{q}^S = \text{diag}(q_{11}^S, -\frac{1}{2}q_{11}^S, -\frac{1}{2}q_{11}^S)$, and $\hat{\mathbf{q}}^S$ is of similar form, so (4.35) need only be integrated for a single component (e.g., q_{11}^S).

Combining (4.32) with (4.34), combining (4.33) with (4.35), and transforming the integration variable from t to Y , two zero-valued functions $Z^V(Y)$ and $Z^S(Y)$ are defined:

$$Z^V(Y) = \frac{1}{J} \frac{\partial \Psi^r(e_V^r(Y), \bar{\mathbf{e}}^r(Y), \dots)}{\partial e_V^r} + q_0^V \exp\left[\frac{Y}{\mathcal{U}\tau^V}\right] + \int_{0^+}^Y \exp\left[\frac{Y-s}{\mathcal{U}\tau^V}\right] D_s \hat{q}^V ds = 0, \quad (4.36)$$

$$Z^S(Y) = \frac{1}{J} \frac{\partial \Psi^r(e_V^r(Y), \bar{\mathbf{e}}^r(Y), \dots)}{\partial \bar{e}_{11}^r} + (q_0^S)_{11} \exp\left[\frac{Y}{\mathcal{U}\tau^S}\right] + \int_{0^+}^Y \exp\left[\frac{Y-s}{\mathcal{U}\tau^S}\right] D_s \hat{q}_{11}^S ds = 0. \quad (4.37)$$

Equations (4.36) and (4.37) are solved simultaneously, by iteration, for $e_V^r(Y)$ and $\bar{e}_{11}^r(Y)$ at each increment dY in the wave. Other potentially nonzero components of $\bar{\mathbf{e}}^r$ are $\bar{e}_{22}^r = \bar{e}_{33}^r = -\frac{1}{2}\bar{e}_{11}^r$. Derivatives are obtained via standard difference approximations taken at each increment:

$$\frac{de_V^r}{dY} = \lim_{dY \rightarrow 0} \frac{\arg 0(Z^V(Y + dY)) - \arg 0(Z^V(Y))}{dY}, \quad \frac{d\bar{e}_{11}^r}{dY} = \lim_{dY \rightarrow 0} \frac{\arg 0(Z^S(Y + dY)) - \arg 0(Z^S(Y))}{dY}, \quad (4.38)$$

where arguments of $Z^V = 0$ and $Z^S = 0$ are $e_V^r(Y)$ and $\bar{e}_{11}^r(Y)$, respectively, from (4.36) and (4.37).

Let $\square^{G,E}$ and $\square^{G,I}$ label coefficients of respective relaxed and instantaneous thermoelastic responses. Specifically, these comprise $B_i^{G,*}$ and $\Gamma_i^{G,*}$ where $i = 0, 1, 2, 3$ and $i = 0, 1, 2$ for bulk moduli and Grüneisen parameters, and shear modulus parameters $G_0^{G,*}$ and $G_p^{G,*}$. Values are in Table A.3. Specific heat parameters c_{V0}^G and c_θ^G , and $G_\theta^{G,*}$, are the same for relaxed and instantaneous states, all unchanged from Table A.1. Higher-order bulk moduli $B_i^{G,E} = B_i^{G,I}$ for $i > 0$. The viscoelastic free energy function combining volumetric and shear response is, valid for $e_V^E \leq 0$,

$$\begin{aligned} \Psi^r = & (B_0^{G,I} - B_0^{G,E})(\Delta e_V)^2 \left[\frac{1}{2} - \frac{1}{6}B_1^{G,E}\Delta e_V + \frac{1}{24}B_2^{G,E}(\Delta e_V)^2 - \frac{1}{120}B_3^{G,E}(\Delta e_V)^3 \right] \\ & + [(G_0^{G,I} - G_0^{G,E}) - (B_0^{G,I}G_p^{G,I} - B_0^{G,E}G_p^{G,E})\Delta e_V + (B_0^{G,I}G_2^{G,I} - B_0^{G,E}G_2^{G,E})(\Delta e_V)^2]\Delta \bar{\mathbf{e}} : \Delta \bar{\mathbf{e}} \\ & - c_{V0}^G(\theta - \theta_0)\Delta e_V[(\Gamma_0^{G,I} - \Gamma_0^{G,E}) + \frac{1}{2}(\Gamma_1^{G,I} - \Gamma_1^{G,E})\Delta e_V + \frac{1}{6}(\Gamma_2^{G,I} - \Gamma_2^{G,E})(\Delta e_V)^2]. \end{aligned} \quad (4.39)$$

The total free energy $\Psi = \Psi_V^{G,E} + \Psi_S^{G,E} + \Psi_\beta^{G,E} + \Psi^{G,\theta} + \Psi^r$ furnishes the complete instantaneous thermoelastic response when $e_V^r = 0 \Rightarrow \Delta e_V = e_V^E$ and $\bar{\mathbf{e}}^r = \mathbf{0} \Rightarrow \Delta \bar{\mathbf{e}} = \bar{\mathbf{e}}^E$. The relaxed Hugoniot energy, but not all of its strain derivatives, is recovered when $\Delta e_V = 0$ and $\Delta \bar{\mathbf{e}} = \mathbf{0}$, giving $\Psi^r = 0$.

Quantities on the right side of the shock structure differential equation (4.28) can be found analytically using (4.32), (4.33), (4.39), and entropy production from $\mathfrak{D} = \mathfrak{D}_V^r + \mathfrak{D}_S^r$:

$$\frac{\partial P}{\partial \mathbf{r}_V} : \frac{d\mathbf{r}_V}{dY} = -\left\{ J \left[\frac{\partial p^r}{\partial J} \Big|_{\theta, \bar{\mathbf{e}}^r} - \frac{\theta\Gamma}{J} \frac{\partial p^r}{\partial \theta} \Big|_{J, \bar{\mathbf{e}}^r} \right] - q^V \right\} \frac{de_V^r}{dY}, \quad \frac{\partial P}{\partial \mathbf{r}_S} : \frac{d\mathbf{r}_S}{dY} = \frac{dq_{11}^S}{d\bar{e}_{11}^E} \Big|_{\theta, e_V^r} \frac{d\bar{e}_{11}^r}{dY}, \quad (4.40)$$

$$\frac{\partial P}{\partial \eta} \Big|_{J, e_V^r, \bar{\mathbf{e}}^r} \frac{d\eta}{dY} = \frac{-(\mathfrak{D}_V^r + \mathfrak{D}_S^r)}{\mathcal{U}c_V^G} \frac{\partial P}{\partial \theta} \Big|_{J, e_V^r, \bar{\mathbf{e}}^r} = \frac{J}{c_V^G} \left[q^V \frac{de_V^r}{dY} + \frac{3}{2}q_{11}^S \frac{d\bar{e}_{11}^r}{dY} \right] \frac{\partial P}{\partial \theta} \Big|_{J, e_V^r, \bar{\mathbf{e}}^r}. \quad (4.41)$$

Bulk shock velocity κ^V of Section 3.8 is not needed in the current analytical-numerical method, and shear viscosity μ^V vanishes by definition in the glass phase. Adiabatic temperature rise in the wave is obtained by integrating the following form of energy balance (3.130) with respect to Y :

$$\frac{d\theta}{dY} = -\frac{\theta}{J} \left[\Gamma - \frac{4}{3} \frac{G^{G,E}}{c_V^G} \ln J \right] \frac{dJ}{dY} + \frac{J}{c_V^G} \left[q^V - \theta \frac{\partial q^V}{\partial \theta} \right] \frac{de_V^r}{dY} + \frac{3}{2} \frac{J}{c_V^G} \left[q_{11}^S - \theta \frac{\partial q_{11}^S}{\partial \theta} \right] \frac{d\bar{e}_{11}^r}{dY}. \quad (4.42)$$

Given the solution $J = J(Y)$ from (4.28), particle velocity from (4.26) is $v(Y) = v_i + \mathcal{U}[J_i - J(Y)]$.

The “critical strain gradient” $(\partial J/\partial X)^-$ immediately behind the initial instantaneous shock, for which a steady wave exists, can be derived in closed form using various thermodynamic frameworks [106, 118–120, 174, 175]. For the present viscoelastic framework and initial conditions, the analytical solution derived in Ref. [106] applies, here specialized to the simpler case of a single-phase solid rather than solid-fluid mixture. Denote by $\delta_t \square$ the time derivative of a quantity $\square(X, t)$ with respect to an observer moving with the shock at Lagrangian speed \mathcal{U} : $\delta_t \square = \dot{\square} + \mathcal{U} \partial \square / \partial X$. The shock evolution equation for strain amplitude $\llbracket J(X, t) \rrbracket = J^-(X, t) - 1$ is [106]:

$$\delta_t \llbracket J \rrbracket = \mathcal{U} \frac{(1 - \hat{\xi})(2 - \hat{\zeta})\{\Lambda - (\partial J/\partial X)^-\}}{(3\hat{\xi} + 1) - \hat{\zeta}(3\hat{\xi} - 1)}, \quad \Lambda = \frac{1 + \llbracket J \rrbracket}{(1 - \hat{\xi})\hat{C}^-} \left\{ \frac{\rho_0}{J^-} [\mathbf{L}^- : \dot{\mathbf{a}}^-] \right\}. \quad (4.43)$$

For the current application, the requisite mechanical and thermodynamic quantities are

$$\begin{aligned} \hat{C} &= \rho_0(C_L)^2, & \hat{\xi} &= (\mathcal{U}/C_L^-)^2, & \hat{G} &= -\rho\theta\Gamma, & \hat{\zeta} &= \hat{G}^- \llbracket J \rrbracket / (\rho_0\theta^-), & \boldsymbol{\pi} &= -\{q^V, \mathbf{q}^S\}, \\ \mathbf{a} &= \{e_V^r, \bar{\mathbf{e}}^r\}, & \dot{\mathbf{a}} &= -\mathcal{U} \left\{ \frac{de_V^r}{dY}, \frac{d\bar{\mathbf{e}}^r}{dY} \right\}, & \mathbf{A} &= -\frac{\partial P}{\partial \mathbf{a}} \Big|_{J, \eta}, & \mathbf{L} &= \frac{1}{\rho_0 \mathcal{U}} \left[\mathbf{A} - \frac{\hat{G}}{\rho\theta} \boldsymbol{\pi} \right]. \end{aligned} \quad (4.44)$$

When $\Lambda = \Lambda_c = (\partial J/\partial X)^-$, the initial elastic shock is steady with $J^-(t) = J_i = \text{const}$, $P^-(t) = P_i = \text{const}$, and $\mathcal{U} = \text{const}$, consistent with steady-wave assumptions of Section 4.2. Calculations verified that this closed-form solution agrees with the numerical outcome of (4.28) at $Y = Y_i = 0$.

Outcomes of the analysis are shown in Fig. 5. Model depictions of instantaneous and relaxed stress-volume and shock velocity-particle velocity Hugoniots are compared with experimental data [7, 51] in Fig. 5(a) and Fig. 5(b). These data have been used to calibrate (4.39). Instantaneous curves exceed relaxed counterparts. Temperature from the relaxed rather than instantaneous model more closely matches experiment [168] in Fig. 5(c). Conversely, instantaneous sound speed C_L more closely agrees with experimental release velocities [7] in Fig. 5(d). Failure of the model to capture release wave data for $v \gtrsim 150$ m/s is not unexpected. At higher velocities, plastic deformation occurs in PMMA and (4.39) is decreasingly accurate, showing that this energy function and its parameter values should not be extrapolated to higher pressures. Similar issues are reported in other studies [29–31]. The current steady wave analysis is limited to particle velocities $v_i \lesssim 125$ m/s for the initial instantaneous elastic shock front, for which accuracy of C_L is confirmed. For $0 < v \lesssim 170$ m/s, C_L and \mathcal{U} increase monotonically with increasing v , and $C_L/\mathcal{U} > 1$.

The steady wave analysis is applied to three experiments of Ref. [29], where loading protocols are listed in Table 1. Nominal impact velocity is very close to twice the final particle velocity in the tail of the steady wave [29, 30]. Particle velocity histories computed via (4.26) with numerical

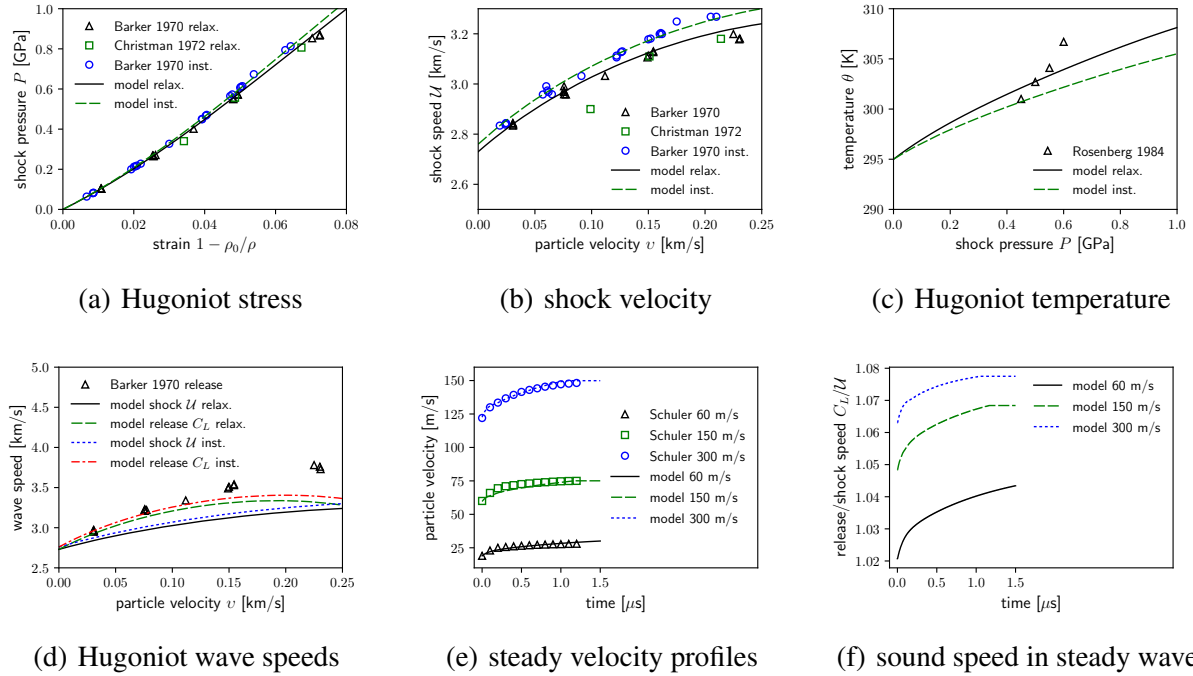


Figure 5. Low-pressure shock response of PMMA: (a) instantaneous and relaxed shock pressure P from model and experiments [7, 60] (b) instantaneous and relaxed shock velocity U from model and experiments [7, 60] (c) instantaneous and relaxed Hugoniot temperature θ from model and experiments [168] (d) shock U and sound C_L velocity from model and experiments [7] (e) steady profiles of particle velocity v vs. time from model and experiments [29] (f) ratio of local sound speed C_L to steady wave velocity U (model)

Table 1. Steady wave loading conditions (model); \square_i, \square_f denote initial, final states

Nominal impact [m/s]	Wave speed U [m/s]	Volume J_i, J_f	Temperature θ_i, θ_f
60	2834	0.9933, 0.9892	296.06, 297.03
150	2966	0.9799, 0.9747	298.05, 299.59
300	3120	0.9607, 0.9520	300.75, 303.41

Table 2. Critical strain gradient $\Lambda_c = (\partial J / \partial X)^-$ for steady waves in PMMA

Nominal impact [m/s]	Strain $1 - J^-$	Λ_c [1/m] (experiment [117])	Λ_c [1/m] (model, eq. (4.43))
60	0.0067	—	6.4
150	0.0201	10.0 ± 3	9.4
220	0.0300	13.7	—
300	0.0393	16.3 ± 6	16.3

integration of (4.28) are compared with data extracted from free surface profiles [29] in Fig. 5(e). A best fit to all three experimental profiles is obtained via adjustment of relaxation times τ^V and τ^S , where the same two values in Table A.3 are applied simultaneously to all three profiles. Closest agreement is obtained for $\tau^V/\tau^S \approx 18.5$, meaning slower relaxation for volumetric versus shear viscoelasticity. Axial stress $P(t)$ in the steady wave at X follows identical trends because its change is $\rho_0 \mathcal{U} \times$ the particle velocity change. Ratio $C_L/\mathcal{U} > 1$ increases monotonically from its initial value at the head to a constant at tail of the wave—attained when the Rayleigh line for each imposed \mathcal{U} intersects the relaxed P versus ρ Hugoniot—for all three cases in Fig. 5(f), a necessary condition for steady wave propagation in nonlinear viscoelastic materials with memory [30]. The critical strain gradient $\Lambda = \Lambda_c$ for steady wave propagation predicted by the second of (4.43) is compared with experimental data [117] in Table 2. Although experimental data demonstrate wide bounds on precision, close agreement of the model with median experimental values is encouraging.

4.3 Spall fracture

The spall process in PMMA is modeled by uniaxial tension calculations. The objective is determination of properties and parameters for crazing and dynamic tensile fracture at very high rates with concurrent evaluation of model capabilities. This is facilitated by comparison with experimental spall data across a range of strain rates and starting temperatures [77, 79, 176]. Notably, Ref. [77] reports an increase in spall strength with increasing rate, and Ref. [79] reports a decrease in spall strength with increasing initial temperature spanning the glass transition. When strain rates are not reported explicitly as in Refs. [79, 176], free surface velocity profiles and sound speeds are used to calculate strain rates during the spall process [78] to be used as loading conditions for the model.

For initial temperatures $\theta_i = \theta_0$, viscoelastic relaxation is not incorporated explicitly, but calculations using instantaneous (e.g., $G_0^{G,I}, B_0^{G,I}$) and relaxed Hugoniot (e.g., $G_0^{G,E}, B_0^{G,E}$) properties bound the predicted response. Results later show that differences among bounded spall strengths are negligible. For $\theta_i > \theta_0$, viscoelastic properties are not well known: τ^V and τ^S should include temperature dependence. Such temperature dependence has been safely omitted in Section 4.2 where $|\theta - \theta_0| \lesssim 8.4$ K. In Section 4.3, like Section 4.1, viscoelastic response is implicitly included in the Hugoniot properties of the glass and melt. Bulk and shear moduli of the melt phase are calculated using sound speeds and shock velocity reported in Ref. [79] for $\theta_i = 413$ K. Specific heats differ among glass and melt (Table A.1); Grüneisen parameters $\Gamma_0^{*,E}$ are assumed the same.

The applied axial strain rate is $j^F > 0$. Isochoric plastic strain from shear yielding $\gamma^P(t)$, free volume change $\varphi(t)$, porosity from crazing or chain scission $\phi(t)$, and damage from fracture $\xi(t)$ can all be nonzero. Impact stresses and temperatures are far below decomposition thresholds, so $\Xi(t) = 0$. Experimental data for impacts below and above the HEL show little or no difference in spall strength [176], so nonzero initial plastic deformation is excluded for simplicity. Subsequent calculations demonstrate isochoric plastic deformation during tensile extension is small. Adiabatic conditions are assumed, and bulk shock viscosity of Section 3.7 is inactive for tensile loading. Shear viscosity is not impossible for the melt phase at high temperature. However, data in Ref. [177] show a logarithmic decrease in μ^V with increasing strain rate. Extrapolating such data to the present regime (i.e., j^F on order of 10^4 to 10^5 /s) gives viscous shear stresses of order 10 kPa,

negligible relative to spall strengths of order 100 MPa and therefore omitted without important consequence. Current 1-D calculations are restricted to a single material point at X undergoing axial strain rate $\dot{J}^F = J_i^{-1/3} \partial v / \partial X$. Stress wave interactions and the width of the spall-damaged zone are not captured explicitly; these require advanced numerical methods with space-time discretization beyond the current scope. Initial conditions are $J^F(0) = 1$, $\gamma^P(0) = \varphi(0) = \phi(0) = \xi(0) = 0$. Initial temperatures vary, where $\theta_i \geq \theta_0$. If $\theta_i > \theta_0$, then an initial spherical thermal expansion $J_i \approx \exp(\Gamma_0^{*,E} c_{V0}^*(\theta_i - \theta_0) / B_0^{*,E})$ alleviates initial thermal pressure.

Consistent with (3.3), material symmetry, and above assumptions, the deformation gradient is

$$\mathbf{F} = \begin{bmatrix} J^F & 0 & 0 \\ 0 & 1 & 0 \\ 0 & 0 & 1 \end{bmatrix} (J_i)^{1/3} = \mathbf{F}^E \bar{\mathbf{F}}^P \mathbf{F}^\phi = \begin{bmatrix} F_{11}^E & 0 & 0 \\ 0 & F_{22}^E & 0 \\ 0 & 0 & F_{22}^E \end{bmatrix} \begin{bmatrix} \bar{F}^P & 0 & 0 \\ 0 & \bar{F}^{P-1/2} & 0 \\ 0 & 0 & \bar{F}^{P-1/2} \end{bmatrix} \begin{bmatrix} F^\phi & 0 & 0 \\ 0 & 1 & 0 \\ 0 & 0 & 1 \end{bmatrix}. \quad (4.45)$$

The following kinematic and stress relations hold, where $J^\phi = F^\phi = 1/(1 - \phi)$ and \mathbf{F}^E contains J_i :

$$J = J_i J^F = J^E J^\phi = \frac{F_{11}^E (F_{22}^E)^2}{1 - \phi}, \quad F_{11}^E = \frac{J_i^{1/3} J^F}{\bar{F}^P F^\phi}, \quad F_{22}^E = J_i^{1/3} (\bar{F}^P)^{1/2}, \quad e_V^E = \ln J^E = \ln J - \ln J^\phi; \quad (4.46)$$

$$\bar{e}_{11}^E = -2\bar{e}_{22}^E = \ln F_{11}^E - \frac{1}{3} e_V^E, \quad \bar{\mathbf{e}}^E = \text{diag}(\bar{e}_{11}^E, \bar{e}_{22}^E, \bar{e}_{22}^E), \quad \gamma^P = \sqrt{3} \ln \bar{F}^P, \quad \mathbf{A} = \bar{\mathbf{F}}^P (\bar{\mathbf{F}}^P)^\top; \quad (4.47)$$

$$\lambda^P = \{\frac{1}{3}[(\bar{F}^P)^2 + 2/\bar{F}^P]\}^{1/2}, \quad \bar{\mathbf{N}}^P = \sqrt{\frac{2}{3}} \text{diag}(1, -\frac{1}{2}, -\frac{1}{2}), \quad \tau^A = \bar{\mathbf{M}}^A : \bar{\mathbf{N}}^P = \frac{\sqrt{3}}{2} \bar{M}_{11}^A; \quad (4.48)$$

$$\bar{\mathbf{M}}^E = J \bar{\boldsymbol{\sigma}} = J \text{diag}(\bar{\sigma}_{11}, -\frac{1}{2} \bar{\sigma}_{11}, -\frac{1}{2} \bar{\sigma}_{11}), \quad \tau^E = \bar{\mathbf{M}}^E : \bar{\mathbf{N}}^P = \frac{\sqrt{3}}{2} J \bar{\sigma}_{11} = \frac{\sqrt{3}}{3} J \bar{\sigma}; \quad (4.49)$$

$$\mathbf{N}_\phi = \text{diag}(1, 0, 0), \quad M_\phi^E = M_{11}^E = J \sigma_{11} = J(\bar{\sigma}_{11} - p) = J P, \quad P = \sigma_{11} \geq 0. \quad (4.50)$$

Axial stress, positive in tension, is P . Spall strength is identified as $P_c = \max_{t \in [0, \infty)} P(t)$.

Unlike static equilibrium conditions for Hugoniot response in Section 4.1, $\gamma^P(t) \geq 0$. Equation (3.68) is used in dynamic form, with literature parameters in Table A.2. In (3.69), $f_R^P = 1$ in tensile loading in accordance with (4.17). Equations (4.18) and (4.19) are used for isotropic hardening/softening and free volume, consistent with parameters for the shock-loading regime in Table A.2. Porosity rate ϕ from crazing in the glass or from scission in the melt is found from (3.76). Fracture rate ξ is given by (2.34), with Φ in (3.75). Surface energies Γ_ξ^G and Γ_ξ^M are constants in Table A.2. A constant resistance R_ξ^G is sufficient for the glass phase, while linear temperature dependence of R_ξ^M is needed to capture experimental data:

$$R_\xi^G = R_{\xi0}^G, \quad R_\xi^M = R_{\xi0}^M [1 + \alpha_{\xi\theta}^M (\theta / \theta_G - 1)]. \quad (4.51)$$

A recent study [178] similarly modeled a change in spall properties across a solid-solid (phase) transition, there for metals. Dissipation from $\mathfrak{D}^P = \tau^P \dot{\gamma}^P$, $\mathfrak{D}^\phi = M_\phi^E \dot{\phi} / (1 - \phi)$, and $\mathfrak{D}^\xi = \zeta \dot{\xi}$ contributes to temperature rate calculated via (3.130), as do thermoelastic coupling and quantities (3.125) and (3.128). For comparison with elevated temperature data, $\omega(t) = 0$ for $\theta_i \leq 391$ K and

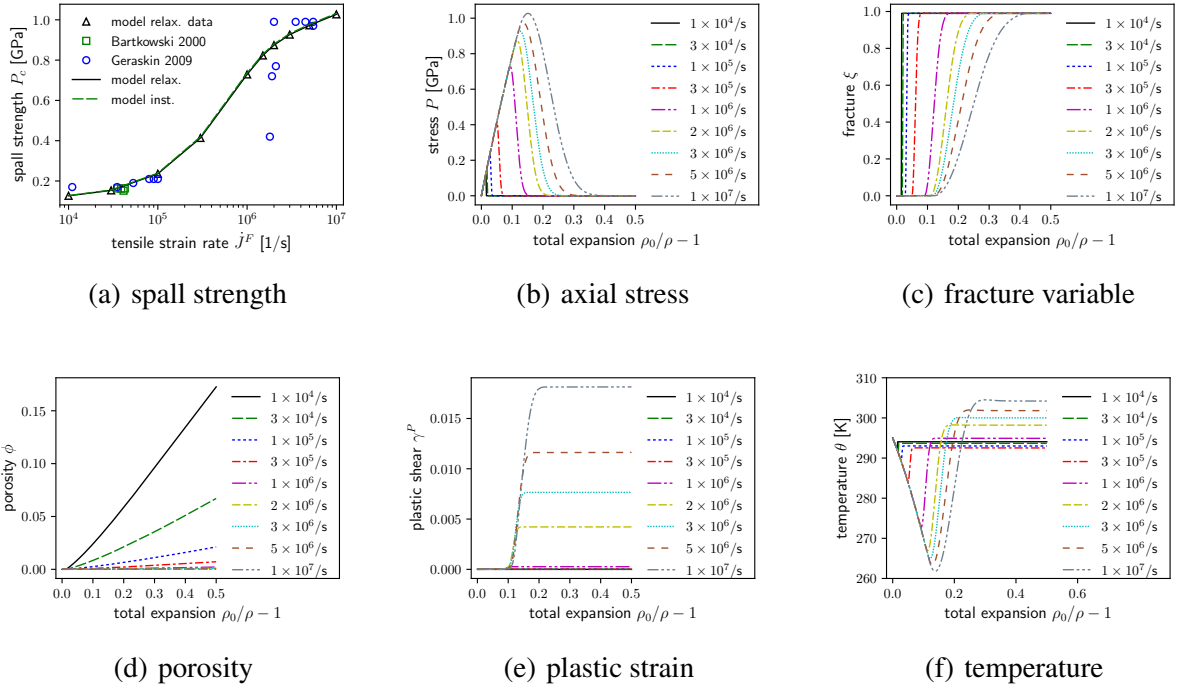


Figure 6. Room-temperature spall response of PMMA: (a) spall stress P_c vs. strain rate J^F from model (relaxed Hugoniot and instantaneous elastic properties) and experiments [77, 176] (b) axial stress P vs. expansive strain $J - 1$ (c) order parameter ξ (d) void fraction ϕ (e) isochoric plastic strain γ^P (f) temperature θ

$\omega(t) = 1$ for $\theta_i \geq 403$ K, as suggested by observations on the PMMA in Ref. [79] that appears to have a slightly higher glass transition temperature θ_G . Neither melting nor freezing are assumed to occur during dynamic deformation (i.e., $\dot{\omega} = 0$), as assumed likewise in Section 4.1. Pressures and time scales are assumed to inhibit such transitions. Degradation of $\Psi_{\beta}^{M,E}$ by f_V^E is omitted for the melt phase to avoid net negative dissipation from release of this (negative) energy. Magnitude of the latter is large due to initial thermal expansion and high specific heat of the melt phase.

Spanning rates in Refs. [77, 176], for room-temperature calculations (i.e., $\theta_i = \theta_0$), imposed values of J^F range from 10^4 to 10^7 /s. For elevated temperature calculations, from velocity profiles in Ref. [79], the following loading conditions (θ_i, J^F) are modeled in units of (K, 10^4 /s): (298, 5.48), (331, 4.84), (361, 3.78), (380, 3.19), (391, 2.95), (403, 1.33), (413, 1.31). Strain rate during spall tends to decrease with increasing temperature as the material becomes more compliant.

Results for $\theta_i = \theta_0 = 295$ K are reported in Fig. 6. Spall strength P_c is compared with experimental data [77, 176] in Fig. 6(a). Many trends are similar; agreement is modest. An outlying experimental data point corresponding to $P_c = 0.42$ GPa at $J^F = 1.8 \times 10^6$ /s is noted, and spall strength tends to attain a flatter plateau at the highest rates in experiments. According to the model, spall strength increases relatively slowly with strain rate up to $\approx 10^5$ /s, increases rapidly between 10^5 and 10^6 /s, then increases slowly again at even higher rates. Results have been achieved by adjusting five parameters in Table A.2: $\dot{\epsilon}_0$, n , and c_{ξ}^{ϕ} for crazing along with $R_{\xi_0}^G$ and β_{ξ} for frac-

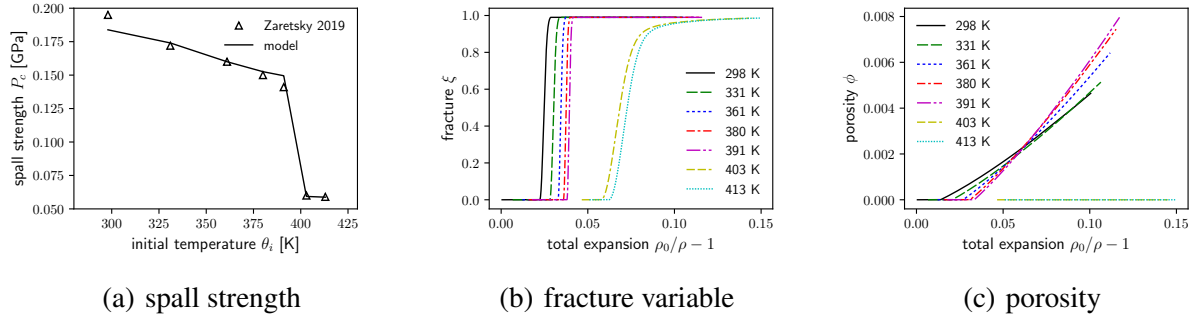


Figure 7. Elevated-temperature spall response of PMMA: (a) spall stress P_c vs. strain rate J^F from model and experiments [79] (b) order parameter ξ vs. expansive strain $J - 1$ (c) void fraction ϕ

ture. Spall strength P_c is highly sensitive to craze-induced porosity that initiates brittle fracture in the glass. Outcomes in Fig. 6(a) are nearly indistinguishable whether instantaneous or relaxed Hugoniot elastic constants are used, suggesting transient effects of viscoelasticity should be small.

Predictions for axial stress P , fracture order parameter ξ , void volume fraction ϕ , plastic shear strain γ^P , and temperature θ are shown versus total (including thermal) expansion $J - 1$ in the remaining five parts of Fig. 6, where each curve corresponds to a strain rate J^F listed in the legend. The slower the rate of increase of ξ with J in Fig. 6(c), the larger the peak stress attained in Fig. 6(b). Greater terminal porosities are achieved in Fig. 6(d) for lower expansion rates because more time is available for rate-dependent void growth; time needed for spall decreases with increasing J^F . The highest plastic shear strains are attained for highest strain rates in Fig. 6(e) since a larger driving shear stress is achieved prior to load drop, and plastic strain-rate sensitivity is small compared to that for craze strain: $m/n \approx 0.05$. Temperature in Fig. 6(f) initially decreases with increasing strain and tensile pressure due to thermoelastic coupling. After the onset of fracture, temperature increases due to dissipation and reduction of the tangent bulk modulus from damage.

Outcomes for higher $\theta_i \in [298, 413]$ K are shown in Fig. 7. Close agreement with experimental values obtained from pull-back signals [79] is witnessed in Fig. 7(a). The severe drop in P_c above the glass transition is evident for $\theta_i > 391$ K. Results are obtained by calibration of $W_{\xi_0}^M$ and $\alpha_{\xi\theta}^M$ in Table A.2 without adjusting any properties assigned previously to achieve Fig. 6. Evolution of ξ and ϕ are shown in respective Fig. 6(b) and Fig. 6(c), where initial temperatures for each curve are given in the legend. Total expansion J contains thermal expansion J_i . Thus, $J(0) > 1$ and J_i increases with θ_i . Initial expansion is higher in the melt due to higher coefficient of thermal expansion, manifesting from lower bulk modulus and higher specific heat [2, 4]. Below the glass transition, spall strength decreases with increasing temperature because strain rate decreases concurrently. Similar to the case for room-temperature results in Fig. 6, lower strain rates here at higher starting temperatures correlate with higher porosity from crazing below the glass transition in Fig. 7(c), leading to smaller peak stresses and lower spall strength. Plastic strain λ^P is too small (i.e., $\lambda^P(t) \ll \lambda_\phi^P = 1.39$) for cavitation and pore growth by chain scission in the melt. Thus $\phi = 0$ for $\theta_i \geq 403$ K in Fig. 7(c), and spall fracture occurs in the melt by strain-energy driven damage to rupture in the absence of crazing or void growth. Although the rate of increase in ξ with J is more

gradual in melt than the glass in Fig. 7(b), strength P_c is lower in the former. This is a net product of low melt-to-glass ratios of threshold fracture energy, Hugoniot bulk modulus, and Hugoniot shear modulus in Tables A.2 and A.3: $W_{\xi_0}^M/W_{\xi_0}^G \approx 0.06$, $B_0^{M,E}/B_0^{G,E} \approx 0.8$, and $G_0^{M,E}/G_0^{G,E} \approx 0.65$.

5 Conclusions

A constitutive framework has been established for the dynamic thermomechanical response of amorphous polymers applicable to extreme pressures and loading rates. The framework accounts for nonlinear thermoelasticity, isochoric plasticity, crazing, and rupture. Fracture, melting across the glass transition, and shock decomposition across the high-pressure transition are captured by distinct order parameters enabling a smooth, thermodynamically consistent material response.

The model has been applied toward PMMA. Experimental Hugoniot data are well-represented to shock pressures up to 120 GPa where temperatures exceed 4200 K. On the principal Hugoniot, decomposition begins at respective shock pressure and temperature of 25.7 GPa and 1289 K and is 90% complete at 42 GPa and 2124 K. A continuous decomposition process enables shock and release velocities to increase continuously with particle velocity. Kinetic barriers preclude fracture and melting at high pressure; the latter exceed the former in magnitude. Low-pressure steady waves have been adequately represented using a single relaxation time for each of bulk and shear viscoelasticity. Shear relaxation time is smaller than bulk relaxation time. Experimental spall strengths are reasonably captured (with a few exceptions): spall resistance increases with increasing expansion rate and decreasing temperature. Spall fracture is dominated by crazing at temperatures below the glass transition; rupture occurs without crazing above the glass transition.

Calculations in the present study have been limited to one spatial dimension. Implementation in a 3-D numerical scheme (e.g., finite element or hydrocode) is foreseen as a necessary future step to address more complicated loading conditions.

A Appendix: PMMA properties and parameters

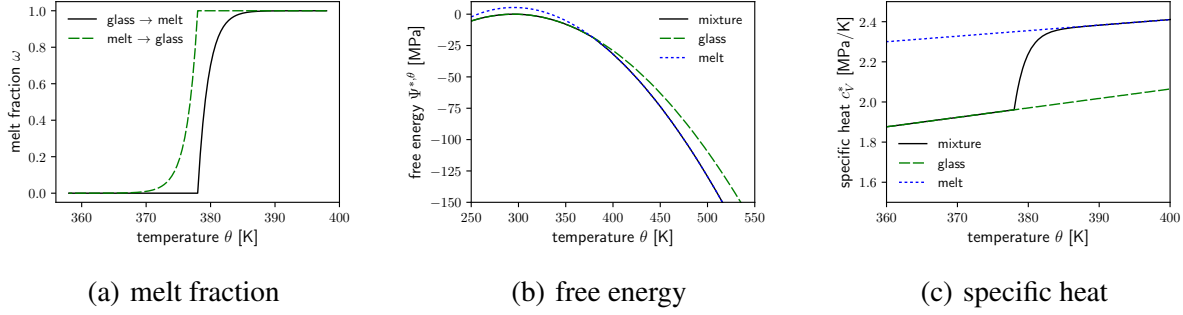


Figure A.1. Metastable melt and freezing processes at null pressure or strain: (a) melt fraction for melting and freezing (b) free energies and (c) specific heats of phases and mixture undergoing melting. Glass transition is $\theta_G = 378$ K.

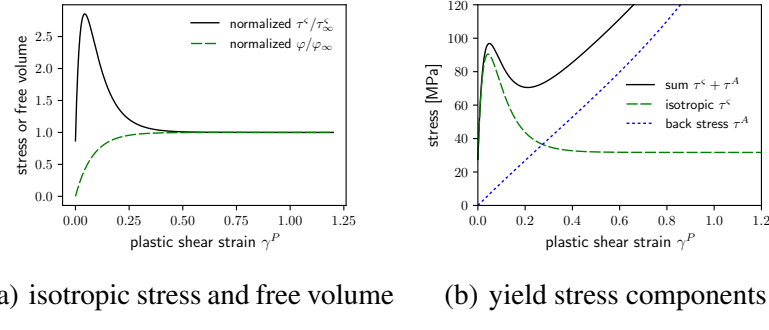


Figure A.2. Evolution of plastic free volume and shear strength versus monotonic plastic shear strain γ^P : (a) isotropic stress τ^ς and free volume φ normalized by $\tau_\infty^\varsigma = 31.7$ MPa and $\varphi_\infty = 3 \times 10^{-4}$ (b) isotropic stress τ^ς , anisotropic hardening stress τ^A , and their sum (no pressure hardening or thermal softening)

Table A.1. Physical properties and model parameters for Hugoniot analysis of PMMA, $\theta_0 = 295$ K

Property [units]	Definition	Value	Reference or source
ρ_0 [g/cm ³]	mass density at $\theta = \theta_0$	1.185	[7, 29]
θ_G [K]	static, atmospheric glass transition temperature	378	[20]
c_{V0}^G [MPa/K]	glass specific heat per unit volume at $\theta = \theta_0$	1.570	[2]
c_{V0}^M [MPa/K]	melt specific heat per unit volume at $\theta = \theta_0$	2.121	[2]
c_{V0}^D [MPa/K]	product specific heat per unit volume at $\theta = \theta_0$	1.570	assumed
c_{θ}^G/c_{V0}^G [1/K]	temperature derivative of glass specific heat	3.0×10^{-3}	[2]
c_{θ}^M/c_{V0}^M [1/K]	temperature derivative of melt specific heat	1.3×10^{-3}	[2]
c_{θ}^D/c_{V0}^D [1/K]	temperature derivative of product specific heat	1.3×10^{-3}	assumed
$\psi_0^{M,\theta}$ [MPa]	datum free energy of melt phase	5.35	calculated
β_{ω} [MPa]	kinetic factor for melt transition width	0.195	calculated
P_D^H [GPa]	Shock pressure threshold for decomposition onset	25.7	[85, 87]
J_D^H [-]	Hugoniot volume ratio at decomposition onset	0.58	calculated
θ_D [K]	Hugoniot temperature at onset of decomposition	1289	calculated
δ_{Ξ} [-]	relative volume change under shock decomposition	-0.034	[85, 86]
$\psi_0^{D,\theta}$ [GPa]	datum free energy of decomposed product phase	-0.103	calculated
λ_{θ}^{Ξ} [GPa]	kinetic latent heat of decomposed products	6.69	calculated
β_{Ξ} [GPa]	kinetic factor for decomposition transition width	1.5	calculated
$B_0^{G,E}$ [GPa]	isothermal bulk modulus of glass	5.71	from $C_L = 2.75$ km/s [20]
$B_1^{G,E}$ [-]	linear volume stiffening of bulk modulus of glass	1.3	calibrated
$B_2^{G,E}$ [-]	quadratic volume stiffening of bulk modulus of glass	15.0	calibrated
$B_3^{G,E}$ [-]	cubic volume stiffening of bulk modulus of glass	200	calibrated
$B_0^{D,E}$ [GPa]	isothermal bulk modulus of products	8.0	calibrated
$B_1^{D,E}$ [-]	linear volume stiffening of bulk modulus of products	1.5	calibrated
$B_2^{D,E}$ [-]	quadratic volume stiffening of bulk modulus of products	15.0	calibrated
$B_3^{D,E}$ [-]	cubic volume stiffening of bulk modulus of products	120	calibrated
$G_0^{G,E}$ [GPa]	elastic shear modulus of glass	2.29	[60]
$G_{\theta}^{G,E}$ [MPa/K]	linear thermal softening of shear modulus	-5.2	[60]
$G_p^{G,E}$ [-]	linear pressure stiffening of shear modulus	2.0	calibrated
$G_2^{G,E}$ [-]	quadratic pressure stiffening of shear modulus	0	not used
$\Gamma_0^{G,E}$ [-]	ambient pressure Grüneisen parameter of glass	0.657	[145]
$\Gamma_1^{G,E}$ [-]	linear volume dependence of Grüneisen parameter	0.657	[20]
$\Gamma_2^{G,E}$ [-]	quadratic volume dependence of Grüneisen parameter	16.0	[20]
$\Gamma_0^{D,E}$ [-]	ambient pressure Grüneisen parameter of products	0.667	ideal gas limit [91]
$\Gamma_1^{D,E} = \Gamma_2^{D,E}$ [-]	volume dependence of Grüneisen parameter of products	0	not used

Table A.2. Plasticity, fracture, and melt parameters for shock and spall analysis of PMMA

Property [units]	Definition	Value	Reference or source
P_p^H [GPa]	Hugoniot elastic limit (HEL)	0.740	[7, 29, 51, 115]
J_p^H [-]	volume ratio at HEL	0.937	calculated
θ_p [-]	temperature at HEL	306	calculated
N_0^P [-]	number of links per polymer chain	2.2525	[2]
N_θ^P [1/K]	thermal scaling of number of links	2.5×10^{-3}	[2]
μ_{A0} [MPa]	modulus for anisotropic hardening	10.2	[19]
$\mu_{A\theta}$ [MPa/K]	thermal scaling of plastic modulus	0.0942	[2]
τ_0^S [MPa]	initial isotropic plastic strength	27.5	[19]
τ_∞^S [MPa]	terminal isotropic plastic strength	31.7	[19]
ϕ_∞ [-]	terminal plastic free volume change	3×10^{-4}	[19]
a_φ [-]	kinetic parameter for free volume change	0.08	calibrated
b_φ [-]	kinetic parameter for isotropic strength	0.025	calibrated
μ_ξ^G [MPa]	modulus for isotropic hardening	151.2	calibrated
α_θ^F [-]	thermal softening of plastic flow	0.331	calculated
α_p^F [-]	pressure hardening of plastic flow	0.538	from HEL strength
$\dot{\gamma}_0$ [1/s]	reference plastic shearing rate	1.16×10^{16}	[2]
H_β/k_B [K]	activation energy of secondary relaxation	1.082×10^4	[2]
c_1^G [-]	shear yielding kinetic parameter	32.58	[2]
c_2^G [K]	shear yielding kinetic parameter	83.5	[2]
m [-]	rate sensitivity exponent for shear flow	0.157	[2]
V_F/k_B [K/MPa]	activation energy of secondary relaxation	7.062	[2]
f_1, f_2, f_3 [-]	fitting parameters for Hugoniot strength	-14.5, 262.3, -1979	calibrated
f_4, f_5, f_6 [-]	fitting parameters for Hugoniot strength	7369, -13732, 10119	calibrated
e_V^c [-]	inelastic strain above which f_R^P vanishes	0.41	calibrated
c_1^ϕ [MPa]	craze initiation parameter	45.6	[19]
c_2^ϕ [MPa ²]	craze initiation parameter	1130	[19]
$\dot{\varepsilon}_0$ [1/s]	reference craze strain rate	2×10^3	calibrated for spall
n [-]	rate sensitivity exponent for craze strain	3.33	calibrated for spall
λ_ϕ^P [-]	chain scission initiation stretch	1.39	[13]
Γ_ξ [J/m ²]	low temperature dynamic fracture energy	150	[179]
l_ξ [μm]	phase-field length constant	300	[14]
$c_\xi^P l_\xi / \Gamma_\xi$ [-]	ductile fracture driving force	25	[19]
$c_\xi^\phi l_\xi / \Gamma_\xi$ [-]	craze fracture driving force	10^9	calibrated for spall
$R_{\xi_0}^G l_\xi / \Gamma_\xi$ [-]	glass fracture resistance	115	calibrated for spall
$R_{\xi_0}^M l_\xi / \Gamma_\xi$ [-]	melt fracture resistance	6.96	calibrated for spall
α_ξ^M [-]	temperature dependence of melt fracture	9	calibrated for spall
β_ε [μs]	phase-field fracture kinetic time	5	calibrated for spall
$B_0^{M,E}$ [GPa]	isothermal bulk modulus of melt	3.31	from shock speed [79]
$G_0^{M,E}$ [GPa]	dynamic shear modulus of melt	1.50	from shear wave speed [79]
$G_\theta^{M,E}$ [MPa/K]	linear thermal softening of shear modulus	-3×10^{-3}	[3]

Table A.3. Refined elastic and viscoelastic parameters for steady wave analysis of PMMA, $\theta_0 = 295$ K

Property [units]	Definition	Value	Reference or source
$B_0^{G,E}$ [GPa]	relaxed isothermal bulk modulus	5.622	from $C_L = 2.73$ km/s [31, 51, 167]
$B_0^{G,I}$ [GPa]	instantaneous isothermal bulk modulus	5.817	from $C_L = 2.76$ km/s [21, 31, 51]
$B_1^{G,E} = B_1^{G,I}$ [-]	linear volume stiffening of bulk modulus	15.0	calibrated
$B_2^{G,E} = B_2^{G,I}$ [-]	quadratic volume stiffening of bulk modulus	-400	calibrated
$B_3^{G,E} = B_3^{G,I}$ [-]	cubic volume stiffening of bulk modulus	0	not used
$G_0^{G,E}$ [GPa]	relaxed elastic shear modulus	2.257	calibrated
$G_0^{G,I}$ [GPa]	instantaneous elastic shear modulus	2.302	[60, 180]
$G_p^{G,E}$ [-]	linear pressure stiffening of relaxed modulus	1.50	calibrated
$G_p^{G,I}$ [-]	linear pressure stiffening of instant modulus	1.65	calibrated
$\Gamma_0^{G,I}$ [-]	ambient pressure instant Grüneisen parameter	0.55	[145]
$\Gamma_1^{G,I}$ [-]	linear volume dependence of $\Gamma^{G,I}$	0.55	[20]
$\Gamma_2^{G,I}$ [-]	quadratic volume dependence of $\Gamma^{G,I}$	16.0	[20]
$\tau_V^V = \tau_V^S$ [μ s]	bulk viscoelastic relaxation time	1.200	calibrated
$\tau_S^S = \tau_V^S$ [μ s]	shear viscoelastic relaxation time	0.065	calibrated

References

- [1] S. Saeki, M. Tsubokawa, J. Yamanaka, and T. Yamaguchi. Correlation between the equation of state and the pressure dependence of glass transition and melting temperatures in polymers and rare-gas solids. *Polymer*, 33:577–584, 1992.
- [2] J. Richeton, S. Ahzi, K.S. Vecchio, F.C. Jiang, and A. Makradi. Modeling and validation of the large deformation inelastic response of amorphous polymers over a wide range of temperatures and strain rates. *International Journal of Solids and Structures*, 44:7938–7954, 2007.
- [3] V. Srivastava, S.A. Chester, N.M. Ames, and L. Anand. A thermo-mechanically-coupled large-deformation theory for amorphous polymers in a temperature range which spans their glass transition. *International Journal of Plasticity*, 26:1138–1182, 2010.
- [4] B.E. Clements. A continuum glassy polymer model applicable to dynamic loading. *Journal of Applied Physics*, 112:083511, 2012.
- [5] C.L. Beyler and M.M. Hirschler. Thermal decomposition of polymers. In *SFPE Handbook of Fire Protection Engineering*, volume 2, chapter 7, pages 111–131. National Fire Protection Association, Quincy (MA), 2002.
- [6] M. Grujicic, W.C. Bell, and B. Pandurangan. Design and material selection guidelines and strategies for transparent armor systems. *Materials and Design*, 34:808–819, 2012.
- [7] L.M. Barker and R.E. Hollenbach. Shock-wave studies of PMMA, fused silica, and sapphire. *Journal of Applied Physics*, 41:4208–4226, 1970.
- [8] A.S. Argon. Role of heterogeneities in the crazing of glassy polymers. *Pure and Applied Chemistry*, 43:247–272, 1975.
- [9] E.M. Arruda, M.C. Boyce, and R. Jayachandran. Effects of strain rate, temperature and thermomechanical coupling on the finite strain deformation of glassy polymers. *Mechanics of Materials*, 19:193–212, 1995.

- [10] N.A. Fleck, W.J. Stronge, and J.H. Liu. High strain-rate shear response of polycarbonate and polymethyl methacrylate. *Proceedings of the Royal Society of London A*, 429(1877): 459–479, 1990.
- [11] A.D. Mulliken and M.C. Boyce. Mechanics of the rate-dependent elastic–plastic deformation of glassy polymers from low to high strain rates. *International Journal of Solids and Structures*, 43:1331–1356, 2006.
- [12] J. Richeton, S. Ahzi, K.S. Vecchio, F.C. Jiang, and R.R. Adharapurapu. Influence of temperature and strain rate on the mechanical behavior of three amorphous polymers: characterization and modeling of the compressive yield stress. *International Journal of Solids and Structures*, 43:2318–2335, 2006.
- [13] B.P. Gearing and L. Anand. On modeling the deformation and fracture response of glassy polymers due to shear-yielding and crazing. *International Journal of Solids and Structures*, 41:3125–3150, 2004.
- [14] S. Narayan and L. Anand. Fracture of amorphous polymers: a gradient-damage theory. *Journal of the Mechanics and Physics of Solids*, 146:104164, 2021.
- [15] M.L. Williams, R.F. Landel, and J.D. Ferry. The temperature dependence of relaxation mechanisms in amorphous polymers and other glass-forming liquids. *Journal of the American Chemical Society*, 7:3701–3707, 1955.
- [16] L. Anand and M.E. Gurtin. A theory of amorphous solids undergoing large deformations, with application to polymeric glasses. *International Journal of Solids and Structures*, 40: 1465–1487, 2003.
- [17] V.S. Jatin and S. Basu. Investigations into the origins of plastic flow and strain hardening in amorphous glassy polymers. *International Journal of Plasticity*, 56:139–155, 2014.
- [18] R.P. White and J.E.G. Lipson. Polymer free volume and its connection to the glass transition. *Macromolecules*, 49:3987–4007, 2016.
- [19] H. Dal, O. Gultekin, S. Basdemir, and A. Acan. Ductile–brittle failure of amorphous glassy polymers: a phase-field approach. *Computer Methods in Applied Mechanics and Engineering*, 401:115639, 2022.
- [20] R. Menikoff. Constitutive model for polymethyl methacrylate at high pressure. *Journal of Applied Physics*, 96:7696–7704, 2004.
- [21] J.R. Asay, D.L. Lamberson, and A.H. Guenther. Pressure and temperature dependence of the acoustic velocities in polymethylmethacrylate. *Journal of Applied Physics*, 40:1768–1783, 1969.
- [22] R. Kono. The dynamic bulk viscosity of polystyrene and polymethyl methacrylate. *Journal of the Physical Society of Japan*, 15:718–725, 1960.
- [23] S.B. Sane and W.G. Knauss. The time-dependent bulk response of poly (methyl methacrylate). *Mechanics of Time-Dependent Materials*, 5:293–324, 2001.
- [24] B.E. Clements. Nonequilibrium volumetric response of shocked polymers. *AIP Conference Proceedings*, 1195:1223–1228, 2009.
- [25] L. Anand, N.M. Ames, V. Srivastava, and S.A. Chester. A thermo-mechanically coupled theory for large deformations of amorphous polymers. Part I: formulation. *International Journal of Plasticity*, 25:1474–1494, 2009.

[26] J.-L. Bouvard, D.K. Ward, D. Hossain, E.B. Marin, D.J. Bammann, and M.F. Horstemeyer. A general inelastic internal state variable model for amorphous glassy polymers. *Acta Mechanica*, 213:71–96, 2010.

[27] J.-L. Bouvard, D.K. Francis, M.A. Tschopp, E.B. Marin, D.J. Bammann, and M.F. Horstemeyer. An internal state variable material model for predicting the time, thermomechanical, and stress state dependence of amorphous glassy polymers under large deformation. *International Journal of Plasticity*, 42:168–193, 2013.

[28] B.D. Coleman and W. Noll. Foundations of linear viscoelasticity. *Reviews of Modern Physics*, 33:239–249, 1961.

[29] K.W. Schuler. Propagation of steady shock waves in polymethyl methacrylate. *Journal of the Mechanics and Physics of Solids*, 18:277–293, 1970.

[30] K.W. Schuler, J.W. Nunziato, and E.K. Walsh. Recent results in nonlinear viscoelastic wave propagation. *International Journal of Solids and Structures*, 9:1237–1281, 1973.

[31] J.W. Nunziato and E.K. Walsh. Propagation of steady shock waves in non-linear thermoviscoelastic solids. *Journal of the Mechanics and Physics of Solids*, 21:317–335, 1973.

[32] U.K. Jinaga, K. Zulueta, A. Burgoa, L. Cobian, U. Freitas, M. Lackner, Z. Major, and L. Noels. A consistent finite-strain thermomechanical quasi-nonlinear-viscoelastic viscoplastic constitutive model for thermoplastic polymers. *International Journal of Solids and Structures*, page 113517, 2025.

[33] G.A. Holzapfel and J.C. Simo. A new viscoelastic constitutive model for continuous media at finite thermomechanical changes. *International Journal of Solids and Structures*, 33: 3019–3034, 1996.

[34] G.A. Holzapfel. On large strain viscoelasticity: continuum formulation and finite element applications to elastomeric structures. *International Journal for Numerical Methods in Engineering*, 39:3903–3926, 1996.

[35] S. Sadik and A. Yavari. Nonlinear anisotropic viscoelasticity. *Journal of the Mechanics and Physics of Solids*, 182:105461, 2024.

[36] F. Sidoroff. Nonlinear viscoelastic model with intermediate configuration. *Journal de Mecanique*, 13:679–713, 1974.

[37] S. Reese and S. Govindjee. A theory of finite viscoelasticity and numerical aspects. *International Journal of Solids and Structures*, 35:3455–3482, 1998.

[38] J.D. Clayton. *Nonlinear Mechanics of Crystals*. Springer, Dordrecht, 2011.

[39] D.K. Francis, J.-L. Bouvard, Y. Hammi, and M.F. Horstemeyer. Formulation of a damage internal state variable model for amorphous glassy polymers. *International Journal of Solids and Structures*, 51:2765–2776, 2014.

[40] M.C. Boyce, D.M. Parks, and A.S. Argon. Large inelastic deformation of glassy polymers. Part I: rate dependent constitutive model. *Mechanics of Materials*, 7:15–33, 1988.

[41] A.S. Argon. A theory for the low-temperature plastic deformation of glassy polymers. *Philosophical Magazine*, 28:839–865, 1973.

[42] E.M. Arruda, M.C. Boyce, and H. Quintus-Bosz. Effects of initial anisotropy on the finite strain deformation behavior of glassy polymers. *International Journal of Plasticity*, 9:783–811, 1993.

- [43] R.B. Dupaix and M.C. Boyce. Constitutive modeling of the finite strain behavior of amorphous polymers in and above the glass transition. *Mechanics of Materials*, 39:39–52, 2007.
- [44] N.M. Ames, V. Srivastava, S.A. Chester, and L. Anand. A thermo-mechanically coupled theory for large deformations of amorphous polymers. Part II: applications. *International Journal of Plasticity*, 25:1495–1539, 2009.
- [45] J. Richeton, S. Ahzi, L. Daridon, and Y. Remond. A formulation of the cooperative model for the yield stress of amorphous polymers for a wide range of strain rates and temperatures. *Polymer*, 46:6035–6043, 2005.
- [46] J. Richeton, S. Ahzi, A. Makradi, and K.S. Vecchio. Constitutive modeling of polymer materials at impact loading rates. *Journal de Physique IV*, 134:103–107, 2006.
- [47] P.D. Wu and E. Van Der Giessen. On improved network models for rubber elasticity and their applications to orientation hardening in glassy polymers. *Journal of the Mechanics and Physics of Solids*, 41:427–456, 1993.
- [48] E.M. Arruda and M.C. Boyce. A three-dimensional constitutive model for the large stretch behavior of rubber elastic materials. *Journal of the Mechanics and Physics of Solids*, 41:389–412, 1993.
- [49] P. Khandagale, T. Breitzman, C. Majidi, and K. Dayal. Statistical field theory for nonlinear elasticity of polymer networks with excluded volume interactions. *Physical Review E*, 107:064501, 2023.
- [50] G. Palm, R.B. Dupaix, and J. Castro. Large strain mechanical behavior of poly (methyl methacrylate)(PMMA) near the glass transition temperature. *Journal of Engineering Materials and Technology*, 128:559–563, 2006.
- [51] K.W. Schuler and J.W. Nunziato. The dynamic mechanical behavior of polymethyl methacrylate. *Rheologica Acta*, 13:265–273, 1974.
- [52] L.A. Merzhievskii and M.S. Voronin. Modeling of shock-wave deformation of polymethyl methacrylate. *Combustion, Explosion, and Shock Waves*, 48:226–235, 2012.
- [53] T.V. Popova, A.E. Mayer, and K.V. Khishchenko. Numerical investigations of shock wave propagation in polymethylmethacrylate. *Journal of Physics: Conference Series*, 653:012045, 2015.
- [54] T.V. Popova, A.E. Mayer, and K.V. Khishchenko. Evolution of shock compression pulses in polymethylmethacrylate and aluminum. *Journal of Applied Physics*, 123:235902, 2018.
- [55] A. Dorogoy, D. Rittel, and A. Brill. A study of inclined impact in polymethylmethacrylate plates. *International Journal of Impact Engineering*, 37:285–294, 2010.
- [56] T.J. Holmquist, J. Bradley, A. Dwivedi, and D. Casem. The response of polymethyl methacrylate (PMMA) subjected to large strains, high strain rates, high pressures, a range in temperatures, and variations in the intermediate principal stress. *European Physical Journal Special Topics*, 225:343–354, 2016.
- [57] B.P. Lawlor, V. Gandhi, and G. Ravichandran. Full-field quantitative visualization of shock-driven pore collapse and failure modes in PMMA. *Journal of Applied Physics*, 136:225901, 2024.
- [58] B.D. Coleman and W. Noll. The thermodynamics of elastic materials with heat conduction and viscosity. *Archive for Rational Mechanics and Analysis*, 13:167–178, 1963.

- [59] B.D. Coleman and M.E. Gurtin. Thermodynamics with internal state variables. *Journal of Chemical Physics*, 47:597–613, 1967.
- [60] D.R. Christman. Dynamic properties of polymethylmethacrylate (PMMA) (Plexiglas). Technical Report DNA-2810F, Defense Nuclear Agency, Washington, D.C., 1972.
- [61] P.D. Washabaugh and W.G. Knauss. Non-steady, periodic behavior in the dynamic fracture of PMMA. *International Journal of Fracture*, 59:189–197, 1993.
- [62] A.S. Argon and M.M. Salama. Growth of crazes in glassy polymers. *Philosophical Magazine*, 36:1217–1234, 1977.
- [63] C. G’Sell, J.M. Hiver, and A. Dahoun. Experimental characterization of deformation damage in solid polymers under tension, and its interrelation with necking. *International Journal of Solids and Structures*, 39:3857–3872, 2002.
- [64] S. Satapathy and S. Bless. Deep punching PMMA. *Experimental Mechanics*, 40:31–37, 2000.
- [65] D. Rittel and A. Brill. Dynamic flow and failure of confined polymethylmethacrylate. *Journal of the Mechanics and Physics of Solids*, 56:1401–1416, 2008.
- [66] L. Zhang, D. Townsend, N. Petrinic, and A. Pellegrino. Pressure and temperature dependent dynamic flow and failure behavior of PMMA at intermediate strain rates. *International Journal of Impact Engineering*, 158:104026, 2021.
- [67] J.S. Archer and A.J. Lesser. Shear band formation and mode II fracture of polymeric glasses. *Journal of Polymer Science B: Polymer Physics*, 49:103–114, 2010.
- [68] T. Bjerke and J. Lambros. Heating during shearing and opening dominated dynamic fracture of polymers. *Experimental Mechanics*, 42:107–114, 2002.
- [69] R. Estevez, M.G.A. Tijssens, and E. Van der Giessen. Modeling of the competition between shear yielding and crazing in glassy polymers. *Journal of the Mechanics and Physics of Solids*, 48:2585–2617, 2000.
- [70] I. Arias, J. Knap, V.B. Chalivendra, S. Hong, M. Ortiz, and A.J. Rosakis. Numerical modelling and experimental validation of dynamic fracture events along weak planes. *Computer Methods in Applied Mechanics and Engineering*, 196:3833–3840, 2007.
- [71] A. Schluter, C. Kuhn, R. Muller, and D. Gross. An investigation of intersonic fracture using a phase field model. *Archive of Applied Mechanics*, 86:321–333, 2016.
- [72] J.D. Clayton. Dynamic plasticity and fracture in high density polycrystals: constitutive modeling and numerical simulation. *Journal of the Mechanics and Physics of Solids*, 53: 261–301, 2005.
- [73] J.D. Clayton. Modeling dynamic plasticity and spall fracture in high density polycrystalline alloys. *International Journal of Solids and Structures*, 42:4613–4640, 2005.
- [74] J.W. Foulk and T.J. Vogler. A grain-scale study of spall in brittle materials. *International Journal of Fracture*, 163:225–242, 2010.
- [75] C. Miehe, M. Hofacker, L.M. Schanzel, and F. Aldakheel. Phase field modeling of fracture in multi-physics problems. Part II. Coupled brittle-to-ductile failure criteria and crack propagation in thermo-elastic-plastic solids. *Computer Methods in Applied Mechanics and Engineering*, 294:486–522, 2015.
- [76] K. Li, H. Deng, W. Xu, and Y. Liu. Modelling of fracture-involved large strain behaviors of

amorphous glassy polymers via a unified physically-based constitutive model coupled with phase field method. *Engineering Fracture Mechanics*, 311:110546, 2024.

- [77] A.A. Geraskin, K.V. Khishchenko, I.K. Krasyuk, P.P. Pashinin, A.Y. Semenov, and V.I. Vovchenko. Specific features of spallation processes in polymethyl methacrylate under high strain rate. *Contributions in Plasma Physics*, 49:451–454, 2009.
- [78] J.M. Diamond and K.T. Ramesh. Spallation of polycarbonate on nanosecond timescales. *Physical Review E*, 111:025503, 2025.
- [79] E.B. Zaretsky and G.I. Kanel. Response of poly (methyl methacrylate) to shock-wave loading at elevated temperatures. *Journal of Applied Physics*, 126:085902, 2019.
- [80] I.A. Cherepanov, A.S. Savinykh, G.V. Garkushin, and S.V. Razorenov. Spall strength of polycarbonate at a temperature of 20–185 C. *Technical Physics*, 69:1938–1944, 2024.
- [81] D.R. Curran, D.A. Shockley, and L. Seaman. Dynamic fracture criteria for a polycarbonate. *Journal of Applied Physics*, 44:4025–4038, 2012.
- [82] D.M. Dattlebaum, B.F. Schilling, B.E. Clements, J.L. Jordan, C.F. Welch, and J.A. Stull. Shock response and dynamic failure of high-density (HDPE) and ultra-high molecular weight polyethylene (UHMWPE). *Journal of Dynamic Behavior of Materials*, 12:37–48, 2026.
- [83] M.A.N. Dewapriya and R.E. Miller. Molecular dynamics study on the shock induced spallation of polyethylene. *Journal of Applied Physics*, 131:025102, 2022.
- [84] J.D. Clayton. Phase-field theory of adiabatic shear. *Acta Mechanica*, 237:239–273, 2026.
- [85] W.J. Carter and S.P. Marsh. Hugoniot equation of state of polymers. Technical Report LA-13006-MS, Los Alamos National Laboratory, Los Alamos (NM), 1995.
- [86] D.M. Dattelbaum and J.D. Coe. Shock-driven decomposition of polymers and polymeric foams. *Polymers*, 11:493, 2019.
- [87] G.E. Hauver and A. Melani. Shock compression of plexiglas and polystyrene. Technical Report BRL-R-1259, Ballistic Research Laboratory, Aberdeen Proving Ground (MD), 1964.
- [88] G.E. Hauver. Shock-induced polarization in plastics. II. Experimental study of plexiglas and polystyrene. *Journal of Applied Physics*, 36:2113–2118, 1965.
- [89] M.K. Lentz, J.D. Coe, and K.A. Velizhanin. Reshock analysis for PMMA driven above the threshold for chemical decomposition. *AIP Conference Proceedings*, 2272:070027, 2020.
- [90] S.A. Bordzilovskii, M.S. Voronin, and S.M. Karakhanov. Temperature of polymethyl methacrylate in a secondary shock wave. *Combustion, Explosion, and Shock Waves*, 57: 736–745, 2021.
- [91] J.D. Coe, M. Lentz, K.A. Velizhanin, J.T. Gammel, J. Kaushagen, K. Jones, and K.R. Cochrane. The equation of state and shock-driven decomposition of polymethylmethacrylate (PMMA). *Journal of Applied Physics*, 131, 2022.
- [92] R.C. Huber, D.M. Dattelbaum, J.M. Lang, J.D. Coe, J.H. Peterson, B. Bartram, and L.L. Gibson. Polyimide dynamically compressed to decomposition pressures: two-wave structures captured by velocimetry and modeling. *Journal of Applied Physics*, 133:035106, 2023.
- [93] R.A. Graham. Shock-induced electrical activity in polymeric solids. A mechanically induced bond scission model. *Journal of Physical Chemistry*, 83:3048–3056, 1979.
- [94] K.-S. Chan and A.L. Ruoff. Static compression of polymethyl methacrylate to 100 GPa.

Journal of Applied Physics, 52:5395–5396, 1981.

- [95] K.A. Maerzke, J.D. Coe, C. Ticknor, J.A. Leiding, J. Tinka Gammel, and C.F. Welch. Equations of state for polyethylene and its shock-driven decomposition products. *Journal of Applied Physics*, 126:045902, 2019.
- [96] T. Kashiwagi, T. Hirata, and J.E. Brown. Thermal and oxidative degradation of poly (methyl methacrylate) molecular weight. *Macromolecules*, 18:131–138, 1985.
- [97] S.I. Stoliarov, P.R. Westmoreland, M.R. Nyden, and G.P. Forney. A reactive molecular dynamics model of thermal decomposition in polymers: I. Poly (methyl methacrylate). *Polymer*, 44:883–894, 2003.
- [98] O.P. Korobeinichev, A.A. Paletsky, M.B. Gonchikzhev, R.K. Glaznev, I.E. Gerasimov, Y.K. Naganovsky, I.K. Shundrina, A.Y. Snegirev, and R. Vinu. Kinetics of thermal decomposition of PMMA at different heating rates and in a wide temperature range. *Thermochimica Acta*, 671:17–25, 2019.
- [99] M. Van Thiel, J. Shaner, and E. Salinas (editors). Compendium of shock wave data. Volume 3. Technical Report UCRL-50108-3, Lawrence Livermore Laboratory, Livermore (CA)), 1977.
- [100] M. Scheidler. Viscoelastic models for nearly incompressible materials. Technical Report ARL-TR-4992, Army Research Laboratory, Aberdeen Proving Ground (MD), 2009.
- [101] J.D. Clayton. Analysis of shock compression of strong single crystals with logarithmic thermoelastic-plastic theory. *International Journal of Engineering Science*, 79:1–20, 2014.
- [102] J.D. Clayton. *Nonlinear Elastic and Inelastic Models for Shock Compression of Crystalline Solids*. Springer, Cham, 2019.
- [103] V.I. Levitas and K. Samani. Coherent solid/liquid interface with stress relaxation in a phase-field approach to the melting/solidification transition. *Physical Review B*, 84:140103, 2011.
- [104] A. Bahloul, I. Doghri, and L. Adam. An enhanced phase field model for the numerical simulation of polymer crystallization. *Polymer Crystallization*, 3:e10144, 2020.
- [105] V.I. Levitas, A.V. Idesman, and A.K. Palakala. Phase-field modeling of fracture in liquid. *Journal of Applied Physics*, 110:033531, 2011.
- [106] J.D. Clayton. Universal phase-field mixture representation of thermodynamics and shock wave mechanics in porous soft biologic continua. *Physical Review E*, 110:035001, 2024.
- [107] J.D. Clayton. Analysis of adiabatic strain localization coupled to ductile fracture and melting, with application and verification for simple shear. *AppliedMath*, 5:169, 2025.
- [108] J.H. Gibbs and E.A. DiMarzio. Nature of the glass transition and the glassy state. *Journal of Chemical Physics*, 28:373–383, 1958.
- [109] J. Wu. The glassy state, ideal glass transition, and second-order phase transition. *Journal of Applied Polymer Science*, 71:143–150, 1999.
- [110] J.C.F. Millett and N.K. Bourne. The deviatoric response of polymethylmethacrylate to one-dimensional shock loading. *Journal of Applied Physics*, 88:7037–7040, 2000.
- [111] Y.M. Gupta, D.D. Keough, D. Henley, and D.F. Walter. Measurement of lateral compressive stresses under shock loading. *Applied Physics Letters*, 37:395–397, 1980.
- [112] Y.M. Gupta. Determination of the impact response of PMMA using combined compression and shear loading. *Journal of Applied Physics*, 51:5352–5361, 1980.

- [113] J.L. Jordan, D.T. Casem, B.T. Sturtevant, and G. Sutherland. Dynamic strength in polymethylmethacrylate. *AIP Conference Proceedings*, 2272:040006, 2002.
- [114] Y.V. Batkov, S.A. Novikov, and N.D. Fishman. Shear stresses in polymers under shock compression. *AIP Conference Proceedings*, 370:577–580, 1996.
- [115] Z. Rosenberg and Y. Partom. Accounting for the Hugoniot elastic limits of polymers by using pressure-dependent yield criterion. *Journal of Applied Physics*, 76:1935–1936, 1994.
- [116] J.W. Nunziato and K.W. Schuler. Evolution of steady shock waves in polymethyl methacrylate. *Journal of Applied Physics*, 44:4774–4775, 1973.
- [117] J.W. Nunziato and E.K. Walsh. Amplitude behavior of shock waves in a thermoviscoelastic solid. *International Journal of Solids and Structures*, 9:1373–1383, 1973.
- [118] P.J. Chen and M.E. Gurtin. On the growth of one-dimensional shock waves in materials with memory. *Archive for Rational Mechanics and Analysis*, 36:33–46, 1970.
- [119] P.J. Chen and M.E. Gurtin. Thermodynamic influences on the growth of one-dimensional shock waves in materials with memory. *Zeitschrift fur Angewandte Mathematik und Physik (ZAMP)*, 23:69–79, 1972.
- [120] P.J. Chen and M.E. Gurtin. Growth and decay of one-dimensional shock waves in fluids with internal state variables. *Physics of Fluids*, 14:1091–1094, 1971.
- [121] J.D. Clayton. Nonlinear thermodynamic phase field theory with application to fracture and dynamic inelastic phenomena in ceramic polycrystals. *Journal of the Mechanics and Physics of Solids*, 157:104633, 2021.
- [122] J.D. Clayton and C.L. Williams. Modelling the anomalous shock response of titanium diboride. *Proceedings of the Royal Society of London A*, 478:20220253, 2022.
- [123] L.E. Malvern. *Introduction to the Mechanics of a Continuous Medium*. Prentice-Hall, Englewood Cliffs NJ, 1969.
- [124] J.E. Marsden and T.J.R. Hughes. *Mathematical Foundations of Elasticity*. Prentice-Hall, Englewood Cliffs NJ, 1983.
- [125] M.E. Gurtin. Generalized Ginzburg-Landau and Cahn-Hilliard equations based on a micro-force balance. *Physica D*, 92:178–192, 1996.
- [126] M.J. Borden, T.J.R. Hughes, C.M. Landis, A. Anvari, and I.J. Lee. A phase-field formulation for fracture in ductile materials: finite deformation balance law derivation, plastic degradation, and stress triaxiality effects. *Computer Methods in Applied Mechanics and Engineering*, 312:130–166, 2016.
- [127] C. Miehe, L.-M. Schaenzel, and H. Ulmer. Phase field modeling of fracture in multi-physics problems. Part I. Balance of crack surface and failure criteria for brittle crack propagation in thermo-elastic solids. *Computer Methods in Applied Mechanics and Engineering*, 294: 449–485, 2015.
- [128] M.E. Gurtin and L. Anand. A theory of strain-gradient plasticity for isotropic, plastically irrotational materials. Part II: finite deformations. *International Journal of Plasticity*, 21: 2297–2318, 2005.
- [129] J.D. Clayton. *Differential Geometry and Kinematics of Continua*. World Scientific, Singapore, 2014.
- [130] L. Anand. On H. Hencky’s approximate strain-energy function for moderate deformations.

Journal of Applied Mechanics, 46:78–82, 1979.

- [131] J.E. Fitzgerald. A tensorial Hencky measure of strain and strain rate for finite deformations. *Journal of Applied Physics*, 51:5111–5115, 1980.
- [132] J.C. Criscione, J.D. Humphrey, A.S. Douglas, and W.C. Hunter. An invariant basis for natural strain which yields orthogonal stress response terms in isotropic hyperelasticity. *Journal of the Mechanics and Physics of Solids*, 48:2445–2465, 2000.
- [133] J.D. Clayton. Nonlinear thermomechanics for analysis of weak shock profile data in ductile polycrystals. *Journal of the Mechanics and Physics of Solids*, 124:714–757, 2019.
- [134] L. Schanzel, H. Dal, and C. Miehe. A new continuum approach to the coupling of shear yielding and crazing with fracture in glassy polymers. *Proceedings of Applied Mathematics and Mechanics (PAMM)*, 12:337–338, 2012.
- [135] S. Basdemir, O. Gultekin, and H. Dal. Coupled thermo-viscoplastic fracture model for ductile-brittle failure of amorphous glassy polymers with phase-field approach. *Proceedings of Applied Mathematics and Mechanics (PAMM)*, 22:e202200280, 2022.
- [136] C. Miehe, F. Welschinger, and M. Hofacker. Thermodynamically consistent phase-field models of fracture: Variational principles and multi-field FE implementations. *International Journal for Numerical Methods in Engineering*, 83:1273–1311, 2010.
- [137] J.D. Clayton, R.B. Leavy, and J. Knap. Phase field theory for pressure-dependent strength in brittle solids with dissipative kinetics. *Mechanics Research Communications*, 129:104097, 2023.
- [138] Y.-L. Loo, R. A. Register, A.J. Ryan, and G.T. Dee. Polymer crystallization confined in one, two, or three dimensions. *Macromolecules*, 34:8968–8977, 2001.
- [139] D. Rittel. On the conversion of plastic work to heat during high strain rate deformation of glassy polymers. *Mechanics of Materials*, 31:131–139, 1999.
- [140] G. Shao, S. Zhu, Y. Wang, and Q. Zhao. An internal state variable thermodynamic model for determining the Taylor-Quinney coefficient of glassy polymers. *International Journal of Mechanical Sciences*, 126:261–269, 2017.
- [141] J.D. Clayton and J. Knap. A geometrically nonlinear phase field theory of brittle fracture. *International Journal of Fracture*, 189:139–148, 2014.
- [142] L. Davison. *Fundamentals of Shock Wave Propagation in Solids*. Springer, Berlin, 2008.
- [143] M. Born. Thermodynamics of crystals and melting. *Journal of Chemical Physics*, 7:591–603, 1939.
- [144] J.D. Clayton and J.T. Lloyd. Finite strain continuum theory for phase transformations in ferromagnetic elastic-plastic solids. *Continuum Mechanics and Thermodynamics*, 34:1579–1620, 2022.
- [145] J.W. Nunziato and E.K. Walsh. Instantaneous and equilibrium Grüneisen parameters for a nonlinear viscoelastic polymer. *Journal of Applied Physics*, 44:1207–1211, 1973.
- [146] G.A. Holzapfel and T.C. Gasser. A viscoelastic model for fiber-reinforced composites at finite strains: continuum basis, computational aspects and applications. *Computer Methods in Applied Mechanics and Engineering*, 190:4379–4403, 2001.
- [147] G.A. Holzapfel, T.C. Gasser, and M. Stadler. A structural model for the viscoelastic behavior of arterial walls: continuum formulation and finite element analysis. *European Journal of*

Mechanics A Solids, 21:441–463, 2002.

- [148] W. Hu, H. Guo, Y. Chen, R. Xie, H. Jing, and H. Peng. Experimental investigation and modeling of the rate-dependent deformation behavior of PMMA at different temperatures. *European Polymer Journal*, 85:313–323, 2016.
- [149] C.E. Federico, J.L. Bouvard, C. Combeaud, and N. Billon. Large strain/time dependent mechanical behaviour of PMMAs of different chain architectures. Application of time-temperature superposition principle. *Polymer*, 139:177–187, 2018.
- [150] C. Miehe, S. Goktepe, and J.M. Diez. Finite viscoplasticity of amorphous glassy polymers in the logarithmic strain space. *International Journal of Solids and Structures*, 46:181–202, 2009.
- [151] A. Cohen. A Pade approximant to the inverse Langevin function. *Rheologica Acta*, 30: 270–273, 1991.
- [152] J.D. Clayton, H.A. Murdoch, J.T. Lloyd, D.J. Magagnosc, and D.M. Field. Modeling magnetic field and strain driven phase transitions and plasticity in ferrous metals. *Zeitschrift für Angewandte Mathematik und Mechanik (ZAMM)*, 104:e202200612, 2024.
- [153] C. Miehe and L.-M. Schanzel. Phase field modeling of fracture in rubbery polymers. Part I: finite elasticity coupled with brittle failure. *Journal of the Mechanics and Physics of Solids*, 65:93–113, 2014.
- [154] B.E. Clements. A continuum theory of dynamically loaded polymers. *arXiv preprint*, arXiv.1207.2723, 2012.
- [155] O. Olabisi and R. Simha. Pressure-volume-temperature studies of amorphous and crystallizable polymers. I. Experimental. *Macromolecules*, 8:206–210, 1975.
- [156] J.W. Forbes. Experimental investigation of the kinetics of the shock-induced alpha to epsilon phase transformation in Armco iron. Technical Report NSWC/WOL TR 77-137, Naval Surface Warfare Center, Silver Spring (MD), 1977.
- [157] J.C. Boettger and D.C. Wallace. Metastability and dynamics of the shock-induced phase transition in iron. *Physical Review B*, 55:2840–2849, 1997.
- [158] S.B. Kormer. Optical study of the characteristics of shock-compressed condensed dielectrics. *Soviet Physics Uspekhi*, 11:229–254, 1968.
- [159] M.-S. Jeong, J.-H. Ko, Y.H. Ko, and K.J. Kim. High-pressure elasticity of poly(methyl methacrylate) up to 31.5 gpa studied by Brillouin spectroscopy. *Current Applied Physics*, 15:943–946, 2015.
- [160] M.L. Wilkins. Use of artificial viscosity in multidimensional fluid dynamic calculations. *Journal of Computational Physics*, 36:281–303, 1980.
- [161] D.J. Benson. Explicit finite element methods for large deformation problems in solid mechanics. In E. Stein, R. de Borst, and T.J.R. Hughes, editors, *Encyclopedia of Computational Mechanics*, volume 2, chapter 25, pages 1–43. John Wiley and Sons, New York, 2007.
- [162] A. Morro. Shock waves in thermo-viscous fluids with hidden variables. *Archive of Mechanics*, 32:193–199, 1980.
- [163] J.L. Jordan, D. Casem, and M. Zellner. Shock response of polymethylmethacrylate. *Journal of Dynamic Behavior of Materials*, 2:372–378, 2016.
- [164] J.L. Jordan, D. Casem, P. Moy, and T. Walter. Properties and shock response of PMMA.

AIP Conference Proceedings, 1793:140007, 2017.

- [165] D. Lacina, C. Neel, and D. Dattelbaum. Shock response of polymethyl methacrylate (PMMA) measured with embedded electromagnetic gauges. *Journal of Applied Physics*, 123:185901, 2018.
- [166] J.W. Nunziato, K.W. Schuler, and E.K. Walsh. The bulk response of viscoelastic solids. *Transactions of the Society of Rheology*, 16:15–32, 1972.
- [167] J.W. Nunziato and H.J. Sutherland. Acoustical determination of stress relaxation functions for polymers. *Journal of Applied Physics*, 44:184–187, 1973.
- [168] Z. Rosenberg and Y. Partom. Direct measurement of temperature in shock-loaded polymethylmethacrylate with very thin copper thermistors. *Journal of Applied Physics*, 56: 1921–1926, 1984.
- [169] S.A. Bordzilovskii, S.M. Karakhanov, L.A. Merzhievskii, and M.S. Voronin. Temperature measurements for shocked polymethylmethacrylate, epoxy resin, and polytetrafluoroethylene and their equations of state. *Journal of Applied Physics*, 120:135903, 2016.
- [170] W.D. Reinhart and L.C. Chhabildas. Response to unloading and reloading of shock compressed polymethyl methacrylate. *AIP Conference Proceedings*, 845:131–134, 2006.
- [171] M.N. Pavlovskii. Measurements of the velocity of sound in shock-compressed quartzite, dolomite, anhydrite, sodium chloride, paraffin, plexiglas, polyethylene, and fluoroplast-4. *Journal of Applied Mechanics and Technical Physics*, 17:709–712, 1976.
- [172] C.L. Williams, J.T. Lloyd, D.T. Mallick, J.P. Ligda, and J.D. Clayton. Real-time observation of twinning, detwinning, and melting in shock-compressed magnesium alloy AZ31B-H24. *Physical Review Materials*, 9:043603, 2025.
- [173] D. Rittel. Experimental investigation of transient thermoplastic effects in dynamic fracture. *International Journal of Solids and Structures*, 37:2901–2913, 2000.
- [174] R.M. Bowen and P.J. Chen. Shock waves in ideal fluid mixtures with several temperatures. *Archive for Rational Mechanics and Analysis*, 53:277–294, 1974.
- [175] J.D. Clayton. Analysis of shock waves in a mixture theory of a thermoelastic solid and fluid with distinct temperatures. *International Journal of Engineering Science*, 175:103675, 2022.
- [176] P.T. Bartkowski and D.P. Dandekar. Recompression of PMMA following shock induced tension. *AIP Conference Proceedings*, 505:539–542, 2000.
- [177] C.B. Martinez and M.C. Williams. Viscosity and microstructure of polyethylene-poly (methyl methacrylate) melt blends: some simple interpretations. *Journal of Rheology*, 24: 421–450, 1980.
- [178] C.L. Williams, B.C. Hornbuckle, D.D. Mallick, T.C. Parker, J.D. Clayton, and J.W. Wilkerson. Strength-ductility synergy of a high chromium martensitic steel with a unique microstructure under dynamic extremes. *Acta Materialia*, 298:121368, 2025.
- [179] A.G. Atkins, C.S. Lee, and R.M. Caddell. Time-temperature dependent fracture toughness of PMMA: Part 1. *Journal of Materials Science*, 10:1381–1393, 1975.
- [180] D.R. Stephens, H.C. Heard, and R.N. Schock. High-pressure mechanical properties of polymethylmethacrylate. Technical Report R-4531, Lawrence Livermore National Laboratory, Livermore (CA), 1972.